MIT's Interferometer CST Testbed 647

647 is handwritten.

Tupper Hyde*, Ed Kim**, Eric Anderson**, Gary Blackwood**, and Leonard Lublin**

Space Engineering Research Center
Massachusetts Institute of Technology
Cambridge, MA 02139

Introduction

The MIT Space Engineering Research Center (SERC) has developed a controlled structures technology (CST) testbed based on one design for a space-based optical interferometer. The role of the testbed is to provide a versatile platform for experimental investigation and discovery of CST approaches. In particular, it will serve as the focus for experimental verification of CSI methodologies and control strategies at SERC. The testbed program has an emphasis on experimental CST--incorporating a broad suite of actuators and sensors, active struts, system identification, passive damping, active mirror mounts, and precision component characterization.

The SERC testbed represents a one-tenth scaled version of an optical interferometer concept based on an inherently rigid tetrahedral configuration with collecting apertures on one face. The testbed consists of six 3.5 meter long truss legs joined at four vertices and is suspended with attachment points at three vertices (Figure 1). Each aluminum leg has a 0.2m by 0.2m by 0.25m triangular cross-section. The structure has a first flexible mode at 31 Hz and has over 50 global modes below 200 Hz. The stiff tetrahedral design differs from similar testbeds (such as the JPL Phase B) in that the structural topology is closed. The tetrahedral design minimizes structural deflections at the vertices (site of optical components for maximum baseline) resulting in reduced stroke requirements for isolation and pointing of optics. Typical total light path length stability goals are on the order of $\lambda/20$, with a wavelength of light, λ, of roughly 500 nanometers [1]. It is expected that active structural control will be necessary to achieve this goal in the presence of disturbances.

A unique feature of the SERC testbed is the implementation of a multi-axis laser metrology, incorporating complex bends in multiple beam path lengths. At three mock siderostat locations are precision three-axis active mirror mounts. The fourth vertex holds a laser head and other optics. These optical components provide laser interferometric displacement measurements for baseline metrology (six axes define the position of the mock collecting apertures relative to the fourth reference point). We are concerned that the testbed represents a scaled model of an actual scientific observatory as closely as possible. At the same time, we seek to perform CST research which is generic and applicable in different areas.

The structure is instrumented with accelerometers, load cells, strain gages, experimental piezoceramic and piezopolymer sensors, and (initially) three piezoceramic active strut members. The stiffness of the active struts has been selected to approximately match the impedance of structure as seen by the actuator at the active strut mounting location, leading naturally to control designs based on passive shunting, wave impedance, or balanced bridge feedback.

A finite element model of the testbed was constructed and a conventional system identification using an external excitation source will be carried out. The results (frequencies, mode shapes) will be compared and the subsequent roles of each of these models in the control design determined. Because of inherent inaccuracies of the finite element model in representing lightly damped closely spaced modes, the experimentally determined modal model is preferred for control design. Methods for generating uncertainty information from the system identification for application in robust control methodologies, and studies of model reduction techniques are planned.

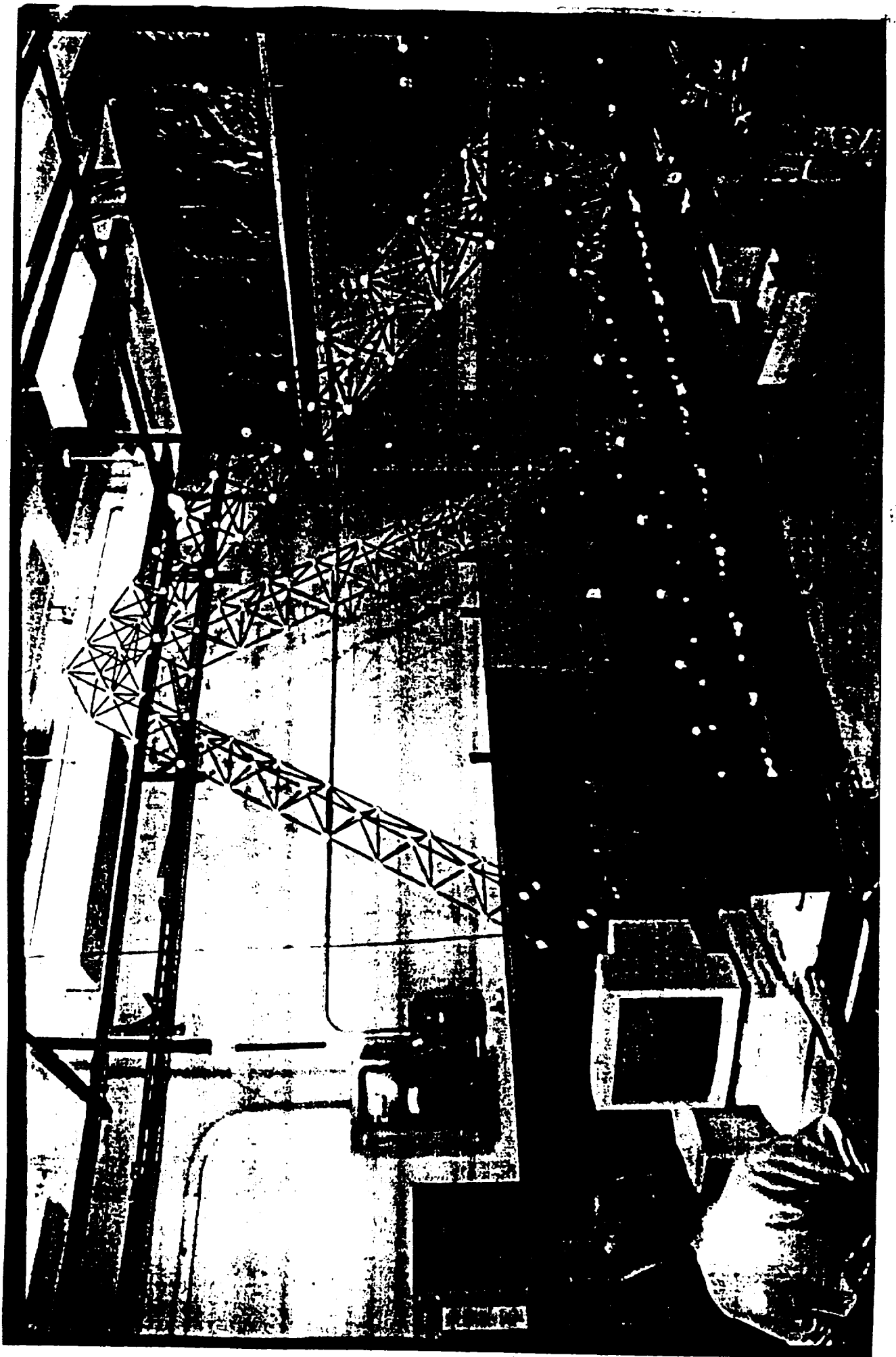* Research Associate   ** Graduate Research Assistant

Figure 1. MIT SERC Interferometer CSI Testbed

Three-axis active mirror mounts have been designed which provide ±3.5 microns of stroke over a frequency range of 500 Hz. Two mounts employ conventional piezoelectric actuators; the third mount utilizes electrostrictive actuators that exhibit superior bidirectional repeatability, a result of greater linearity and reduced hysteresis as compared to piezoelectrics. The moving mirror mass has been sized to reflect the approximate scaled masses of siderostats of the proposed space-based optical interferometer. The actual moving mass of the the mirrors will be varied to determine the level at which interaction with the structural flexibility becomes significant.

The remainder of the paper begins with a description of the optics portion of the testbed. Then the testbed CST program is reviewed with attention focussed in six areas: results from other research closely-related to the testbed, finite element modelling, system identification, passive damping, an axial component tester, and control experiments.

Optics

In this section, the optical components of the testbed are described. The focus here is on the implementation of the on-board metrology system. Functional explanations of space-based interferometry can be found elsewhere in this volume.

Beam-combining coherence requirements for an actual space-based interferometer will require on-board sensing and correction mechanisms capable of controlling path lengths to $\lambda/20$. Multi-aperture non-interferometric imaging instruments with similar baselines and operating wavelengths can have more demanding requirements. The sensing system for orienting the instrument relative to an external reference coordinate frame should have resolution and stability on par with the resolution and stability of the internal metrology system. Our immediate concern is the reduction in errors due to flexibility (Figure 2).

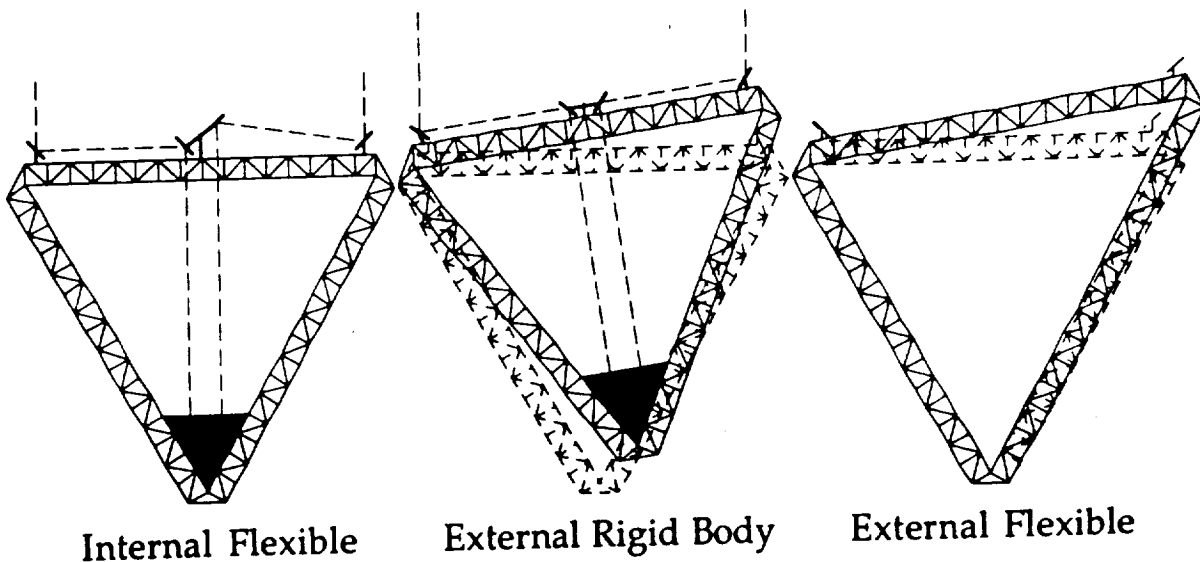Internal Flexible   External Rigid Body   External Flexible

Figure 2: Sources of Path Length Error

The Interferometer CST Testbed under construction at MIT addresses the problem of most direct relevance to CST: control of the instrument geometry in order to control projected baselines and internal path lengths. The testbed control goal is to maintain fixed distances between points on

the structure which represent collecting apertures (mock siderostats) and metrology nodes, since relative motion among these points changes both projected baselines and internal path lengths.

A sample interferometer mission to image a tenth magnitude object at visible wavelengths with one milliarcsecond resolution using one meter apertures leads to path length stability requirements of approximately 80 nm rms. The basic testbed configuration is intended to include enough detail to be representative without being overly complex and costly. Many of the features may be applicable to other spacecraft requiring precision control. Sensing of the external (rigid body) orientation of the testbed and the science optics are not currently addressed, although metrology systems for both of these could be tied directly into the on-board baseline metrology system with little difficulty. Additionally, each mock siderostat mount includes provisions for mounting a small flat mirror with its reflecting surface coplanar with the vertex of the metrology system at that siderostat. Such a mirror might form part of a future science optics chain.

Laser Metrology

A six-axis laser metrology system forming an optical tetrahedron (Figure 3) will provide the primary measure of control effectiveness. One vertex is located at each of the three mock siderostats with the fourth vertex containing the out-of-plane reference point. The outputs of the near and far legs will yield relative displacements among the vertices with the minimum number of laser axes. The vertices of the optical and structural tetrahedrons typically do not coincide since the siderostat locations were chosen to represent non-redundant baselines without necessarily requiring rigid body tilting of the entire instrument. In the initial configuration, one siderostat plate will be located near one structural vertex; the others are roughly 1/2 and 1/3 of the distance down two different legs. The relative angles between the actively-mounted cat's eyes will be less than 96.5 degrees, which is within the cone of operation.
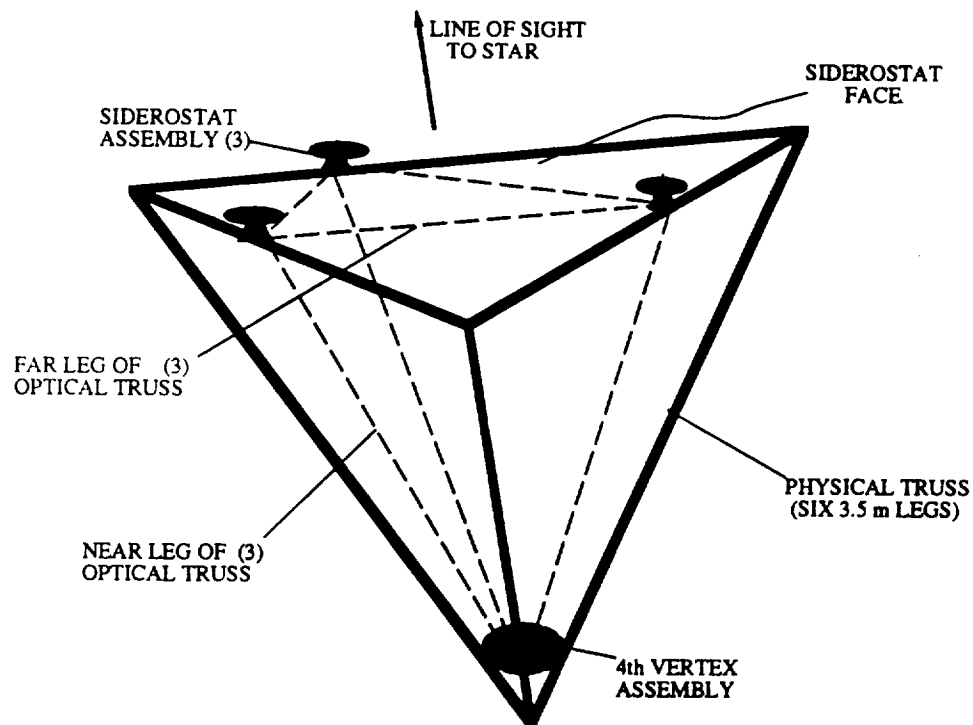

Figure 3: Illustration of the Structural and Optical Tetrahedral Trusses

The power required to operate six axes, instead of the nine that would be needed to determine $\Delta x, \Delta y, \Delta z$ for the three siderostats, permitted the use of a commercially available laser measurement system using a single laser head mounted on the testbed. We are using a dual-frequency stabilized laser head (670 µW total power), detectors, and fringe counting electronics manufactured by Hewlett-Packard Corporation. A lens and 45-degree polarizer assembly plus a short length of optical fiber allow the detector electronics packages to be located out of the way of

the measurement optics and associated mounting fixtures. The VME-based fringe counting electronics provide a seamless link to our real-time control computer.

Figure 4 details one measurement axis. The measurement resolution is limited by the HP-supplied electronics to $\lambda/64$ at $\lambda = 633$ nm, or approximately 10 nm. Greater resolution can be obtained with alternate electronics, such as the VME modules developed by Mike Shao's group at JPL. For operation in air without wavelength tracking over short time scales and in a laboratory disturbance environment, we feel that 10 nm resolution will be adequate. Our closed loop control frequency range is 2-200 Hz, so changes in the refractive index of air and other sources of error with long time constants will not pose any problem. A preliminary error budget suggests that measurement resolution will be ~ 17 nm.
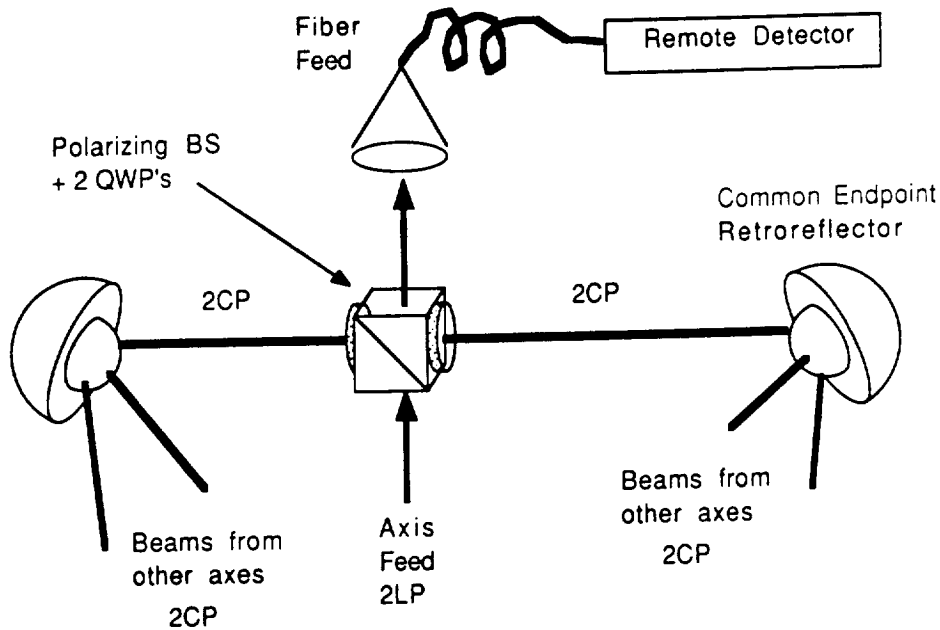

Figure 4: One Axis of the Laser Metrology System

Cat's Eye Retroreflectors

Cat's eye retroreflectors will be used to provide wide fields of view at the vertices of the optical tetrahedron. These are similar to cat's eyes used by C. Townes (UC Berkeley $10\mu m$ interferometer) and D. Hutter (US Naval Observatory Astrometric Interferometer) although in this application there is no siderostat slew range to contend with. The minimum size of the cat's eye for a given amount of spherical aberration is a function of the laser beam diameter and the refractive index of the cat's eye glass. The metrology laser beam diameter of 6 mm at the laser head led to a cat's eye size and mirror mass which was unnecessarily cumbersome for implementation on a moving platform. Reducing the beam diameter permits the cat's eye size to be reduced while maintaining the same spherical aberration performance. Lenses reduce the collimated beam diameter to 4 mm without reducing the available power. The cat's eye parameters are:

glass index at 633 nm	1.72 (Schott SF 10)
radius of small hemisphere	25 mm
radius of large hemisphere	34.7 mm
max. ΔOPL across beam cross section	$\lambda/10$
mass	511 g
usable field of view:	+/- 60 degree cone (see Figure 5)

Input
beams

AR
coat

$r2$

rL

120°
cone

silver + overcoat

common center

Figure 5: Cat's Eye Retroreflector

Near Leg   Far Leg Feed

Near Leg

Far Leg Feed

10 in

Laser head & power
splitting optics mounted
underneath bottom plate

Beam
Steerer

5 in

Legend

Rcvr Fiber Input
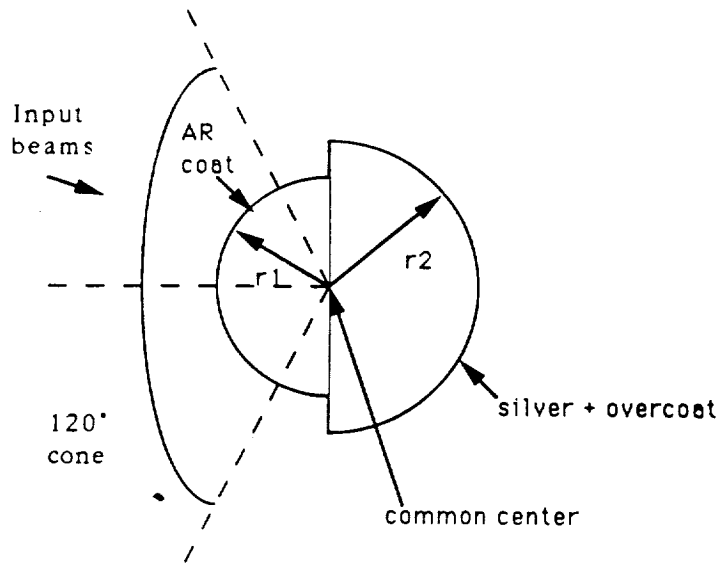
Retroreflector

Pol. BS + 2 QWP

Beam Steerer

Near Leg Optics
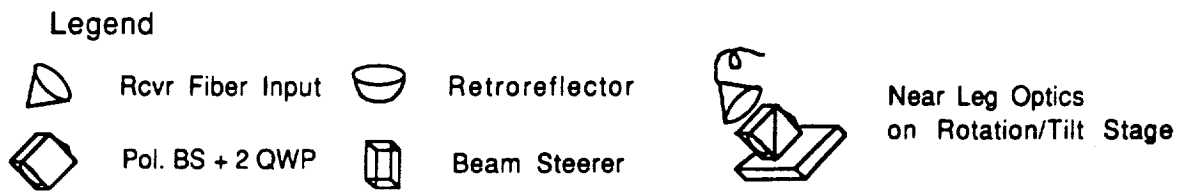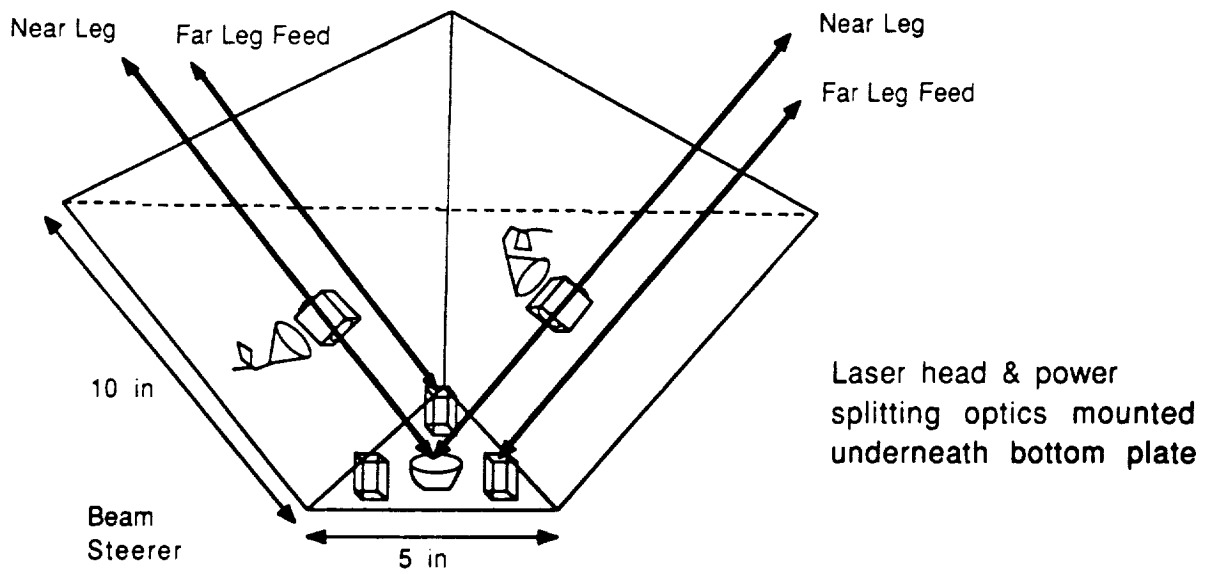on Rotation/Tilt Stage

Figure 6: Layout of Fourth Vertex

Modifying the radii to generate a small amount of focusing will help counteract the increased divergence of the smaller beam diameter and produce better overlap at the detectors. The curved surface of the large hemisphere will have a silver reflective coating with a protective overcoat. The curved surface of the small hemisphere will be coated with a broadband anti-reflective coating targetted to be the proper thickness for λ = 633 nm at half the cone angle. Anti-reflective performance at other angles will depend on the spectral response of the coating. The hemispheres will be aligned after coating and joined by optical contacting.

Other Optics

The remainder of the optics for each measurement leg consists of a polarizing beamsplitter cube with crystal quartz quarter wave plates cemented to opposite faces, plus the associated feed optics. Each beamsplitter-waveplate assembly is mounted in a semi-custom mount which provides the adjustment degrees of freedom needed to align the measurement beam with respect to its retroreflector endpoints. Three of these mounts are rigidly attached to an open pyramidal "bucket" that is itself rigidly attached to the main fourth vertex optics plate (Figure 6). The remaining three mounts are rigidly attached to the siderostat optics plates (Figure 7) in the far leg measurement paths. These rigid mounts are designed to prevent motion of the beamsplitter optics from appearing as motion of the retroreflectors. The feed optics must maintain the orthogonality of the laser polarizations through complex bends in order to minimize errors due to polarization mixing.
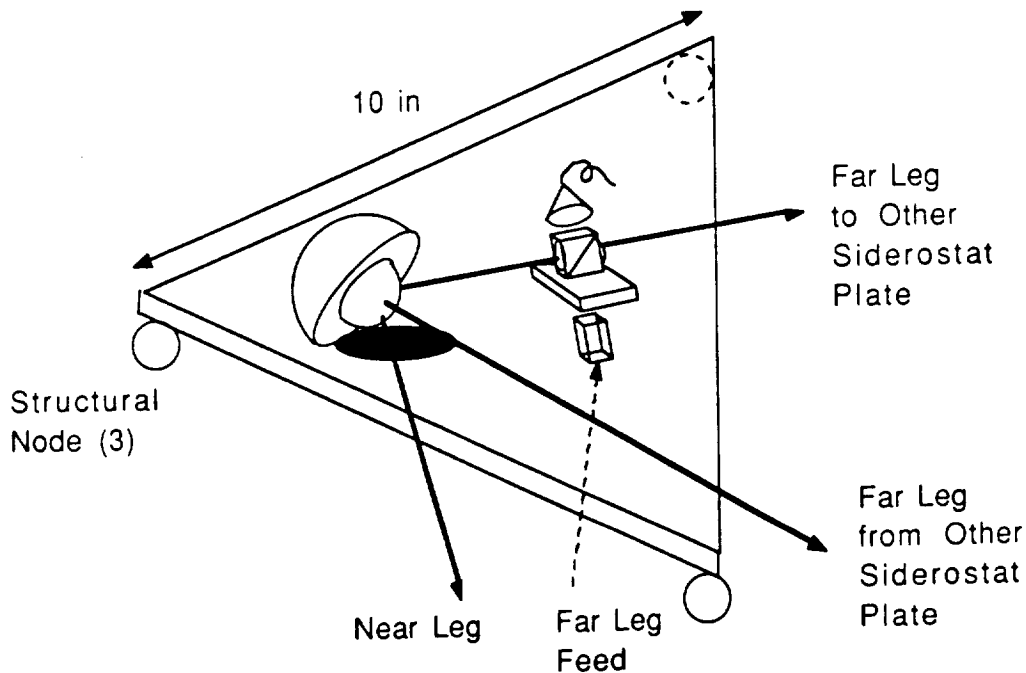

Figure 7: Layout of Siderostat Plate

Results from Recent Testbed-Related Research

In conjunction with the development of the testbed, several other areas of research are being pursued. Three studies have been completed, and are documented elsewhere [1-3]. Some relevant results are summarized below.

Systems Level Disturbance Minimization Using Controlled Structures Technology

Disturbances present on a typical large space-based observatory are detailed. The spectrum of disturbances is divided into those which depend on the space (Earth orbital) environment and those which are internal. Various CST techniques for minimizing the effect of disturbances on mission requirements are reviewed. These include passive structural tailoring, passive damping, vibration isolation, and active structural control. The full-scale 35-meter baseline version of the interferometer testbed is used as a case study for evaluating the flowdown of systems level information to the structural requirements. The power, attitude control, and interferometer and metrology subsystems are discussed with respect to their role as disturbance sources. Finally, an approach for systems level disturbance minimization is outlined.

Experimental Characterization of Damping at Nanostrain Levels

In light of the increasing trend towards nanometer-level requirements on structural stability, it was considered beneficial to characterize damping at extremely small displacement and strain levels. There has been discussion in the CSI community recently regarding dynamic behavior of structures at extremely low vibration levels. In particular, it was not known whether there was a radical change in properties below a particular vibration or displacement floor. In this study, damping was measured in aluminum and graphite/epoxy material specimens in air and in vacuum, and in the bare interferometer testbed truss. It was demonstrated that material damping was independent of strain from ten microstrain down to one nanostrain. Excellent correlation with thermoelastic material models was obtained. Damping in the testbed was found to be independent of strain below one microstrain (Figure 8). The linearity can be exploited by doing system identification at micron displacement levels instead of nanometer levels. The results were immediately instrumental in allowing the use of relatively inexpensive accelerometers for system identification on the testbed, rather than the extremely accurate high cost sensors.
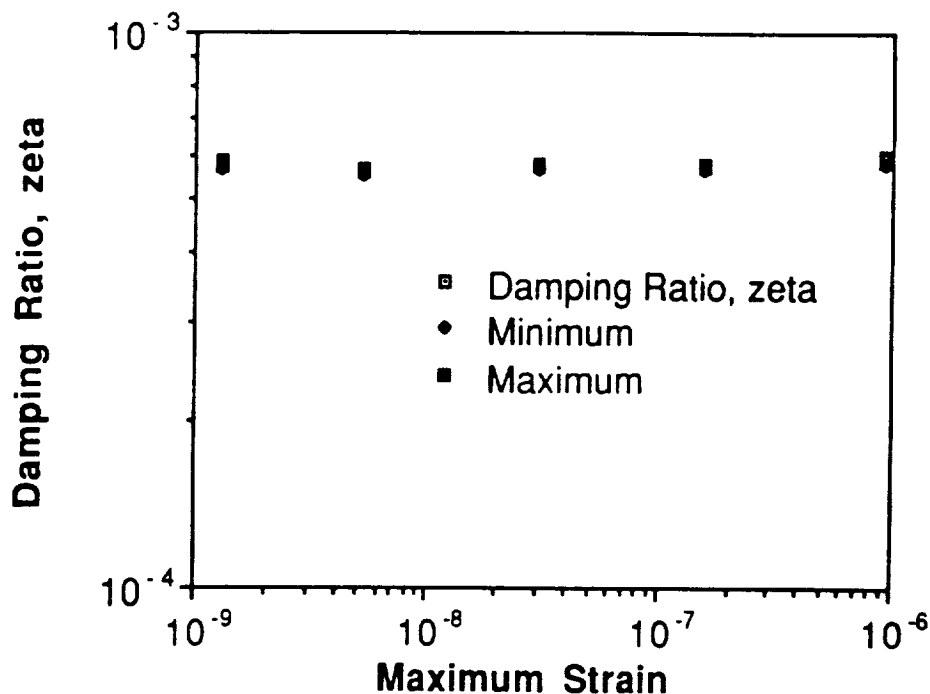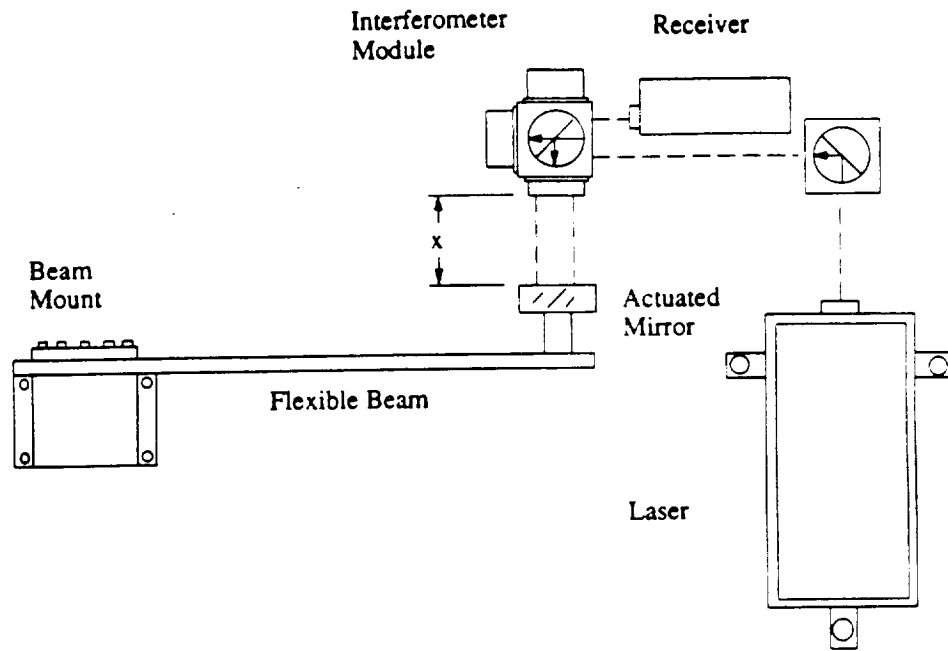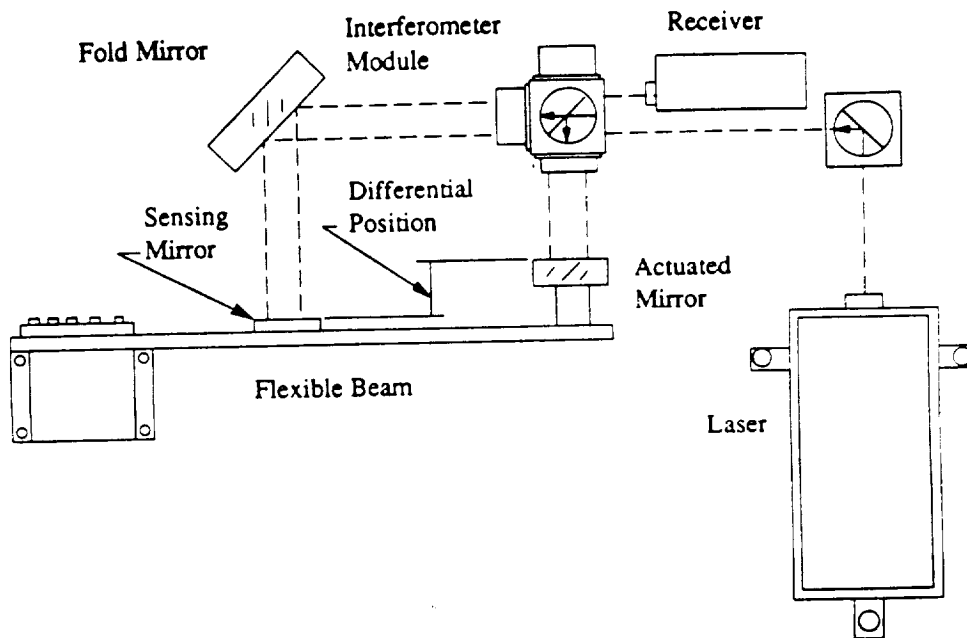

Figure 8: Experimentally Determined Damping in 44 Hz Testbed Mode

a)   Collocated Sensor-Actuator Set-up

b)   Non-Collocated Sensor-Actuator Set-up

Figure 9: Experimental Approach for Investigating Path Length Control

Experimental Demonstration of Nanometer-level Active Control of a Flexible Beam

In this approach to structural control, the flexibility of the structure is ignored to the greatest extent possible. Instead of controlling the structure, a mirror mass was moved to maintain an optical path length in the presence of disturbances propagating through the structure (Figure 9) using a control strtegy that ignored the structural dynamics of the flexible base structure. The approach was successful provided that the actuated mass was small compared to modal masses of the structure. The effect of damping was investigated and quantified. An order of magnitude

reduction in vibration levels was demonstrated (Figure 10). This concept--implemented only for a single input single output case--will be extended to the interferometer testbed, where active mirror mounts will be used to position the cat's eye retroreflectors in three displacement degrees of freedom. Preliminary analysis of the finite element model suggests that the ratio of the moving mirror mass to the modal masses of the structure are small enough to allow the design of a high performance stable controller without further considerations of the structural dynamics. Research into active isolation will focus on the extension of this approach to cases involving noncollocation, multiple flexible modes, and multi input multi output systems.

	Motion (rms) (0-20,000 Hz)	Attenuation	Motion (peak) (0-20,000 Hz)
Fixed Block Uncontrolled	17 nm		16 nm
Controlled	0.77 nm	-27 dB	5 nm @ piezo mode
Collocated			
Uncontrolled	77 nm		250 nm @ 1st mode
Controlled	3.1 nm	-26.8dB	11 nm @ piezo mode
Non-Collocated (x=0.5)			
Uncontrolled	45nm		190 nm @ 1st mode
Controlled	3.9 nm	-21.2 dB	10 nm @ piezo mode

Figure 10: Results from Path Length Control Experiment

Finite Element Model

The purpose of the finite element model is to provide a basis for analytical studies of structural modification, and to serve as one basis for control design. The accuracy of the finite element model is verified by comparison of frequencies and mode shapes with an experimentally derived modal model. It is not likely that the model will be used for control design if experimental models are available. The effort in finite element modelling is outlined in Figure 11.

Two finite element models have been constructed using ADINA: a continuum beam model and a model which contains separate elements for each strut. The continuum model has sufficient accuracy to make it useful for examining various approaches to control. Some features of the models are described below.

Continuum Model
- Equivalent continuum cross-sectional properties for each leg of the truss were derived. (The six legs have identical cross-sections.)
- Each of the six legs was then modeled with 14 Timoshenko beam elements.
- The first flexible mode is at 38 Hz.
- The low mode shapes are characterized by 1st and 2nd bending and the torsion of individual legs.

Continuum Model	Full Struts Model	Correlation with Modal Model	Parametric Studies
equivalent beam properties	strut stiffness and joint mass	ADINA-matlab link	disturbance-to-performance metric t.f's
geometry	geometry	frequencies, mode shapes	system i.d. shaker location/direction search
frequencies, mode shapes	frequencies, mode shapes	iteration	passive damping location search
documentation	iteration on properties		active member location search
adjustment based on system id	modelling of additional hardware (vertices,optics), iteration		point impedance calculation
	choose strut locations		
	testbed global damping measurement		

Figure 11: Near Term Efforts on Testbed Finite Element Model

Full Struts Model
- There are 228 nodes representing the aluminum joints.
- Each of the 696 struts is modeled with a Timoshenko beam.
- The first flexible mode is at 34.56 Hz.
- The model runs in under 2 minutes on the Cray II.
- The low mode shapes are characterized by 1st and 2nd bending and torsion of the individual legs.
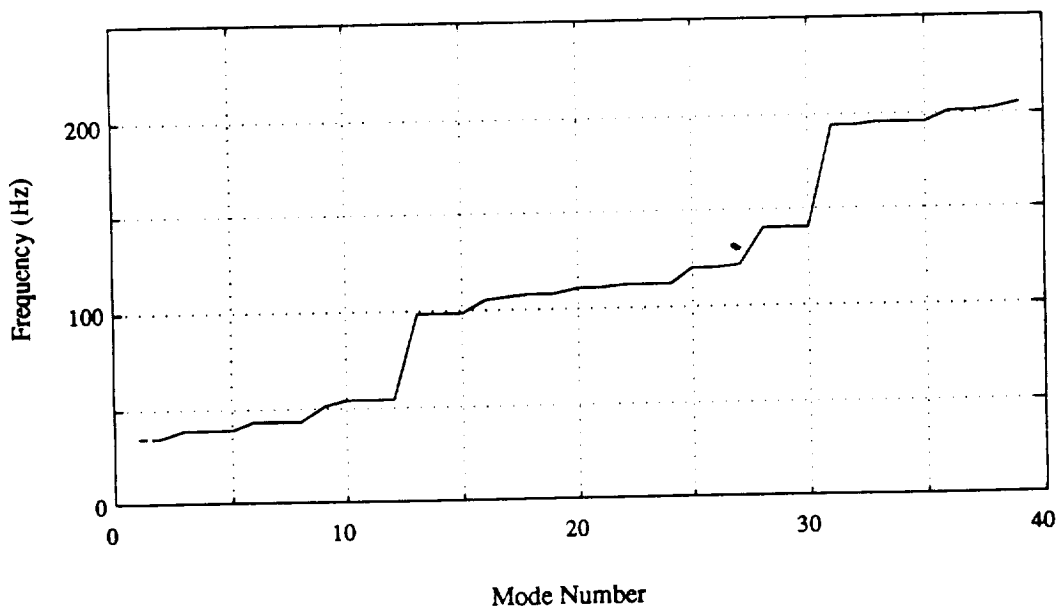- There are 35 flexible modes below 200 Hz.

Figure 12: Frequency Distribution of First 39 Finite Element Modes

Distribution of Modes

Figure 12 shows the frequency vs. mode number for the first 39 modes based on the full struts model. Because of the inherent symmetry of the structure, there are repeated eigenvalues (multiplicity 2 or 3) present. Further, there is a separation between clumps of modes from 54-98 Hz and from 142-194 Hz. The repeated roots and clumping of modes will disappear once concentrated mass of the three siderostats and the fourth vertex are added. Also, the added mass will drop the frequencies further so that there will be more than 50 modes below 200 Hz.

Matlab Postprocessing

The eigenvectors from the full struts model have been used to calculate strain energy distributions for each mode. The elements can be ranked from most to least strain energy by mode or sum of modes. This information will be used to choose passive damping element locations, and later as an initial criterion for active member location selection. With an improved model (including optics) we will be able to calculate a rough optical path performance metric to rank locations on an 'open loop' controllability basis (*i.e.* without simulating performance of the closed loop system).

In separate work, a two-dimensional truss model has been used as a sample problem to develop necessary tools for control based on state-space models from the ADINA output. Implications of the close modal spacing and light damping are being studied.

Addition of Damping

The finite element model will be augmented with experimentally determined damping values. In addition, damping will be added in select elements in conjunction with the viscoelastic struts experiment. A more careful study optimizing passive damping locations will be carried out later.

Role of the Finite Element Model

The finite element model in its current form is a useful tool for parametric studies, mode shape visualization, calculation of strain energy distributions, and selection of system ID accelerometer locations. We have improved the accuracy of the model, but it is still not perfect. With initial ID data we will be able to make a direct comparison between finite element and experimental data.

At some point a broader discussion of the role of finite element models in CST may be in order. There are several points which must be addressed. From the academic perspective at SERC, these include:

- The 'need' to develop a highly accurate finite element model because it is standard practice in industry.
- The value of a finite element model for laying out identification and control architectures
- The inadequacy of finite element models as a basis for control in a complex lightly damped structure
- The relative value of finite element models and experimental system identification
- The realistic potential for on-orbit system identification
- The need for an accurate finite element model if system identification is not possible
- The role of a hybrid approach which could include subscale and component identification

System Identification

A system identification is routinely performed on controlled structure testbeds as a prelude to control experiments. To date, the interferometer testbed is the most complex structure to be identified in SERC. The experimental model derived from the system ID will serve two purposes. First, it will allow verification of the finite element model. Second, it will provide a modal model for control design.

Because of the complexity of the optics, the testbed will not reach its 'final' configuration for some time (late fall 1990). However, an initial ID will be performed in order to provide verification of the naked truss finite element model. The structure and model will be sufficiently complicated later so that tracing sources of error will be difficult. In addition, the initial ID will allow us to become familiar with the recently-purchased software and hardware systems. The ID will be done with an external shaker and roughly 32 or more accelerometers. Later, active members installed in the truss will be used for system ID.

Initial tests show several interesting results. The first flexible mode was measured at 31.34 Hz, compared with a finite element prediction of 34.56 Hz. This 10% error indicates a need to revise the finite element model, with input from a subcomponent stiffness test on the struts. The effect of gravity is apparent in the structure. Modes which are nominally the same frequency differ by typically 0.3 Hz. Also, pendulum and bounce suspension modes have been measured (below 4 Hz). Finally, typical damping ratios of 0.04% to 0.07% have been recorded for the flexible truss modes, with minimal intrumentation and cabling on the structure.

Frequency Resolution
Due to memory limitations of the identification computer, frequency resolution is currently at best 0.0125 Hz. This may not be acceptable for lightly damped modes present in the testbed.

Generation of the Modal Model
The Structural Measurement Systems STAR software will provide frequency domain fits over limited frequency ranges. These will be assembled in Matlab where the full modal model will be constructed. This model will initially contain roughly 100 states.

Passive Damping

Viscoelastic	Shunted Piezoelectric	Viscous Dashpot	Proof Mass
material properties (Poron, Scotchdamp)	small truss experiment	survey available hardware	Hardware available in lab
design	active member impedance selection	confer with Honeywell	Harris precision device
construction	analysis (resistive, resonant)	evaluate inexpensive design concepts	select locations
test in small truss	electrical components		testbed damping measurements
component tester	component tester		
choose strut locations	choose strut locations		
testbed global damping measurement	testbed global damping measurement		

Figure 13: Near Term Efforts on Passive Damping Augmentation

A passive-as-possible approach is preferred in achieving a spacecraft which must meet stringent shape or pointing requirements. However, in an environment which will include several

potential disturbance sources, some sort of vibration alleviation will also be necessary. The introduction of an active control system can greatly improve performance at the expense of complexity, cost, and the possibility of instability. Passive damping augmentation is a far less glamorous, but nevertheless effective alternative. When an active structural control system is considered necessary, passive damping can only be beneficial. It does not make sense to implement aggressive structural control on a plant with only 0.05% inherent damping. Our initial goal is to conduct enough tests to establish the basis for later comprehensive experimental studies of passive damping schemes to be carried out in the future. The program has been broken into four areas representing different approaches to passive damping. These are shown in Figure 13.

Viscoelastic
        Constrained layer viscoelastic struts have been tested in a small cantilevered truss. Poron and Scotchdamp materials were compared, and Scotchdamp was found to be more effective. The effectiveness of different Viscoelastic layer thicknesses has been judged based on ringdown experiments in a first bending mode. A significant component of the strain energy of the structure is in the damper strut. This allowed high loss factors (25 %), and large drops in frequency.
        Twelve of these simple highly effective struts have been manufactured. With information from the component tester, it will be possible to model the struts with equivalent axial stiffness and viscous damping. This information will be integrated into the finite element model where a prediction of the added global damping due to several viscoelastic struts is possible. A repeat of the ID experiments will yield a measured value for damping.

Shunted Piezoelectrics
        A resistively-shunted strut [4] was built and tested in a small cantilevered truss. The initial results were discouraging, with damping values below those expected. Subsequent re-engineering of the strut yielded no improvement. The use of a commercial Physik Instrumente actuator in the strut gave no better results. Although the experiment was designed to concentrate a large amount of strain energy in the piezoceramic material, this was apparently not the case. A careful test of the strut in the component tester will provide an accurate accounting of strain energy distribution. The active member actuator stiffnesses were selected with consideration of appropriate stiffness properties for the shunting application in the large testbed.

Concerns
        The difficult problem we face in adding significant global damping is the large number of struts (696) in the testbed. The damping members must be selectively placed, perhaps near critical payloads. At this point, the constrained layer Viscoelastic struts are by far the least expensive and easiest to make. Drawbacks include the frequency-dependent loss factor and material propertytemperature sensitivity. The shunted piezoceramics are potentially more effective than we have demonstrated to date, but are expensive. A device based on the Honeywell D-Strut design, which is capable of broadband viscous damping and is relatively temperature-independent is desirable, but is at this point prohibitively expensive to incorporate into the testbed.

Component Tester

        An axial component tester has been constructed and is operational on an optics bench. This facility includes a Physik Instrumente piezoceramic strut to drive various test articles which represent subcomponents of the testbed. Mainly, these are passive or active replacements for the aluminum struts. Load and displacement are measured, the latter with a Zygo Axiom 2/20 interferometer system. The tester will be used in the 0.1-200 Hz frequency range, with displacements from 1 nm to 60 μm. Initial measurements to be conducted are:

- stiffness of truss longerons and diagonals
- stiffness of active struts
- voltage/deflection plots of active struts
- viscoelastic strut characterization

The facility will be available in the future for characterization of other passive or active components.

Control Experiments

We do not forsee having the capability to do absolute shape control in the near future, since that requires rigid body control of the testbed. The initial effort involves separation of the structural control and optical metrology path length control loops. Capabilities will be established in each through simple closed-loop experiments. Figure 14 shows the near term goals for control experiments.

Software		Structural Control	Optical Path Control
Integration with hardware	**User environment**	number of actuators	mirror mount dynamics
interface to laser metrology	streamlining	active member characteristics	accelerometer measurements
integration of vector processor	matlab links (pseudo-autocode)	actuator locations	interferometer measurements
tradeoffs between number of states vs. speed (benchmarks)	input/output displays	control design	single axis piston
data storage capability	input/output saturation flags	collocated velocity	multi-mirror, multi-axis
matlab links	internal state displays	collocated force and strain	
	documentation	optical performance measure	

Figure 14: Near Term Efforts on Control Experiments

Model Basis for Control Design

There are several methods for generating a model which is a suitable basis for control design. These include finite element models (usually augmented with experimental damping values), measured models based on modal models from system identification, and measured models based on direct information from input-output actuator-sensor pairs. The third approach is preferred if the proper measurements can be made. For all these designs model reduction may be necessary in the plant and controller.

Real Time Software

The software to do linear, constant coefficient, digital control is functionally complete. The code is called *MatCon* for matrix control. The user interface is through Matlab, where a typical continuous control design is discretized. The discrete matrices and some other constants (number of inputs, outputs, and states, scaling factors, and the sampling period) are saved in a standard Matlab *.mat* file. The real-time computer then reads this data and starts the controller. The following algorithm is used.

$$input \ vector \ y \ from \ A/D$$

$$x_{n+1} = F_{11} x_n + F_{12} y_n$$

$$u_n = F_{21} x_n$$

$$output \ vector \ u \ to \ D/A$$

$$wait \ for \ next \ sample \ time$$

While the controller is running the user can stop and start the controller, record states, inputs, and outputs, and scale inputs and outputs. The data file of input vectors is stored in on-board memory, until a set number of samples has been saved. The controller is then stopped and the data transferred to the hard disk on a Sun Sparcstation, where it can be read back into Matlab. States and outputs can be reconstructed from the saved input data for full analysis. There is a direct interface to the six HP laser measurement boards. Four-pole Bessel anti-alias filters with a corner frequency set by digital input-output from the real-time computer are used. The filter cards also provide a digitally programmed gain of 1,2,4,8,or 16 to help amplify low-level sensor signals. We will have the capability to process 16 inputs, 10 outputs, 32 states at 1kHz. The control bandwidth is not expected to exceed 150 Hz.

Active Struts

The active strut design is shown in Figure 15. In addition to the load cell and internal strain gage measurements, two accelerometers are mounted to the strut to provide an inertial collocated measurement and to permit system identification using the active struts. Three struts are currently available, and an additional homemade unit will initially be used as a disturbance source generator.
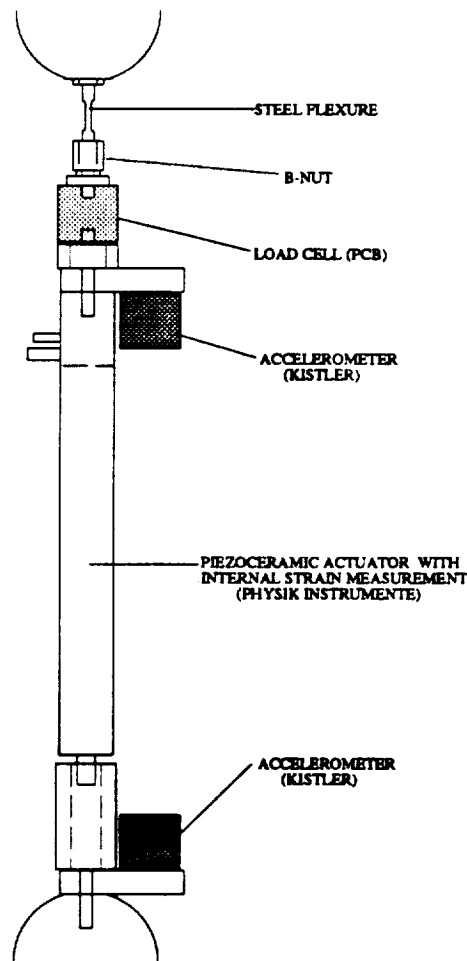

Figure 15: Active Strut Configuration

Active Mirror Mounts

Active mirror mounts will be used to maintain to $\lambda/20$ the linear positions of the cat's eye retroreflectors, which are located at the three mock siderostat locations shown in Figure 3. Output position control will be achieved by moving the cat's eye and mounting table using three microactuators: 0.7" piezoelectric stacks for two of the active mirror mounts and 0.4" electrostrictive stacks for the third, as shown in Figure 16. The actuators will be run in common mode to actuate piston, or z, motion of the point M of the cat's eye. In differential mode, the cat's eye and table will be tilted; resulting in x and y displacements through the lever arm and flexure assembly. The rotations and lateral displacements cannot be controlled independently, but this constraint will not be a problem for the envisioned set of control experiments in the near to medium term. Simultaneous displacements of +/- 3.5 µm can be achieved in all three directions. The mirror mount design includes the flexibility to introduce additional mass to simulate the scaled mass of the retroreflectors. Additionally, the mounts can later be modified to incorporate mass reactuation, where the he effect of moving the mass of the cat's eye is reduced or even cancelled. The result will be a reduction in the interaction between the mirror control system and the truss flexibility.
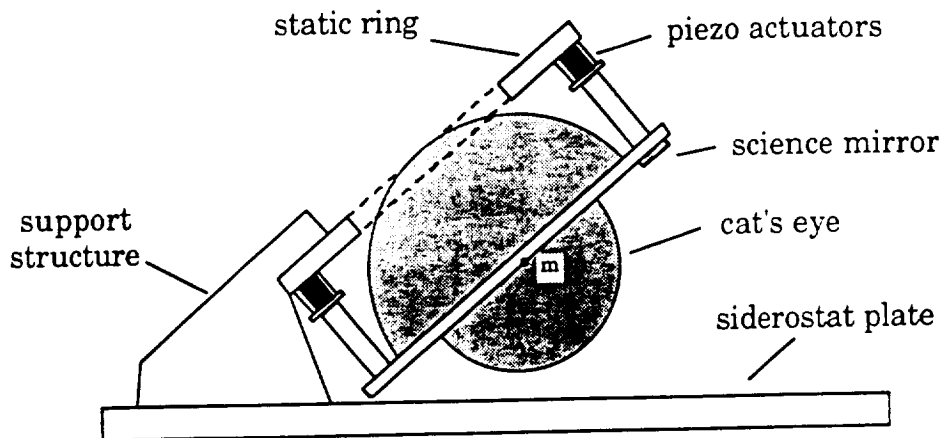

Figure 16: Active Mirror Mount Functional Drawing

The active mirror mount is a small stroke device intended to control only path length errors in the flexible truss. These errors will result from disturbance sources that are introduced intentionally to simulate space disturbances and from disturbances present in the ambient noise environment of the laboratory. Figure 17 shows the ambient acceleration power spectral density (PSD) in the worst-case direction measured by a triax of moderate-sensitivity accelerometers (1V/g) at a proposed active mirror mount location on the truss. In this very preliminary study, the structural dynamic response, starting at 30 Hz, is also corrupted by electrical noise and various lower frequency suspension modes. A displacement PSD is calculated by scaling the acceleration PSD by $1/\omega^4$, which leads to an estimate of rms displacement of 22 nm in the frequency band of 20-100 Hz. Assuming that a point corresponding to a siderostat on another leg experiences the same disturbance and vibrates out of phase with the first point throughout this frequency range, an ambient path length error of 44 nm rms can be expected. The actual error may be less once electrical noise is removed and the additional mass of the active mirror mounts is added to the truss.

Electrostrictive Actuators

In separate work [5], electrostrictive ceramic PMN:BA, a material of interest to structural control engineers, was characterized for test parameters of frequency, amplitude, and temperature. Results indicate that at room temperature the material strain response is quite linear with almost
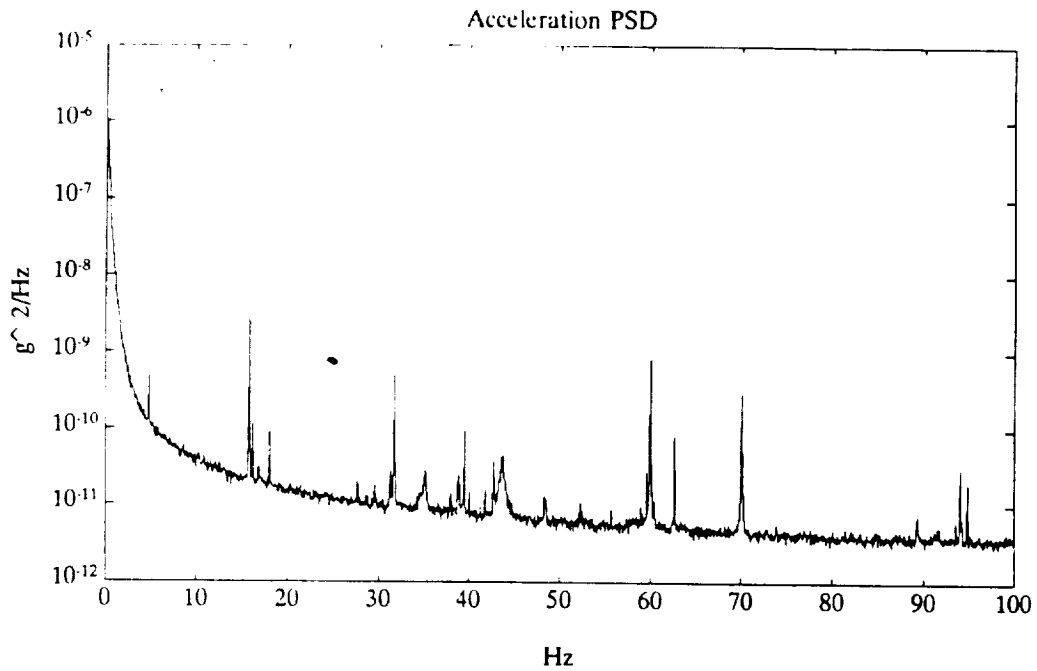

Figure 17 Acceleration Power Spectral Density in Worst-case Direction at Proposed Active Mirror Mount Location
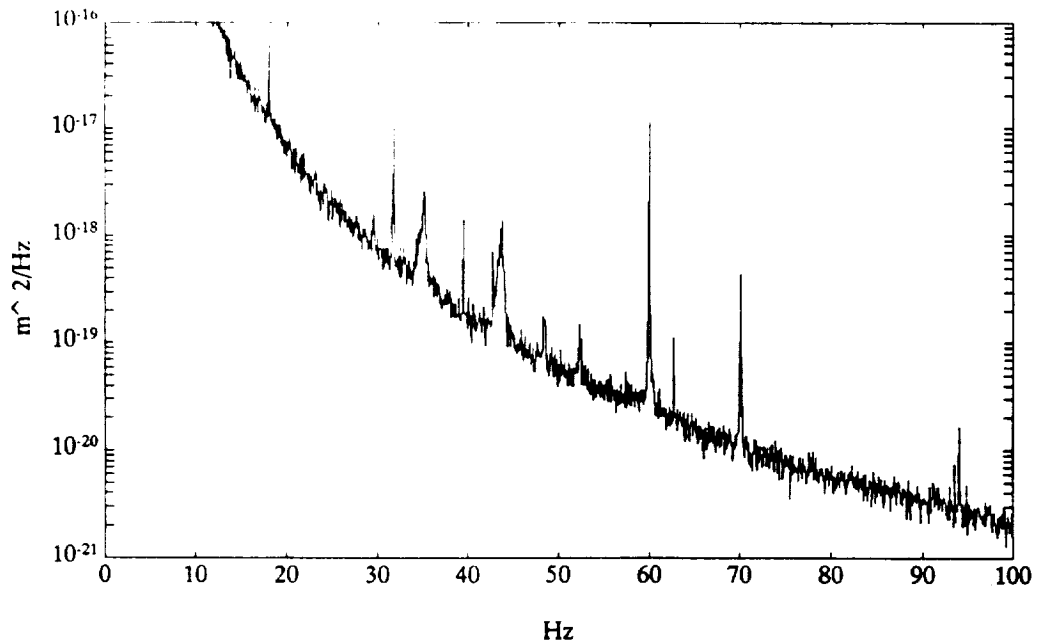

Figure 18 Displacement Power Spectral Density in Worst-case Direction at Proposed Active Mirror Mount Location (Derived from Acceleration Measurement)

no phase due to hysteresis, unlike piezoelectrics, and is constant with frequency. However, the induced strain sensitivity is highly dependent on temperature, and hysteresis increases rapidly below room temperature. Since electrostrictive actuators will be used in one of the three active

mirror mounts, the operating temperature of the actuators will need to be monitored during calibration and usage.

Summary

The SERC interferometer CST testbed will soon be fully operational. The facility will address concerns regarding extremely tight constraints imposed on structural motion in future space observatories. At the same time, the testbed will serve as a platform for exploration of a broad range of controlled structure technologies and approaches.

References

1 Eyerman, C.E., A Systems Engineering Approach to Disturbance Minimization for Spacecraft Utilizing Controlled Structures Technology, MIT Dept. of Aeronautics and Astronautics,S.M. thesis, May, 1990, SERC Report 2-90.

2 Ting, J., Characterization of Damping of Materials and Structures at Nanostrain Levels, MIT Dept. of Aeronautics and Astronautics,S.M. thesis, May, 1990, SERC Report 1-90.

3 Garcia, J.G., Stability of an Actuated Mirror on a Flexible Structure as a Function of Mass and Structural Damping, MIT Dept. of Mechanical Engineering, S.M. thesis, June, 1990.

4 Hagood, N.W. and von Flotow, A.H., 'Damping of Vibrations with Piezoelectric Materials and Passive Electrical Networks,' accepted for publication in *Journal of Sound and Vibration*.

5 Blackwood, G.H. and Fleming, F.M., Characterization of Transverse Field-Induced Strain in PMN:BA Electroceramic Plates, MIT Space Engineering Research Center Report #7-90, July, 1990.

August 8, 1990

Dr. Stephen Synnott
M.S. 301-125L
Jet Propulsion Laboratory
4800 Oak Grove Drive
Pasadena, CA 91109

Dear Steve:

I have enclosed the paper based on our presentation at the Workshop on Technologies for Space Interferometry held at JPL last spring for inclusion is the volume you are assembling. Please contact me at 617/253-6685 or Tupper Hyde at 617/253-5243 with any questions.

Sincerely,

Eric Anderson

On a Cost Functional for $\mathcal{H}_2/\mathcal{H}_\infty$ Minimization

Douglas G. MacMartin, Steven R. Hall*
Space Engineering Research Center
Department of Aeronautics and Astronautics
Massachusetts Institute of Technology
Cambridge MA 02139

Denis Mustafa[†]
Laboratory for Information and Decision Systems
Massachusetts Institute of Technology
Cambridge MA 02139

Abstract

A cost functional is proposed and investigated which is motivated by minimizing the energy in a structure using only collocated feedback. Defined for an $\mathcal{H}_\infty$–norm bounded system, this cost functional also overbounds the $\mathcal{H}_2$ cost. Some properties of this cost functional are given, and preliminary results on the procedure for minimizing it are presented. The frequency domain cost functional is shown to have a time domain representation in terms of a Stackelberg non-zero sum differential game.

Introduction

This paper examines the properties, evaluation algorithm, and an optimization approach for a cost functional for combined $\mathcal{H}_2/\mathcal{H}_\infty$ control. Combined $\mathcal{H}_2$ and $\mathcal{H}_\infty$ control is of interest since it combines the problems of nominal performance and robust stability. Related work includes $\mathcal{H}_2$ optimization with an $\mathcal{H}_\infty$ constraint [1–4], minimum entropy $\mathcal{H}_\infty$ control [4,5], and mixed $\mathcal{H}_2$ and $\mathcal{H}_\infty$ control [6,7]. The cost functional of interest to us is defined as follows.

Definition 1 *Consider a system $H(s) = [H_0(s)\ H_1(s)]$ and a number $\gamma \in \mathbb{R}$, with $H_0 \in \mathcal{RH}_2$, $H_1 \in \mathcal{RH}_\infty$, and $\|H_1\|_\infty < \gamma$. Then the cost $L(H,\gamma)$ is defined by*

$$L(H,\gamma) := \frac{1}{2\pi} \int_{-\infty}^{\infty} \text{trace}\left\{ (I - \gamma^{-2} H_1 H_1^*)^{-1} H_0 H_0^* \right\} d\omega \quad (1)$$

The specific form of this cost is motivated by minimizing the total vibrational energy of a structure with only a model of the local dynamics near an actuator and collocated sensor. Previous work with this type of model has used $\mathcal{H}_2$ [8] and $\mathcal{H}_\infty$ [9] optimizations of the power flow. Briefly, the fraction of the input power flow that is reflected into the structure at the actuator location is a quadratic at each frequency, and can be represented by a transfer function HH^*. The fraction of the power that is dissipated is then $(I - HH^*)$, and the total power dissipated is $(I - HH^*)E$ where E is the structural energy as a function of frequency. If the power flow into the structure from external disturbance sources is given by $\Phi(j\omega)$, then a power balance yields that the total energy in the structure is given by $L([H\ H\Phi], 1)$. A more detailed explanation may be found in [10].

In [7], a framework for mixed $\mathcal{H}_2/\mathcal{H}_\infty$ control problems is considered. There the cost functional is motivated in an input/output sense. The system is subject to two inputs, one of bounded spectrum, and the other with bounded power. For the case where the first input signal is white and the second is causal, necessary and sufficient conditions are given for the existence of a controller which minimizes the cost. The non-white and non-causal case is

described but not solved (see Section 3.3.) This case is, however, of particular interest as the cost then equals $L(H,\gamma)$, revealing a close relationship between the present approach and the approach taken in [7]. This connection is currently under investigation.

The final section of this paper gives a third interpretation of this cost in terms of a Stackelberg non-zero sum differential game.

Properties

The following basic properties of $L(H,\gamma)$ will be stated without proof, and can be easily shown to hold.

Proposition 2 *Let $H(s)$ and γ satisfy the conditions in Definition 1. Then*

(i) $L(H,\gamma)$ *is well defined.*

(ii) $L(H,\gamma) \geq 0$, *and* $L(H,\gamma) = 0 \iff H_0 = 0$.

(iii) $L(UHV,\gamma) = L(H,\gamma)$ *for any* $U, V \in \mathcal{RL}_\infty$ *with* $U^*U = I$, $VV^* = I$.

In the case where $H_1 = H_0$, further properties of the cost $L(H,\gamma)$ can be established by relating it to the entropy $I(H,\gamma)$ of a system defined, for example, in Reference [5].

Definition 3 *For $H \in \mathcal{RH}_2$, $\gamma \in \mathbb{R}$, and $\|H\|_\infty < \gamma$, the entropy at infinity is defined by*

$$I(H,\gamma) := -\frac{\gamma^2}{2\pi} \int_{-\infty}^{\infty} \ln \left| \det \left(I - \gamma^{-2} H^* H \right) \right| d\omega \quad (2)$$

Also let $C(H)$ be the usual $\mathcal{H}_2$ cost associated with the system H;

$$C(H) := \frac{1}{2\pi} \int_{-\infty}^{\infty} \text{trace}\left\{ H^* H \right\} d\omega \quad (3)$$

Proposition 4 *For $H = [H_0\ H_0]$, with H_0 and γ satisfying the conditions in Definition 3, consider the cost $L(H,\gamma)$, the entropy $I(H_0,\gamma)$, and the $\mathcal{H}_2$ cost $C(H_0)$. Define $\xi = \gamma^{-2}$, then*

(i) $L(H,\gamma) = \frac{\partial}{\partial \xi}(\xi I(H_0,\gamma))$

(ii) $L(H,\gamma) \geq I(H_0,\gamma) \geq C(H_0)$.

Proof: The first assertion follows directly from the proof of Proposition 2.3.2 in Reference [5]. The first inequality in (ii) follows from $L(H,\gamma) = I(H_0,\gamma) + \frac{\partial}{\partial \xi}(I(H_0,\gamma))$ and the result from Proposition 2.3.2 in [5] that $\frac{\partial}{\partial \xi}(I(H_0,\gamma)) \geq 0$. The final inequality is obtained from the result that $I(H_0,\gamma)$ itself bounds the $\mathcal{H}_2$ cost. □

That $L(H,\gamma)$ overbounds an $\mathcal{H}_2$ cost can also be shown to hold for the case $H_1 \neq H_0$.

Proposition 5 $L(H,\gamma) \geq C(H_0)$.

Proof: Since $\|H_1\|_\infty < \gamma$, $(I - \gamma^{-2}H_1H_1^*) < 1$ and $(I - \gamma^{-2}H_1H_1^*)^{-1} < 1$. The result then follows directly from the definition of $L(H,\gamma)$ in Equation (1). $\square$

Finally, note that relaxing the $\mathcal{H}_\infty$-norm bound completely recovers the $\mathcal{H}_2$ cost.

Proposition 6 $\lim_{\gamma \to \infty} L(H,\gamma) = C(H_0)$.

Proof: This follows directly from the definition of $L(H,\gamma)$ in Equation (1) and the Dominated Convergence Theorem. $\square$

Evaluation of the Cost

Consider a state space representation for a strictly proper system $H = [H_0 \; H_1]$,

$$H = \left[\begin{array}{c|cc} A & B_0 & B_1 \\ \hline C & 0 & 0 \end{array}\right] = C(sI - A)^{-1} [B_0 \; B_1] \qquad (4)$$

The aim is to evaluate $L(H,\gamma)$ in terms of the state space data. Note that a non-zero term D_1 could be included; H_1 is made strictly proper only to simplify the results.

Lemma 7 *Let* $H = [H_0 \; H_1]$ *be given by Equation (4)*, $\gamma \in \mathbb{R}$, *and* $\|H_1\|_\infty < \gamma$. *Then*

$$L(H,\gamma) = \text{trace}\left\{CQC^T\right\} \qquad (5)$$

where P, Q *satisfy* $(A + \gamma^{-2}B_1B_1^TP)$ *stable and*

$$PA + A^TP + \gamma^{-2}PB_1B_1^TP + C^TC = 0 \qquad (6)$$

$$(A + \gamma^{-2}B_1B_1^TP)Q + Q(A + \gamma^{-2}B_1B_1^TP)^T + B_0B_0^T = 0 \qquad (7)$$

Proof: Since $H_1H_1^* < \gamma^2 I \;\; \forall \omega$, then $\exists M^{\pm 1} \in \mathcal{RH}_\infty$ given by

$$M^*M = H_0^*(I - \gamma^{-2}H_1H_1^*)^{-1}H_0 \qquad (8)$$

A state space representation for M^*M can be found by noting that M^*M is the transfer function of the feedback system shown in Figure 1. So

$$M^*M = \left[\begin{array}{cc|c} A & \gamma^{-2}B_1B_1^T & B_0 \\ -C^TC & -A^T & 0 \\ \hline 0 & B_0^T & 0 \end{array}\right] \qquad (9)$$

With P given by Equation (6), then

$$M = \left[\begin{array}{c|c} A + \gamma^{-2}B_1B_1^TP & B_0 \\ \hline C & 0 \end{array}\right] \qquad (10)$$

is the stable factor of M^*M above [11]. Substituting Equation (8) into (1), it is clear from (3) that the cost $L(H,\gamma)$ is then given by $\|M\|_2$, where $\|M\|_2 = \text{trace}\left\{CQC^T\right\}$ and Q satisfies the Lyapunov equation (7) [13]. $\square$
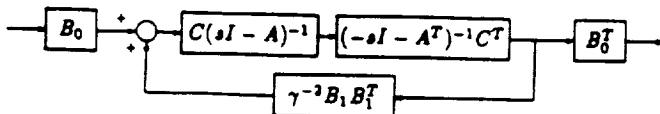

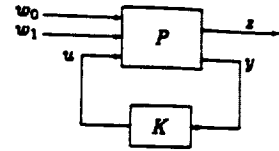Figure 1: Block Diagram for M^*M

Figure 2: Feedback System

Optimization

The goal of this section is to present an approach for solving for the optimum controller that minimizes a cost functional of the form (1). Linear time-invariant controllers will be assumed throughout, but this form is not proven to yield minimal cost. The necessary conditions that an optimal compensator must satisfy are presented. Conditions for the existence of such a controller are not discussed here.

The system can be described by the block diagram in Figure 2. P can be realized in state space as

$$P = \left[\begin{array}{c|ccc} A & B_0 & B_1 & B_2 \\ \hline C_1 & 0 & 0 & D_{12} \\ C_2 & D_{20} & D_{21} & 0 \end{array}\right] \qquad (11)$$

and H is then given by the lower linear fractional transformation,

$$H = \mathcal{F}(P,K) = [P_{10} \; P_{11}] + P_{12}K(I - P_{22}K)^{-1} [P_{20} \; P_{21}] \qquad (12)$$

Admissible compensators K will be those which stabilize P, and satisfy $\|H_1\|_\infty < \gamma$. The problem statement is then

$$\min_K \left\{L(H,\gamma) : K \text{ admissible}\right\} \qquad (13)$$

By a scaling of H, without loss of generality consider the case $\gamma = 1$.

The full state feedback problem is examined first, with normalized control weighting, so that $C_1^T = [C^T \; 0]$ and $D_{12}^T = [0 \; I]$.

Theorem 8 *Consider the problem statement (13), with* $A_{CL} := A + B_2F$. *If* F *is a static feedback matrix that solves Equation (13), then:*

$$F = -B_2^T(P\tilde{Q} + \tilde{P}Q)(Q + \tilde{Q})^{-1} \qquad (14)$$

where P, Q, $\tilde{P}$, *and* $\tilde{Q}$ *satisfy* $A_{tmp} = (A_{CL} + B_1B_1^TP)$ *stable and*

$$PA_{CL} + A_{CL}^TP + PB_1B_1^TP + C^TC + F^TF = 0 \qquad (15)$$

$$A_{tmp}Q + QA_{tmp}^T + B_0B_0^T = 0 \qquad (16)$$

$$\tilde{P}A_{tmp} + A_{tmp}^T\tilde{P} + C^TC + F^TF = 0 \qquad (17)$$

$$A_{tmp}\tilde{Q} + \tilde{Q}A_{tmp}^T + Q\tilde{P}B_1B_1^T + B_1B_1^T\tilde{P}Q = 0 \qquad (18)$$

Proof: The closed loop system is $H = \left[\begin{array}{c|cc} A_{CL} & B_0 & B_1 \\ \hline C & 0 & 0 \\ F & 0 & 0 \end{array}\right]$. From Proposition 7, the cost is $J = \text{trace}\left\{CQC^T + FQF^T\right\}$, where Q solves the Lyapunov equation (16), and P satisfies the Riccati equation (15). Appending these two equations to the cost as constraints with Lagrange multipliers $\tilde{P}$ and $\tilde{Q}$ respectively yields the equations for $\tilde{P}$, $\tilde{Q}$ and F upon differentiating with respect to Q, P and F.

Preliminary results indicate that an iterative approach to solving these equations converges rapidly to the optimal feedback law F. Given an initial guess for F (say, from the minimum entropy control problem [5]), P, Q, $\tilde{P}$, and $\tilde{Q}$ can be computed sequentially as the solution of Riccati and Lyapunov equations. Equation (14) can then be evaluated for F, and the process repeated.

For a system of order n and a fixed order compensator of order n_c, the necessary conditions for the optimum can be found again using a Lagrange multiplier approach, in terms of 4 order $n + n_c$ matrix equations similar to Equations (15)–(18). Work currently in progress to simplify and interpret these results for the dynamic compensation problem. Note that there is no a priori reason to expect that no improvement in the cost can be achieved for $n_c > n$.

Time Domain Interpretation

The form of the augmented cost for the linear control problem leads to an interesting differential games interpretation. It is well known that the central controller in the $\mathcal{H}_\infty$ problem can be found as the solution to a zero-sum differential game [14], where for minimizing $\|T_{zw}\|_\infty$, the control u and noise w solve the optimization problems:

$$u = \mathrm{argmin} \int_0^\infty z^T z - \gamma^2 w^T w \; dt \qquad (19)$$

$$w = \mathrm{argmin} \int_0^\infty -z^T z + \gamma^2 w^T w \; dt \qquad (20)$$

u has some information y about the state, and w has full information.

With the current cost functional, and under the assumption of linear feedback, the optimization problem is again equivalent to a differential game, but it is no longer a zero-sum game. Whether the two problems are equivalent when both are allowed nonlinear feedback is unknown.

Proposition 9 *If an optimal linear compensator exists for problem (13), then it is the same as that of a Stackelberg differential game with u as leader, w_1 as follower and w_0 as unit intensity white noise, where u and w_1 solve the following optimization problems:*

$$u = \mathrm{argmin} \lim_{t \to \infty} E\left\{ z^T z \right\} \qquad (21)$$

$$w_1 = \mathrm{argmin} \lim_{t \to \infty} E\left\{ -z^T z + \gamma^2 w_1^T w_1 \right\} \qquad (22)$$

u has some information y about the state, and w has full information.

Proof: Assuming a linear control law for u, the optimization problem for w_1 is easily solved with a single Riccati equation (which is Equation (15) for the state feedback case.) Appending this as a constraint for the optimization problem (21) results in an identical problem formulation to that of problem (13). $\square$

This game seems to be a more natural problem to pose than the pure $\mathcal{H}_\infty$ differential game, since the control does not benefit from the use of noise, but instead optimizes an $\mathcal{H}_2$ type of cost functional, while the deterministic noise w_1 solves the same optimization problem as before. In addition, the plant is subject to a white noise input w_0. This looks similar to the framework of [6,7] since a single output is minimized in the presence of two disturbance inputs, one of which is associated with the $\mathcal{H}_2$ nature of the problem while the other is associated with the $\mathcal{H}_\infty$ nature.

Note that for a non-zero sum differential game, the solution depends on how the optimality is defined. For the Stackelberg or leader-follower solution [15–17], one player (here the control u) acts as leader and announces a strategy, and knowing this strategy, the follower (here the noise w_1) solves its optimization problem. Also note that in general, the optimal control for the Stackelberg problem is known to be nonlinear [17]. Similar equations to (15)–(18) have been reported in [16], where the optimal linear state feedback law for a Stackelberg problem was found. The nonlinear, team optimal strategy obtained, for example, in [17] does not apply to this problem since the leader u cannot increase the follower w_1's cost indefinitely, and therefore cannot induce w_1 to follow a strategy desirable to u.

The differential games representation of problem (13) allows the matrices of Equations (15)–(18) to be given an interpretation. $-P$ and $+\tilde{P}$ correspond to the optimal cost-to-go for the costs associated with w_1 and u respectively, Q is the covariance of the state, and $\tilde{Q}$ is the sensitivity of the cost for u to changes in the cost for w_1.

References

[1] Bernstein, D. S. and Haddad, W. M., "LQG Control with an $\mathcal{H}_\infty$ Performance Bound: A Riccati Equation Approach," *IEEE Trans. Auto. Control*, Vol. 34, No 3, March 1989, pp. 293-305.

[2] Haddad, W. M. and Bernstein, D. S., "On the Gap Between $\mathcal{H}_2$ and Entropy Performance Measures in $\mathcal{H}_\infty$ Control Design," *Proceedings, 28th IEEE Conf. on Decision and Control*, Dec. 1989, pp. 1506-1508.

[3] Rotea, M. A., and Khargonekar, P. P., "Simultaneous $\mathcal{H}_2/\mathcal{H}_\infty$ Optimal Control with State Feedback," *Proceedings, 1990 Am. Control Conference*, San Diego, CA, May 1990, pp. 2380-2384.

[4] Mustafa, D. "Relations Between Maximum-entropy/$\mathcal{H}_\infty$ Control and Combined $\mathcal{H}_\infty$/LQG Control," *Systems and Control Letters*, Vol. 12, 1989, pp. 193-203.

[5] Mustafa, D. *Minimum Entropy $\mathcal{H}_\infty$ Control*, PhD Thesis, University of Cambridge, 1989.

[6] Doyle, J., Zhou, K., and Bodenheimer, B., "Optimal Control with Mixed $\mathcal{H}_2$ and $\mathcal{H}_\infty$ Performance Objectives," *Proceedings, 1989 Am. Control Conference*, Pittsburgh, PA, pp. 2065-2070.

[7] Zhou, K., Doyle, J., Glover and Bodenheimer, B., "Mixed $\mathcal{H}_2$ and $\mathcal{H}_\infty$ Control," *Proceedings, 1990 Am. Control Conference*, San Diego, CA, May 1990, pp. 2502-2507.

[8] Miller, D. W., Hall, S. R. and von Flotow, A. H., "Optimal Control of Power Flow at Structural Junctions," *J. of Sound and Vibration*, Vol. 140, No. 2, 1990.

[9] MacMartin, D. G. and Hall, S. R., "An $\mathcal{H}_\infty$ Power Flow Approach to Control of Uncertain Structures," *Proceedings, 1990 Am. Control Conference*, San Diego, CA, May 1990, pp. 3073-3080, to appear in *AIAA J. of Guidance, Control, and Dynamics*.

[10] MacMartin, D. G. and Hall, S. R., "Applications of Statistical Energy Analysis to Control," *preprint*, June, 1990.

[11] Francis, B. A., *A Course in $\mathcal{H}_\infty$ Control Theory*, Springer-Verlag, 1987.

[12] Kwakernaak, and Sivan, *Linear Optimal Control Systems*, Wiley-Interscience, 1972.

[13] Doyle, J. C., Glover, K., Khargonekar, P. P., and Francis, B. A., "State-Space Solutions to Standard $\mathcal{H}_2$ and $\mathcal{H}_\infty$ Control Problems," *IEEE Trans. Auto. Control*, Vol. 34, No. 8, Aug. 1989, pp. 831-847.

[14] Rhee, I., and Speyer, J. L., "A Game Theoretic Controller and its Relationship to $\mathcal{H}_\infty$ and Linear-Exponential-Gaussian Synthesis," *Proceedings, 28th IEEE Conf. on Decision and Control*, Dec. 1989, pp. 909-915.

[15] Simaan, M., and Cruz, J. B., "On the Stackelberg Strategy in Nonzero-Sum Games," *J. Opt. Theory and Applications*, Vol. 11, No. 5, 1973, pp. 533-555.

[16] Medanic, J., "Closed-loop Stackelberg Strategies in Linear-Quadratic Problems," *IEEE Trans. Auto. Contr.*, Vol. AC-23, No. 4, Aug. 1978, pp. 632-637.

[17] Basar, T., and Selbuz, H., "Closed-Loop Stackelberg Strategies with Applications in the Optimal Control of Multilevel Systems," *IEEE Trans. Auto. Contr.*, Vol. AC-24, No. 2, April 1979, pp. 166-179.

Fixed-Order Multi-Model Estimation and Control

Douglas MacMartin and Steven R. Hall*

Dept. of Aeronautics and Astronautics

Massachusetts Institute of Technology

Cambridge, MA 02139

(617) 258-8747

Dennis S. Bernstein[t]

Harris Corporation

MS 22/4842

Melbourne, FL 32901

(407) 729-2140

September 17, 1990

Submitted to the 1991 American Control Conference

Abstract

In certain applications modeling uncertainty can be represented by a finite number of plant models. This paper considers the problems of determining a feedback controller or estimator that optimizes an $\mathcal{H}_2$ performance criterion involving a collection of plant models. The approach is based upon fixed-structure optimization in which the estimator or controller order are fixed prior to the development of optimality conditions.

1 Introduction

The goal of robust control design is to obtain controllers that maintain desirable performance in the face of modeling uncertainty. In certain cases modeling uncertainty can be adequately represented by means of a finite number of plant models. This multi-model problem arises for example, if the plant can undergo sensor or actuator failure modes. A finite set of models has also been used to design for robustness to an infinite set of models, as in the case of parametric uncertainty [1], high frequency uncertainty [2], or parameter variations (e.g. for different flight regimes) [3].

A fundamental issue in multi-model problems is the *simultaneous* or *reliable* stabilization problem. Here the goal is to design controllers that stabilize each model in a finite collection of plant models. Considerable progress has been made in solving this problem [4–10].

The goal of the present paper is to consider a multi-model optimization problem. Specifically, we consider a quadratic ($\mathcal{H}_2$) performance criterion involving a collection of plant models controlled by a single feedback compensator. The approach we take involves fixing the order of the compensator and optimizing over the feedback gains. This approach is similar to that of [11] where static output feedback controllers were considered.

One of our principal objectives in considering the Multi-Model Control Problem is to examine the issue of compensator order. In [6] it is shown that simultaneous

1

stabilization of a pair of plants of bounded degree may require a compensator of arbitrarily high order. In the present paper we show how this issue manifests itself in the structure of the necessary conditions for optimality.

To further elucidate the role of compensator order we also consider two related problems that are simpler in structure but that involve analogous issues. The objective of the Multi-Model Approximation Problem is to determine a single model that simultaneously approximates a finite collection of models. For a collection of r models each of order n_i, $i = 1, \ldots, r$, the maximal-order solution is given by a model of order $\sum_{i=1}^{r} n_i$, which is larger than the order of each of the given plant models.

In a related vein we also consider the Multi-Model Estimation Problem wherein we seek an estimator for each model in a given collection of plant models. As in the Multi-Model Approximation Problem the maximal-order solution has order greater than the individual plant models.

The fixed-structure approach applied to the multi-model problems is a direct extension of the technique utilized in [12–14]. Indeed, by specializing these results to the case of a single model, the results of [12–14] are immediately recovered.

2 Multi-Model Approximation

Consider the following problem.

Problem 1 (Optimal Multi-Model Approximation Problem) *Given a set of r controllable and observable systems H_i, $i = 1 \ldots r$, with state space representations*

$$H_i = \left[\begin{array}{c|c} A_i & B_i \\ \hline C_i & 0 \end{array} \right] = C_i (sI - A_i)^{-1} B_i \tag{1}$$

and a set of r numbers $\alpha_i \in \mathbb{R}$, $\alpha_i > 0$, $i = 1 \ldots r$, find a single approximation model of fixed order n_m, with state space representation

$$H_m = \left[\begin{array}{c|c} A_m & B_m \\ \hline C_m & 0 \end{array} \right] \tag{2}$$

that minimizes the weighted $\mathcal{H}_2$ model-approximation criterion,

$$J(H_m) = \sum_{i=1}^{r} \alpha_i \| H_i - H_m \|_2^2 \qquad (3)$$

To guarantee finite cost J, assume that each H_i is stable, and also restrict the optimization to the set of stable approximation models H_m. Furthermore, since the value of J is independent of the internal realization of H_m, assume that the realization in Equation (2) is controllable and observable. Thus require that $(A_m, B_m, C_m) \in \mathcal{R}$ where

$$\mathcal{R} = \{(A_m, B_m, C_m) : A_m \text{ stable}, (A_m, B_m) \text{ controllable}, (A_m, C_m) \text{ observable}\}$$

Without loss of generality, the weightings α_i can be assumed to be normalized so that

$$\sum_{i=1}^{r} \alpha_i = 1$$

With this normalization, the weighting α_i can then be associated with the probability that H_i accurately models the dynamics of the system.

The necessary conditions for an optimal solution to this problem are given in Theorem 4. The approach used to obtain them is presented briefly here for comparison with the approach required for the multi-model estimation and control problems in Sections 3 and 4, and for the single model problems in [12–14].

The model approximation error transfer function $H_i - H_m$ can be represented in state space as

$$H_i - H_m = \left[\begin{array}{cc|c} A_i & 0 & B_i \\ 0 & A_m & B_m \\ \hline C_i & -C_m & 0 \end{array} \right] = \left[\begin{array}{c|c} \tilde{A}_i & \tilde{B}_i \\ \hline \tilde{C}_i & 0 \end{array} \right] \qquad (4)$$

The cost J is then

$$J(H_m) = \sum_{i=1}^{r} \operatorname{tr}\left\{ \alpha_i \tilde{C}_i \tilde{Q}_i \tilde{C}_i^{T} \right\} \qquad (5)$$

where each $\tilde{Q}_i$ satisfies a Lyapunov equation

$$\tilde{A}_i \tilde{Q}_i + \tilde{Q}_i \tilde{A}_i^T + \tilde{B}_i \tilde{B}_i^T = 0 \qquad (6)$$

Appending these constraints to the cost with Lagrange multipliers $\tilde{P}_i$ yields first order necessary conditions for a solution upon differentiation with respect to $\tilde{Q}_i$, A_m, B_m, and C_m. Each matrix $\tilde{P}_i$ and $\tilde{Q}_i$ has dimension $(n_i + n_m) \times (n_i + n_m)$ and can be partitioned into $n_i \times n_i$, $n_i \times n_m$, $n_m \times n_i$ and $n_m \times n_m$ blocks as

$$\tilde{P}_i = \begin{bmatrix} \tilde{P}_{i_{11}} & \tilde{P}_{i_{12}} \\ \tilde{P}_{i_{21}} & \tilde{P}_{i_{22}} \end{bmatrix} \qquad \tilde{Q}_i = \begin{bmatrix} \tilde{Q}_{i_{11}} & \tilde{Q}_{i_{12}} \\ \tilde{Q}_{i_{21}} & \tilde{Q}_{i_{22}} \end{bmatrix} \tag{7}$$

The necessary conditions are then Equations (6), and

$$\frac{\partial J}{\partial \tilde{Q}_i} = \tilde{P}_i \tilde{A}_i + \tilde{A}_i^T \tilde{P}_i + \tilde{C}_i^T \tilde{C}_i = 0 \quad \forall i \tag{8}$$

$$\frac{\partial J}{\partial B_m} = \sum_{i=1}^{r} \alpha_i \tilde{P}_{i_{22}} B_m + \sum_{i=1}^{r} \alpha_i \tilde{P}_{i_{12}} B_i = 0 \tag{9}$$

$$\frac{\partial J}{\partial C_m} = C_m \sum_{i=1}^{r} \alpha_i \tilde{Q}_{i_{22}} - \sum_{i=1}^{r} \alpha_i C_i \tilde{Q}_{i_{12}} = 0 \tag{10}$$

$$\frac{\partial J}{\partial A_m} = \sum_{i=1}^{r} \alpha_i (\tilde{P}_{i_{22}} \tilde{Q}_{i_{22}} + \tilde{P}_{i_{21}} \tilde{Q}_{i_{12}}) = 0 \tag{11}$$

The equation obtained from differentiation with respect to A_m is of particular importance in simplifying and understanding the structure of the necessary conditions. In the case of a single model ($r = 1$), Equation (11) yields

$$I_{n_m} = \underbrace{(-\tilde{P}_{22}^{-1} \tilde{P}_{21})}_{\Gamma} \underbrace{(\tilde{Q}_{12} \tilde{Q}_{22}^{-1})}_{G^T} \tag{12}$$

A projection operator $\tau = G^T \Gamma = \tau^2$ is then used to simplify the equations [12].

For the multi-model approximation case, from Equation (6) each $\tilde{Q}_{i_{22}}$ satisfies an identical equation,

$$A_m \tilde{Q}_{i_{22}} + \tilde{Q}_{i_{22}} A_m^T + B_m B_m^T = 0 \tag{13}$$

Hence the $\tilde{Q}_{i_{22}}$ satisfy $\tilde{Q}_{i_{22}} = \tilde{Q}_{22}$, $i = 1 \ldots r$. Similarly, each $\tilde{P}_{i_{22}}$ satisfies

$$\tilde{P}_{i_{22}} A_m + A_m^T \tilde{P}_{i_{22}} + C_m^T C_m = 0 \tag{14}$$

4

and hence $\tilde{P}_{i_{22}} = \tilde{P}_{22}$, $i = 1 \ldots r$. Furthermore, from Equations (13) and (14), $\tilde{Q}_{22}$ and $\tilde{P}_{22}$ are the controllability and observability grammians, respectively, of the system H_m. With these simplifications Equation (11) can be written as

$$\tilde{P}_{22}\tilde{Q}_{22} + \sum_{i=1}^{r} \alpha_i (\tilde{P}_{i_{21}} \tilde{Q}_{i_{12}}) = 0 \qquad (15)$$

This immediately gives the following result:

Proposition 2 *Given a fixed order model that is optimal for Problem 1, of order $n_m > N = \sum_{i=1}^{r} n_i$, there exists a model of order N with the same cost. Hence with no fixed order constraint, the optimal system for multi-model approximation has order no larger than N.*

Proof: $\forall i$, $\text{rank}\left\{\tilde{P}_{i_{21}}\tilde{Q}_{i_{12}}\right\} \leq n_i$, hence $\text{rank}\left\{\sum_{i=1}^{r} \alpha_i \tilde{P}_{i_{21}} \tilde{Q}_{i_{12}}\right\} \leq N$. So, from Equation (15), $\text{rank}\left\{\tilde{P}_{22}\tilde{Q}_{22}\right\} \leq N$. If $n_m > N$, either $\tilde{P}_{22}$ or $\tilde{Q}_{22}$ or both must not be full rank, and thus the representation of H_m must have states which are either uncontrollable or unobservable. (The maximum number of states which are both observable and controllable is N.) Removing any uncontrollable or unobservable states yields a system with identical cost and at most N states. □

With the controllability and observability assumptions on the representation of H_m, $\tilde{P}_{22}$ and $\tilde{Q}_{22}$ must be positive definite, and thus Equation (15) can be written

$$I_{n_m} = \sum_{i=1}^{r} \underbrace{(-\alpha_i \tilde{P}_{22}^{-1} \tilde{P}_{i_{21}})}_{\Gamma_i} \underbrace{(\tilde{Q}_{i_{12}} \tilde{Q}_{22}^{-1})}_{G_i^T} \qquad (16)$$

Define

$$\Gamma = \begin{bmatrix} \Gamma_1 & \cdots & \Gamma_r \end{bmatrix} \qquad (17)$$

$$G = \begin{bmatrix} G_1 & \cdots & G_r \end{bmatrix} \qquad (18)$$

$$\tau = G^T \Gamma \qquad (19)$$

$$\tau_{\perp} = I_N - \tau \qquad (20)$$

5

Then τ is again an oblique projection operator, that is $\tau^2 = \tau$. Note that in general, τ is oblique rather than orthogonal, since it need not be symmetric.

The following lemma from [12] is required for the statement of the main theorem.

Lemma 3 *Suppose $\hat{Q}$, $\hat{P} \in \mathbb{R}^{N \times N}$ are positive semi-definite. Then $\hat{Q}\hat{P}$ is nonnegative semisimple (has non-negative eigenvalues). Furthermore, if* $\mathrm{rank}\{\hat{Q}\hat{P}\} = n_m$, *then there exist $G, \Gamma \in \mathbb{R}^{n_m \times N}$ and positive semisimple $M \in \mathbb{R}^{n_m \times n_m}$ such that*

$$\hat{Q}\hat{P} = G^T M \Gamma \tag{21}$$

$$\Gamma G^T = I_{n_m} \tag{22}$$

Matrices G, Γ, and M satisfying the conditions of the lemma will be referred to as a projective factorization of $\hat{Q}\hat{P}$.

It will be convenient to compile the state space information about all of the models into a single set of matrices $(\hat{A}, \hat{B}, \hat{C}_\alpha)$, where

$$\hat{A} = \begin{bmatrix} A_1 & 0 & \cdots & 0 \\ 0 & A_2 & & \\ \vdots & & \ddots & \\ 0 & & & A_r \end{bmatrix} \qquad \hat{B} = \begin{bmatrix} B_1 \\ B_2 \\ \vdots \\ B_r \end{bmatrix} \tag{23}$$

$$\hat{C}_\alpha = \begin{bmatrix} \alpha_1 C_1 & \alpha_2 C_2 & \cdots & \alpha_r C_r \end{bmatrix}$$

The subscript α on $\hat{C}_\alpha$ indicates that it depends on α_i.

Theorem 4 *Suppose (A_m, B_m, C_m) solves the optimal multi-model approximation problem (1). Then there exist positive semi-definite matrices $\hat{Q}$, $\hat{P} \in \mathbb{R}^{N \times N}$ such that, for some projective factorization of $\hat{Q}\hat{P}$, A_m, B_m, and C_m are given by*

$$A_m = \Gamma \hat{A} G^T \tag{24}$$

$$B_m = \Gamma \hat{B} \tag{25}$$

$$C_m = \hat{C}_\alpha G^T \tag{26}$$

6

and such that the following conditions are satisfied:

$$\text{rank}\left\{\hat{Q}\right\} = \text{rank}\left\{\hat{P}\right\} = \text{rank}\left\{\hat{Q}\hat{P}\right\} = n_m \qquad (27)$$

$$\hat{A}\hat{Q} + \hat{Q}\hat{A}^T + \hat{B}\hat{B}^T - \tau_\perp\hat{B}\hat{B}^T\tau_\perp^T = 0 \qquad (28)$$

$$\hat{P}\hat{A} + \hat{A}^T\hat{P} + \hat{C}^T\hat{C} - \tau_\perp^T\hat{C}_\alpha^T\hat{C}_\alpha\tau_\perp = 0 \qquad (29)$$

Proof: Define $\hat{Q} = G^T\tilde{Q}_{22}G$ and $\hat{P} = \Gamma^T\tilde{P}_{22}\Gamma$, and note that $\tau\hat{Q} = \hat{Q}$, and $\hat{P}\tau = \hat{P}$. Pre- and post-multiplying the Lyapunov equations (13) and (14) for $\tilde{Q}_{22}$ and $\tilde{P}_{22}$ by either $I_{n_m} = \Gamma G^T$ or $I_{n_m} = G\Gamma^T$ yields the following equations:

$$\tau\left[\hat{A}\hat{Q} + \hat{Q}\hat{A}^T + \hat{B}\hat{B}^T\right] = 0 \qquad (30)$$

$$\left[\hat{P}\hat{A} + \hat{A}^T\hat{P} + \hat{C}_\alpha^T\hat{C}_\alpha\right]\tau = 0 \qquad (31)$$

The $(1,2)$ sub-blocks of the Lyapunov equations (6) and (8) yield identical equations. Equation (30) is equivalent to Equation (28) since Equation $(28)=(30)+(30)^T-(30)\tau$, and Equation $(30)=\tau(28)$. Similarly, Equations (31) and (29) are equivalent. Note that only two Lyapunov equations are required for the necessary conditions because the $(1,1)$ sub-blocks of both Equation (6) and Equation (8) are superfluous.

Equations (25) and (26) follow directly from (9) and (10). Equation (24) for A_m is obtained from the $(2,2)$ block of either $\left(\sum_{i=1}^r \alpha_i(\text{Eq'n 8})\tilde{Q}_i\right)$ or $\left(\sum_{i=1}^r \alpha_i\tilde{P}_i(\text{Eq'n 6})\right)$, either of which yield that $\sum_{i=1}^r \left(\alpha_i\tilde{P}_i\tilde{A}_i\tilde{Q}_i\right)_{22} = 0$. $\qquad\square$

Because the form of the equations is identical to that of the single model case, the discussion in [12] applies for this problem as well. As in [12], the form is a result of optimality, and not fixed beforehand. If (A_m, B_m, C_m) satisfies the necessary conditions, so does $(TA_mT^{-1}, TB_m, C_mT^{-1})$ for an arbitrary nonsingular transformation matrix T. Further, there exists a similarity transformation which diagonalizes $\hat{Q}\hat{P}$ and τ simultaneously. Representing τ in terms of $\hat{Q}\hat{P}$ as in [12] leads to numerical algorithms for the optimal multi-model approximation problem.

Remark 5 *In the "full order" case $n_m = N$, then $\tau = G = \Gamma = I_N$, giving $A_m = \hat{A}$, $B_m = \hat{B}$, and $C_m = \hat{C}_\alpha$. Thus $H_m = \sum_{i=1}^{r} \alpha_i H_i$. This is exactly the expected result; the best possible approximation is simply the weighted average of all the models.*

Remark 6 *For a single model ($r = 1$), the equations clearly collapse to the equations of [12].*

3 Multi-Model Estimation

Consider the following problem.

Problem 7 (Optimal Multi-Model Estimation Problem) *Given a set of r systems H_i, $i = 1 \ldots r$, with state space representations*

$$H_i = \left[\begin{array}{c|c} A_i & \bar{B}_i \\ \hline C_{i_1} & 0 \\ C_{i_2} & \bar{D}_i \end{array}\right] = \left[\begin{array}{c} C_{i_1} \\ C_{i_2} \end{array}\right] (sI - A_i)^{-1} \bar{B}_i + \left[\begin{array}{c} 0 \\ \bar{D}_i \end{array}\right] \tag{32}$$

and a set of r numbers $\alpha_i \in \mathbb{R}$, $\alpha_i > 0$, $i = 1 \ldots r$, find a single estimator of fixed order n_e, with state space representation

$$H_e = \left[\begin{array}{c|c} A_e & B_e \\ \hline C_e & 0 \end{array}\right] \tag{33}$$

that minimizes the weighted $\mathcal{H}_2$ model-estimation criterion,

$$J(H_e) = \sum_{i=1}^{r} \alpha_i \left\| H_{i_1} - H_e H_{i_2} \right\|_2^2 \tag{34}$$

where H_i is partitioned into H_{i_1} and H_{i_2} according to the two outputs.

The estimation problem can be illustrated by the block diagram as shown in Figure 1.
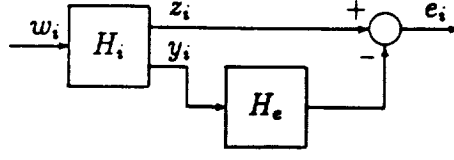
The following assumptions about the problem will be made:

8

Figure 1: Estimation problem for each system.

(i) Each H_i is stable, and each (A_i, C_{i_2}) is detectable.

(ii) $\sum\limits_{i=1}^{r} \alpha_i = 1$

(iii) For clarity in understanding the form of the equations, the process and measurement noise for each model will be assumed to be uncorrelated, so $\bar{B}_i \bar{D}_i^T = 0$. Without loss of generality, assume $\bar{B}_i = [B_i \ 0]$ and $\bar{D}_i = [0 \ D_i]$.

(iv) Require that the measurement noise have no singular directions common to all models, so $\sum\limits_{i=1}^{r} \alpha_i D_i D_i^T > 0$. This is a generalization of the usual single model assumption of nonsingular measurement noise, $DD^T > 0$.

It is interesting to note that each D_i need not have full row rank, hence the estimation problem for each individual model may be singular without the multi-model problem being singular.

As in the multi-model approximation case, require $(A_e, B_e, C_e) \in \mathcal{R}$.

The model estimation error transfer function $H_{i_1} - H_e H_{i_2}$ can be represented in state space as

$$H_{i_1} - H_e H_{i_2} = \left[\begin{array}{cc|cc} A_i & 0 & B_i & 0 \\ B_e C_{i_2} & A_e & 0 & B_e D_i \\ \hline C_{i_1} & -C_e & 0 & 0 \end{array} \right] = \left[\begin{array}{c|c} \tilde{A}_i & \tilde{B}_i \\ \hline \tilde{C}_i & 0 \end{array} \right] \qquad (35)$$

The cost J can again be written in the form of Equation (5),

$$J(H_e) = \sum\limits_{i=1}^{r} \mathrm{tr}\left\{ \alpha_i \tilde{C}_i \tilde{Q}_i \tilde{C}_i^T \right\} \qquad (36)$$

9

where each $\bar{Q}_i$ satisfies a Lyapunov equation identical to Equation (6)).

Necessary conditions can again be obtained using a Lagrange multiplier approach. The Lyapunov equations for $\tilde{P}_i$ are identical to Equations (8). The equation obtained by differentiating with respect to A_e is the same as Equation (11), and once again this will be the key equation for understanding the structure of the necessary conditions. For this problem, each $\tilde{Q}_{i_{22}}$ satisfies

$$A_e \tilde{Q}_{i_{22}} + \tilde{Q}_{i_{22}} A_e^T + B_e C_{i_2} \tilde{Q}_{i_{12}} + \tilde{Q}_{i_{21}} C_{i_2}^T B_e^T + B_e B_e^T = 0 \qquad (37)$$

Each $\tilde{Q}_{i_{22}}$ now satisfies a distinct equation, and thus $\tilde{Q}_{i_{22}} \neq \tilde{Q}_{j_{22}}$, $i \neq j$. The critical observation for this problem, however, is that each $\tilde{P}_{i_{22}}$ still satisfies Equation (14). Thus it is still true that $\tilde{P}_{i_{22}} = \tilde{P}_{22}$, $i = 1 \ldots r$. This is sufficient to obtain the elements of a projection operator from Equation (11), and to prove the following result, analogous to Proposition 2.

Proposition 8 *Given a fixed order model that is optimal for Problem 7, of order $n_m > N = \sum\limits_{i=1}^{r} n_i$, there exists a model of order N with the same cost. Hence with no fixed order constraint, the optimal system for multi-model estimation has order no larger than N.*

Proof: As in the Multi-Model Approximation case, $\text{rank}\left\{ \sum\limits_{i=1}^{r} \alpha_i \tilde{P}_{i_{21}} \tilde{Q}_{i_{12}} \right\} \leq N$. From Equation (11), $\text{rank}\left\{ \tilde{P}_{22} \sum\limits_{i=1}^{r} \alpha_i \tilde{Q}_{i_{22}} \right\} \leq N$. If $n_m > N$, either $\tilde{P}_{22}$ or $\sum\limits_{i=1}^{r} \alpha_i \tilde{Q}_{i_{22}}$ or both must not be full rank. $\tilde{P}_{22}$ is the observability grammian of the system (A_e, B_e, C_e), and thus is not full rank if and only if (A_e, C_e) is unobservable. Also, $\sum\limits_{i=1}^{r} \alpha_i \tilde{Q}_{i_{22}}$ is not full rank if and only if (A_e, B_e) is not controllable. This result will be proven in Proposition 13. Proposition 8 then follows in the same manner as the proof of Proposition 2. $\qquad \square$

Remark 9 *The estimator must obtain all the information possible about the state from the output y. Since all state information from all the models has a finite dimension N, there is an estimator state vector of dimension N that contains the most*

10

information possible about the state vectors of the H_i. Any additional estimator states must be redundant.

As noted earlier, $\bar{P}_{22}$ is the observability grammian for H_e and therefore must be positive definite. Proposition 13 proves that $\sum_{i=1}^{r} \alpha_i \bar{Q}_{i_{22}}$ must also be positive definite. Hence for the multi-model estimation problem, Equation (11) can be written as

$$I_{n_{\mathbb{P}}} = \sum_{i=1}^{r} \underbrace{(-\alpha_i \bar{P}_{22}^{-1} \bar{P}_{i_{21}})}_{\Gamma_i} \underbrace{(\bar{Q}_{i_{12}} \left(\sum_{i=1}^{r} \alpha_i \bar{Q}_{i_{22}} \right)^{-1})}_{G_i^T} \tag{38}$$

With G, Γ, and τ defined as in Equations (17–19), τ is again a projection operator, satisfying $\tau^2 = \tau$.

In addition to the definitions of $\hat{A}$ and $\hat{B}$, given in Equation (23), this problem requires $\hat{C}_{\alpha_1}$ and $\hat{C}_{\alpha_2}$, defined analogously to $\hat{C}_\alpha$, and

$$\hat{V}_1 = \begin{bmatrix} B_1 B_1^T & 0 & \cdots & 0 \\ 0 & B_2 B_2^T & & \\ \vdots & & \ddots & \\ 0 & & & B_r B_r^T \end{bmatrix} \tag{39}$$

$$V_2 = \sum_{i=1}^{r} \alpha_i D_i D_i^T \tag{40}$$

Theorem 10 *Suppose* (A_e, B_e, C_e) *solves the optimal multi-model estimation problem (7). Then there exist positive semi-definite matrices* Q, $\hat{Q}$, $\hat{P} \in \mathbb{R}^{N \times N}$ *such that, for some projective factorization of* $\hat{Q}\hat{P}$, A_e, B_e, *and* C_e *are given by*

$$A_e = \Gamma \hat{A} G^T - B_e \hat{C}_{\alpha_2} G^T \tag{41}$$

$$B_e = \Gamma Q \hat{C}_{\alpha_2}^T V_2^{-1} \tag{42}$$

$$C_e = \hat{C}_{\alpha_1} G^T \tag{43}$$

and such that the following conditions are satisfied:

$$\hat{A}Q + Q\hat{A}^T + \hat{V}_1 - Q\hat{C}_{\alpha_2}^T V_2^{-1} \hat{C}_{\alpha_2} Q + \tau_\perp Q \hat{C}_{\alpha_2}^T V_2^{-1} \hat{C}_{\alpha_2} Q \tau_\perp = 0 \tag{44}$$

11

$$\hat{A}\hat{Q} + \hat{Q}\hat{A}^T + Q\hat{C}_{\alpha_2}^T V_2^{-1}\hat{C}_{\alpha_2}Q - \tau_{\perp}Q\hat{C}_{\alpha_2}^T V_2^{-1}\hat{C}_{\alpha_2}Q\tau_{\perp} = 0 \tag{45}$$

$$\hat{P}(\hat{A} - Q\hat{C}_{\alpha_2}^T V_2^{-1}\hat{C}_{\alpha_2}) + (\hat{A} - Q\hat{C}_{\alpha_2}^T V_2^{-1}\hat{C}_{\alpha_2})^T\hat{P} + \hat{C}_{\alpha_1}^T\hat{C}_{\alpha_1} - \tau_{\perp}\hat{C}_{\alpha_1}^T\hat{C}_{\alpha_1}\tau_{\perp} = 0 \tag{46}$$

Proof: The derivation of these equations is similar to that for the necessary conditions for the multi-model approximation problem. Define $\hat{Q} = G^T\left(\sum_{i=1}^{r}\alpha_i\tilde{Q}_{i_{22}}\right)G$, $\hat{P} = \Gamma^T\tilde{P}_{22}\Gamma$, and $Q = \text{diag}\left\{\alpha_i^{-1}\tilde{Q}_{i_{11}}\right\} - \hat{Q}$. Substituting into the Lyapunov equations defining $\tilde{Q}_i$ and $\tilde{P}_i$ yields Equations (45) and (46) from both the $(1,2)$ and $(2,2)$ sub-blocks. The $(1,1)$ sub-block of the $\tilde{Q}_i$ Lyapunov equation can be used to obtain Equation (44), and the $(1,1)$ sub-block of the $\tilde{P}_i$ equation is superfluous. Equations (42) and (43) follow directly from the equations obtained by differentiating the augmented cost with respect to B_e and C_e. Equation (41) for A_e is obtained in an analogous fashion to the approximation problem. $\square$

As in the multi-model approximation case, the necessary conditions obtained here are similar in form to those for the single model case [13]. Again, the necessary conditions hold for any non-singular state transformation of the estimator. Numerical algorithms developed for solving the equations in [13] can be applied to this problem as well.

Remark 11 *In the "full order" case $n_e = N$, then $\tau = G = \Gamma = I_N$, giving $A_e = \hat{A} - B_e\hat{C}_{\alpha_2}$, $B_e = Q\hat{C}_{\alpha_2}^T V_2^{-1}$, and $C_e = \hat{C}_{\alpha_1}$. Only the Riccati equation for Q needs to be solved, and this has the same form as the Kalman filter equation. Because of the coupling of the multiple models in Q, the full order estimator is not simply a weighted average of the individual model estimators.*

Remark 12 *For a single model ($r = 1$), the equations clearly collapse to the equations of [12]. For $r = 1$ and $n_e = N$, the equations collapse to the standard Kalman filter result.*

Finally, the proposition used in the proof of Proposition 8 needs to be proven.

Proposition 13 $\bar{Q} = \sum_{i=1}^{r}\alpha_i\tilde{Q}_{i_{22}}$ *is full rank if and only if (A_e, B_e) is controllable.*

Proof: $\bar{Q}$ satisfies the Lyapunov equation

$$(A_e + B_e \hat{C}_{\alpha_2} G^T) \bar{Q} + \bar{Q}(A_e + B_e \hat{C}_{\alpha_2} G^T)^T + B_e V_2 B_e^T = 0 \qquad (47)$$

This follows from summing Equations (37) and representing $\bar{Q}_{i_{12}}$ in terms of G and $\bar{Q}$. $\bar{Q}$ is therefore a controllability grammian, and is full rank if and only if $(A_e + B_e \hat{C}_{\alpha_2} G^T, B_e)$ is controllable. This system is controllable if and only if (A_e, B_e) is controllable. □

4 Multi-Model Control

A simple form of the necessary conditions for the multi-model control problem is significantly harder to obtain than for either of the two previously considered problems. A form of the equations similar to the single model case has not yet been obtained. The problem will be set up here, and the critical issues discussed. In particular, the question of controller order is investigated.

Consider the following problem.

Problem 14 (Optimal Multi-Model Control Problem) *Given a set of r systems H_i, $i = 1 \ldots r$, with state space representations*

$$H_i = \left[\begin{array}{c|cc} A_i & \bar{B}_{i_1} & B_{i_2} \\ \hline \bar{C}_{i_1} & 0 & \bar{D}_{i_{12}} \\ C_{i_2} & \bar{D}_{i_{21}} & 0 \end{array} \right] \qquad (48)$$

and a set of r numbers $\alpha_i \in \mathbb{R}$, $\alpha_i > 0$, $i = 1 \ldots r$, find a single compensator of fixed order n_c, with state space representation

$$H_c = \left[\begin{array}{c|c} A_c & B_c \\ \hline C_c & 0 \end{array} \right] \qquad (49)$$

that minimizes the weighted $\mathcal{H}_2$ model-control criterion,

$$J(H_c) \;\; = \;\; \sum_{i=1}^{r} \alpha_i \, \|H_{i_{zw}}\|_2^2 \qquad (50)$$

$$= \sum_{i=1}^{r} \alpha_i \left\| H_{i_{11}} + H_{i_{12}} H_c (I - H_{i_{22}} H_c)^{-1} H_{i_{21}} \right\|_2^2 \qquad (51)$$

H_i is partitioned into $H_{i_{11}}$, $H_{i_{12}}$, $H_{i_{21}}$ and $H_{i_{22}}$ according to the two inputs and two outputs. The closed loop transfer function $H_{i_{zw}}$ is obtained from the lower linear fractional transformation, $H_{i_{zw}} = \mathcal{F}(H_i, H_c)$.

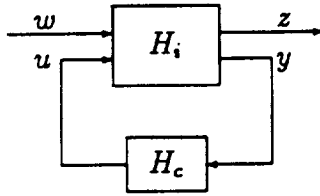The control problem can be illustrated by the block diagram as shown in Figure 2.

Figure 2: Control problem for each system.

The following assumptions about the problem will be made.

(i) Each system H_i must satisfy (A_i, B_{i_2}) stabilizable and (A_i, C_{i_2}) detectable.

(ii) $\sum_{i=1}^{r} \alpha_i = 1$

(iii) For a compensator H_c to exist which gives finite cost J, the set of systems H_i must be simultaneously stabilizable. Conditions for simultaneous stabilization have been studied by Ghosh and Byrnes [6].

(iv) As in the estimation problem, assume uncorrelated process and measurement noise, so $\bar{B}_{i_1} \bar{D}_{i_{21}}^T = 0$. Without loss of generality, again take $\bar{B}_{i_1} = [B_{i_1} \ 0]$ and $\bar{D}_{i_{21}} = [0 \ D_{i_{21}}]$. Further, require that the measurement noise have no singular directions common to all the models, so $\sum_{i=1}^{r} \alpha_i D_{i_{21}} D_{i_{21}}^T > 0$.

(v) The dual assumptions to (iv) will also be made. That is, $\bar{C}_{i_1}^T \bar{D}_{i_{12}} = 0$, $\bar{C}_{i_1} = \begin{bmatrix} C_{i_1} \\ 0 \end{bmatrix}$, $\bar{D}_{i_{12}} = \begin{bmatrix} 0 \\ D_{i_{12}} \end{bmatrix}$, and $\sum_{i=1}^{r} \alpha_i D_{i_{12}} D_{i_{12}}^T > 0$. Note that for any individual H_i, the control weighting $D_{i_{12}} D_{i_{12}}^T$ may be singular.

14

The optimization will be restricted to the (non-empty) set of simultaneously stabilizing compensators H_c, with controllable and observable realizations.

The closed loop transfer function $H_{i_{su}}$ can be represented in state space as

$$H_{i_{su}} = \left[\begin{array}{cc|cc} A_i & B_{i_2}C_c & B_{i_1} & 0 \\ B_cC_{i_2} & A_c & 0 & B_cD_{i_{21}} \\ \hline C_{i_1} & 0 & 0 & 0 \\ 0 & D_{i_{12}}C_c & 0 & 0 \end{array} \right] = \left[\begin{array}{c|c} \tilde{A}_i & \tilde{B}_i \\ \hline \tilde{C}_i & 0 \end{array} \right] \tag{52}$$

The cost J can again be written in the form of Equation (5),

$$J(H_c) = \sum_{i=1}^{r} \text{tr}\left\{ \alpha_i \tilde{C}_i \tilde{Q}_i \tilde{C}_i^T \right\} \tag{53}$$

and again, each $\tilde{Q}_i$ satisfies a Lyapunov equation identical to Equation (6).

Necessary conditions can again be obtained using a Lagrange multiplier approach. The Lyapunov equations for $\tilde{P}_i$ are identical to Equations (8). Once again, the equation obtained by differentiating with respect to A_c is the same as Equation (11). However, for the control problem, there is a crucial difference. Each $\tilde{Q}_{i_{22}}$ and $\tilde{P}_{i_{22}}$ satisfy, respectively,

$$A_c\tilde{Q}_{i_{22}} + \tilde{Q}_{i_{22}}A_c^T + B_cC_{i_2}\tilde{Q}_{i_{12}} + \tilde{Q}_{i_{21}}C_{i_2}^T B_c^T + B_cB_c^T = 0 \tag{54}$$

$$\tilde{P}_{i_{22}}A_c + A_c^T\tilde{P}_{i_{22}} + \tilde{P}_{i_{21}}B_{i_2}C_c + C_c^T B_{i_2}^T\tilde{P}_{i_{12}} + C_c^T C_c = 0 \tag{55}$$

Thus for this problem, every $\tilde{Q}_{i_{22}}$ and every $\tilde{P}_{i_{22}}$ is different, that is $\tilde{Q}_{i_{22}} \neq \tilde{Q}_{j_{22}}$, $i \neq j$, and $\tilde{P}_{i_{22}} \neq \tilde{P}_{j_{22}}$, $i \neq j$. As a result, Equation (11) is difficult to factor, and this also has serious implications on the order of the compensator.

Proposition 15 *There is no a priori* **bound on the order of a compensator which is** *optimal for Problem 14.*

Proof: Ghosh and Byrnes [7] give an example of two second order systems, parameterized by λ, which require an arbitrarily high order compensator for simultaneous stabilization as λ tends to some limit. Since any optimal compensator must be simultaneously stabilizing, it also may be of arbitrarily high order. □

15

Remark 16 *The result in Proposition 15 has been shown before; the purpose of re-stating it here is to illustrate how the result manifests itself in the present context.*

For all three of the problems investigated in this paper, $\sum_{i=1}^{r} \alpha_i \tilde{P}_{i_{21}} \tilde{Q}_{i_{12}}$ has at most rank N. Equation (11) then yields that $\sum_{i=1}^{r} \alpha_i \tilde{P}_{i_{22}} \tilde{Q}_{i_{22}}$ has rank less than or equal to N. For controllable and observable systems H_m, H_e, and H_c, each term in this last sum has rank n_m, n_e, or n_c. In the approximation case, this sum can be factored as $P_{22} Q_{22}$, and in the estimation case, it can be factored as $P_{22} \sum_{i=1}^{r} \alpha_i \tilde{Q}_{i_{22}}$. Sylvester's inequality [15] can then be used to show that this second sum has rank equal to n_m or n_e. From this, the conclusion that $n_m \leq N$, and $n_e \leq N$ follows. In the multi-model control problem, the sum $\sum_{i=1}^{r} \alpha_i \tilde{P}_{i_{22}} \tilde{Q}_{i_{22}}$ may have maximum rank N while the individual terms in the sum can have larger rank n_c. That is, the optimal compensator may be both observable and controllable for arbitrarily large order n_c.

Theorem 17 *Suppose (A_c, B_c, C_c) solves the optimal multi-model control problem (14). Then there exist positive semi-definite matrices $\tilde{Q}_i$, $\tilde{P}_i \in \mathbb{R}^{(n_i+n_c)\times(n_i+n_c)}$ such that A_c, B_c, and C_c are the solutions of*

$$\sum_{i=1}^{r} \alpha_i \left(\tilde{P}_{i_{22}} A_c \tilde{Q}_{i_{22}} + \tilde{P}_{i_{21}} A_i \tilde{Q}_{i_{12}} + \tilde{P}_{i_{22}} B_c C_{i_2} \tilde{Q}_{i_{12}} + \tilde{P}_{i_{21}} B_{i_2} C_c \tilde{Q}_{i_{22}} \right) = 0 \quad (56)$$

$$\sum_{i=1}^{r} \alpha_i \left(\tilde{P}_{i_{22}} B_c D_{i_{21}} D_{i_{21}}^T + (\tilde{P}_{i_{21}} \tilde{Q}_{i_{11}} + \tilde{P}_{i_{22}} \tilde{Q}_{i_{21}}) C_{i_2}^T \right) = 0 \quad (57)$$

$$\sum_{i=1}^{r} \alpha_i \left(D_{i_{12}}^T D_{i_{12}} C_c \tilde{Q}_{i_{22}} + B_{i_2}^T (\tilde{P}_{i_{12}} \tilde{Q}_{i_{22}} + \tilde{P}_{i_{11}} \tilde{Q}_{i_{12}}) \right) = 0 \quad (58)$$

where $\tilde{Q}_i$ and $\tilde{P}_i$ satisfy Equations (6) and (8) respectively, with the appropriate partitioning given by Equation (7).

Proof: Equations (57) and (58) are the necessary conditions obtained directly from differentiating the augmented cost with respect to B_c and C_c. Equation (56) for A_c is obtained in the same manner as for the approximation and estimation problems. □

Remark 18 *Equation (56) can be solved for A_c using Kronecker algebra [16];*

$$\text{vec}\{A_c\} = \left(\sum_{i=1}^{r} \alpha_i \tilde{Q}_{i_{22}}^T \otimes \tilde{P}_{i_{22}}\right)^{-1} \times$$

$$\sum_{i=1}^{r} \alpha_i \left(\left(\tilde{Q}_{i_{12}}^T \otimes \tilde{P}_{i_{21}}\right) \text{vec}\{A_i\} + \text{vec}\left\{\tilde{P}_{i_{22}} B_c C_{i_2} \tilde{Q}_{i_{12}} + \tilde{P}_{i_{21}} B_{i_2} C_c \tilde{Q}_{i_{22}}\right\}\right) \quad (59)$$

Note that the inverse in Equation (59) exists. To see this, note that each $\tilde{P}_{i_{22}}$ and $\tilde{Q}_{i_{22}}$ are positive definite, and their Kronecker product is therefore positive definite [16]. The sum of these products is therefore nonsingular.

Remark 19 *If $D_{i_{21}} = \mu_i D_{21}$, $i = 1 \ldots r$ (which may not be an unreasonable assumption,) then Equation (57) can be written as*

$$B_c = \left(\sum_{i=1}^{r} \alpha_i \tilde{P}_{i_{22}}\right)^{-1} \left(\sum_{i=1}^{r} \alpha_i (\tilde{P}_{i_{21}} \tilde{Q}_{i_{11}} + \tilde{P}_{i_{22}} \tilde{Q}_{i_{21}}) C_{i_1}^T\right) V_2^{-1} = 0 \quad (60)$$

where

$$V_2 = \left(\sum_{i=1}^{r} \alpha_i \mu_i\right) D_{21} D_{21}^T \quad (61)$$

In general, B_c can be solved using Kronecker algebra. Similar comments apply to the calculation of C_c.

5   Conclusions

The simultaneous optimal approximation, estimation and control problems for multiple models has been investigated. In each problem, the order of the system to be found is fixed, and the necessary conditions that an optimal solution must satisfy are found. For both the approximation and estimation cases, the optimal model can be written as an optimal projection of a "full order" model with order $N = \sum_{i=1}^{r} n_i$. There is no improvement in the optimal cost that can be obtained by using a model with order larger than N. In the control case, there is no such *a priori* bound in terms of the individual model orders n_i that can be placed on the optimal compensator order.

References

[1] Ashkenazi, A., and Bryson Jr., A. E., "Control Logic for Parameter Insensitivity and Disturbance Attenuation," *AIAA J. Guidance,* Vol. 5, No. 4, July 1982, pp. 383–388.

[2] Miyazawa, Y., "Robust Flight Control System Design with Multiple Model Approach," *Proceedings, AIAA Guid., Nav. and Control Conf.,* Portland, OR, Aug. 1990, pp. 874-882.

[3] Gangsaas, D., Bruce, K. R., Blight, J. D., and Ly, U. "Application of Modern Synthesis to Aircraft Control," *IEEE Trans. Autom. Contr.,* Vol. AC–31, No. 11, Nov. 1986, pp. 995–1014.

[4] R. Saeks and J. J. Murray, "Fractional representation, algebraic geometry and the simultaneous stabilization problem," *IEEE Trans. Autom. Contr.,* Vol. AC–27, No. 4, Aug. 1982, pp. 895–903.

[5] M. Vidyasagar and N. Viswanadham, "Algebraic design echniques for reliable stabilization," *IEEE Trans. Autom. Contr.,* Vol. AC–27, No. 5, Oct. 1982, pp. 1085–1095.

[6] B. K. Ghosh and C. I. Byrnes, "Simultaneous stabilization and simultaneous pole placement by non-switching dynamic compensation," *IEEE Trans. Autom. Contr.,* Vol. AC–28, No. 6, June 1983, pp. 735–741.

[7] _____, "Simultaneous partial pole placement – a new approach to multi-mode system design," *IEEE Trans. Autom. Contr.,* Vol. AC–31, (1986), pp. 440–443.

[8] _____, "An approach to simultaneous system design, Part I: Semialgebraic Geometric Methods," *SIAM J. Contr. Optim.,* Vol. 24, No. 3, May 1986, pp. 480–496.

[9] ____, "Transcendental and interpolation methods in simultaneous stabilization and simultaneous partial pole placement problems," *SIAM J. Contr. Optim.* Vol. 24, No. 6, Nov. 1986, pp. 1091–1109.

[10] B. K. Ghosh, "An approach to simultaneous system design, Part II: Nonswitching gain and dynamic feedback compensation by algebraic geometric methods," *SIAM J. Contr. Optim.*, Vol. 26, No. 4, July 1988, pp. 919–963.

[11] P. M. Makila, "Multiple models, multiplicative noise and linear quadratic control-algorithm aspects," *preprint.*

[12] Hyland, D. C., and Bernstein, D. S., "The Optimal Projection Equations for Model Reduction and the Relationships Among the Methods of Wilson, Skelton, and Moore," *IEEE Trans. Auto. Contr.*, Vol. AC–30, No. 12, Dec. 1985, pp. 1201-1211.

[13] Bernstein, D. S., and Hyland, D. C., "The Optimal Projection Equations for Reduced Order State Estimation," *IEEE Trans. Auto. Contr.*, Vol. AC–30, No. 6, June 1985, pp. 583-585.

[14] Hyland, D. C., and Bernstein, D. S., "The Optimal Projection Equations for Fixed-Order Dynamic Compensation," *IEEE Trans. Auto. Contr.*, Vol. AC–29, No. 11, Nov. 1985, pp. 1034-1037.

[15] Chen, C., *Introduction to Linear System Theory*, Holt, Rinehart & Winston, 1984.

[16] Graham, A., *Kronecker Products and Matrix Calculus: with Applications*, Ellis Horwood Limited, 1981.

FORMULATION OF FULL STATE FEEDBACK FOR INFINITE ORDER STRUCTURAL SYSTEMS

$9 \angle A \ 32266$

Dr. David W. Miller and Dr. Marthinus C. van Schoor

Space Engineering Research Center
Massachusetts Institute of Technology
Cambridge, MA 02139

ABSTRACT

The exact Linear Quadratic Regulator solution for infinite order structures is the convolution of spatially distributed feedback kernels with spatially continuous state functions. For structures, several state functions exist that completely describe the state of the structure at any given point in time. The continuous control function is then the convolution of one of these state functions with an appropriate feedback kernel. If another state function is selected, a new feedback kernel can be derived that will yield identical closed-loop performance. The appropriate state function should be selected based upon the ease with which it can be measured.

This paper discusses the estimation of exact displacement and displacement rate feedback kernels from finite dimensional control solutions based on finite element structural models. These kernels are then transformed to equivalent curvature and curvature rate feedback kernels. These curvature kernels are augmented with single point displacement and rotation feedback to account for rigid body motions. The curvature and curvature rate state functions can be measured using a growing class of sensors known as area averaging sensors. The output of area averaging sensors equals the convolution of all structural curvature states with the spatial sensitivity function of the sensor. Transforming the discrete feedback gains into continuous feedback kernels and using area averaging sensors enables the implementation of full state feedback for infinite order structural systems.

1

INTRODUCTION

Rationale

Structures are infinite order systems. To obtain a mathematically exact structural model requires the use of a set of partial differential equations subjected to the appropriate boundary conditions. However, in practice it is difficult or impossible to find the exact closed-form Linear Quadratic Regulator[1] (LQR) solution for most structures. Therefore, structures are often modelled by discretization of the structure. This is even true for some very simple structures. The most common method of discretization is finite elements. When the structure is discretized, the order of the model is reduced. Instead of being modelled by an infinite order system, the structure is now modelled with a finite number of degrees-of-freedom. The result is a matrix ordinary differential equation which will approximate the temporal and spatial behavior of the structure.

Given the possibility to model a structure as an infinite order system or as a discrete finite dimensional model, it is prudent to define the terminology used in this paper. A **state function** corresponds to a motion variable which is a continuous function of both space and time. **Discrete states** or **degrees-of-freedom** correspond to point motion variables, which are functions only of time, at a finite number or locations throughout the structure (Fig. 1). The feedback of spatially discrete structural states involves feedback **gains**, whereas the feedback of a spatially continuous state function involves feedback **kernels**.

For control design, Linear Quadratic Regulator (LQR) methods exist that can be used to formulate optimal structural control solutions for these matrix ordinary differential descriptions. Given that model truncation is one of the major contributors to the control spillover problem, it is desirable to include as many degrees-of-freedom as possible in the control model. This is a costly approach, both in terms of money and in implementation since the increased

Figure 1. Graphical representation of state vector and state function description of a structure
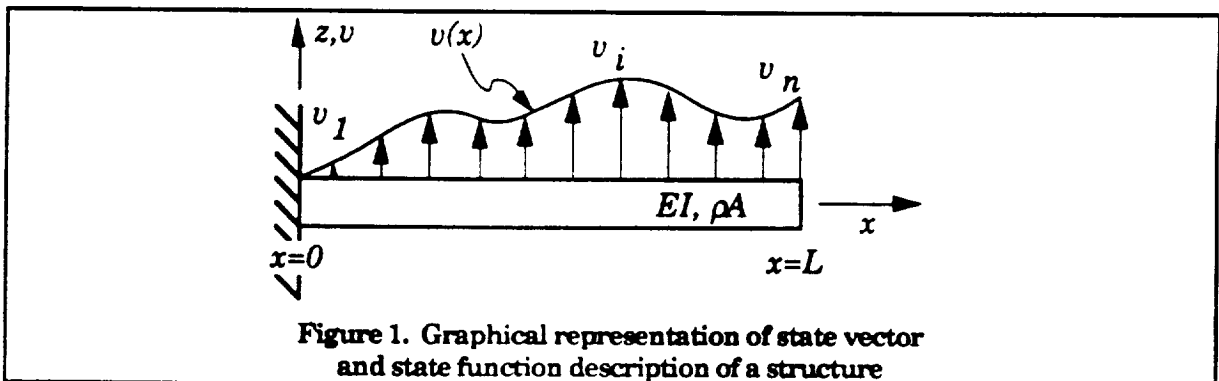
number of degrees-of-freedom requires more state sensors and the controller needs to multiply state feedback gains with the increased number of state measurements to obtain the feedback command. However, the derivation and implementation of a LQR solution, based on a infinite order model, that convolves a spatially distributed feedback kernel(s) with a spatially continuous state function(s) would completely avoid the model truncation, spatial aliasing and cost of implementation problems.

This approach contradicts two common beliefs that stems from the use of approximate, reduced order structural models. A common belief is that that the feedback architecture is typically the multiplication of gains with discrete point measurements (or estimates) of the structural motion. These measurements typically correspond to degrees-of-freedom in a finite element model. The second belief is that the type of degrees-of-freedom (displacement, rotation and their rates) used in the reduced order model are the appropriate state variables to measure.

It is also important to realize that the feedback kernels can be transformed as desired to accommodate measurements other than the states variables used in the model. Such a transformation can allow the use of not only displacement or rotation but also curvature as measurements for the infinite order controller. This paper discusses the estimation of exact feedback kernels from finite dimensional control solutions and the transformation of these kernels to accommodate the measurement of curvature. Posing the feedback in terms of curvature allows the use of a growing class of sensors known as area averaging sensors. These sensors can provide the spatially continuous measurement of the curvature required by the infinite order controller.

Implementation issues associated with these sensors are also discussed in order to demonstrate one technique for realizing the use of these feedback kernels. In this sense, the continuous kernel represents the full state feedback solution for infinite order structural systems, and the availability of at least one implementation technique makes this solution more than just a mathematical exercise.

Background

The description that is obtained of a structural system from a finite element model is a set of second order, matrix ordinary differential equations of the form

$$M\ddot{x}(t) + C\dot{x}(t) + Kx(t) = f(t) \qquad (1)$$

where M, C and K are the mass, damping and stiffness matrices, respectively. The vectors x and f contain discrete point degrees-of-freedom and force inputs, respectively. This system can be placed in first order, state-space form

$$\dot{z}(t) = Az(t) + Bu(t) \qquad (2a)$$

where

$$\begin{Bmatrix} \dot{x} \\ \ddot{x} \end{Bmatrix} = \begin{bmatrix} 0 & I \\ -M^{-1}K & -M^{-1}C \end{bmatrix} \begin{Bmatrix} x \\ \dot{x} \end{Bmatrix} = \begin{Bmatrix} 0 \\ M^{-1} \end{Bmatrix} f \qquad (2b)$$

The Linear Quadratic Regulator minimizes a cost

$$J = \frac{1}{2} \int_0^\infty \left\{ z^T Q z + u^T R u \right\} dt \qquad (3)$$

for this system by formulating a feedback gain matrix G such that

$$u(t) = -R^{-1} B^T P z(t) = -G z(t) \qquad (4)$$

where P is the solution to the steady-state matrix Riccati equation

$$PA + A^T P + Q - PBR^{-1}B^T P = 0 \qquad (5)$$

The feedback form in Eq. 4 consists of multiplying the feedback gains contained in G by the state vector in z, whose entries correspond to the temporal motions of spatially discrete points throughout the structure. The resultant products are summed to arrive at the appropriate control actions which are placed in the vector u. This feedback architecture is simply an artifact of the need to use a finite dimensional (reduced order) structural model to implement the control design.

In actuality, structures do not undergo motion only at discrete points corresponding to the model's nodes but also deform continuously throughout the region between nodes (See Fig. 1). The exact motion of the structure is described by state functions which are continuously distributed along the length of the structure. Therefore, for infinite order structural systems, the mathematically exact control inputs are not the sum of products of discrete gains with discrete motions but the general form of the control is the spatial convolution of the state function with a feedback kernel.

In order to demonstrate the concept of using infinite order structural models for control, a simple structural beam can be used as an example. The partial differential equation description of a uniform beam is

$$EI \frac{\partial^4 v(x,t)}{\partial x^4} + \rho A \frac{\partial^2 v(x,t)}{\partial t^2} = f(x,t) \qquad (6)$$

This description can be placed into state-space, spatial operator form[2]

$$\frac{\partial}{\partial t} z(x,t) = a(x) z(x,t) + b(x) u(x,t) \qquad (7)$$

by choosing the state functions as those which determine the potential (strain) and kinetic energy in the beam (curvature and transverse velocity)

$$\left\{ \begin{array}{c} \dfrac{\partial^3 v}{\partial x^2 \partial t} \\[2mm] \dfrac{\partial^2 v}{\partial t^2} \end{array} \right\} = \left[\begin{array}{cc} 0 & \dfrac{\partial^2}{\partial x^2} \\[3mm] -\dfrac{EI}{\rho A}\dfrac{\partial^2}{\partial x^2} & 0 \end{array} \right] \left\{ \begin{array}{c} \dfrac{\partial^2 v}{\partial x^2} \\[2mm] \dfrac{\partial v}{\partial t} \end{array} \right\} + \left\{ \begin{array}{c} 0 \\[1mm] \dfrac{1}{\rho A} \end{array} \right\} f \tag{8}$$

The parameter E is the modulus of elasticity, I is the area moment of inertia, A is the cross-sectional area and ρ is the volumetric mass density.

The cost is defined by

$$J = \frac{1}{2}\int_{0}^{\infty}\int_{-\infty}^{\infty}(<qz,z>+<ru,u>)dxdt \tag{9}$$

where the matrices q and r are matrix operators penalizing the state and control functions, respectively. Note that q and r are not constants but are spatial operators and that the inner integral indicates that the beam is assumed to be of infinite extent. An infinite extent beam was chosen to facilitate the acquisition of a closed-form, exact solution. However, the operator form for a finite extent beam can also be posed, although the solution will probably require numerical techniques.

The feedback structure is found from the solution pz to the functional Riccati equation

$$0 = paz + a^{*}pz + qz - pbr^{-1}b^{*}pz \qquad \forall z \tag{10}$$

where the symbol "*" signifies the adjoint operator. The feedback is the spatial convolution of a kernel matrix κ with the state function z

$$u(x,t) = -r^{-1}b^{*}(pz)(x,t) = -\int_{-\infty}^{\infty}\kappa(x-w)z(w,t)dw \tag{11}$$

where x corresponds to the location on the structure where control is applied and w indicates where states are measured. Equation 11 is the general solution because it represents the control action at any location as a function of the state functions along the entire extent of the structure. This feedback is analogous to that in Eq. 4 in the sense that it represents the continuous sum of gains times the states of the structure.

The implementation of these continuously distributed feedback kernels requires the use of a continuously distributed sensor. Several researchers have demonstrated the use of continuously distributed curvature sensors and actuators. C.K. Lee[3,4], S.E. Miller[5], S. Collins[6] and D. Miller[7] have worked on the development of area averaging sensors. These authors use spatially distributed sensors to achieve certain measurement characteristics. C.K. Lee[3,4] and S. Collins[6] used sensors shaped as particular mode shapes to obtain a measurement of the generalized coordinate of that mode. S. Collins[6] and D. Miller[7] developed sensors which roll off with frequency without exhibiting phase lag. It will be shown in this paper that area averaging sensors can be used to implement the feedback solution to a partial differential equation description of a finite extent structure.

Approach

An over optimistic goal for this research would have been to attempt to solve the infinite dimensional structural control problem. This goal is not realistic because first it would require the exact partial differential equations (PDE) and boundary conditions (BC's) that describe the dynamics of the structure and second it would be impossible in most cases to find the LQR solution even if an exact model existed. de Luis[2], for example used an infinite extent beam in solving the infinite dimensional control problem in order to find a closed-form, exact control solution. The same infinite dimensional control problem can also be posed for a finite extent beam[8]. However, this problem is much more difficult to solve due to the existence of boundary conditions.

A more realistic approach is to model the structures with the more familiar finite reduced order models (Eqs. 2 through 5) and to hope that by increasing the fidelity (number of degrees-of-freedom) of the model, the continuous feedback kernel can be inferred from the distribution of the discrete gains.

The following section discusses the derivation and implementation of continuously distributed feedback kernels. Several important steps are involved in this derivation. First, spatially discrete displacement and rotation gains derived using standard matrix Riccati techniques on finite element structural models must be converted into spatially continuous feedback kernels. Second, these kernels must be transformed into feedback of distributed curvature to facilitate implementation using area averaging sensors. An alternative approach, also discussed in the next section, is to first convert discrete displacement and rotation gains into discrete curvature gains and then to convert these gains into a spatially continuous curvature feedback kernel. Numerical examples are interspersed with these formulations to demonstrate these techniques. After the section on feedback kernel formulation, a discussion of general control issues of interest is presented along with an additional numerical examples.

Reference Example

Throughout the rest of this paper, these techniques are formulated for the cantilevered beam of length L shown in Figure 2. A control moment is applied to a point on the beam $1/10^{th}$ of the distance from the clamped root to the free tip. This moment actuator is used to represent an equivalent piezoelectric actuator at the cantilevered end. de Luis et al[2] demonstrate that one valid way of modelling the influence of a piezoelectric curvature actuator is to derive equivalent moments at the two ends of the actuator, which are of equal magnitude but of opposite sign. In this problem, if it is assumed that the piezoelectric actuator runs from the root, the companion moment at the clamped end of the beam does not enter the problem and is therefore not shown. The pertinent parameters of the problem are listed in Table 1. The performance metric is the transverse displacement of the tip of the beam (v_{tip}). The entry in the state penalty matrix (Q) corresponding to this displacement is

6

assumed to be unity. This state penalty in equation form, from Eq. 3, is

$$z^T Q z = v_{tip}^2 \qquad (12)$$


Figure 2. Cantilevered, Bernoulli-Euler beam.
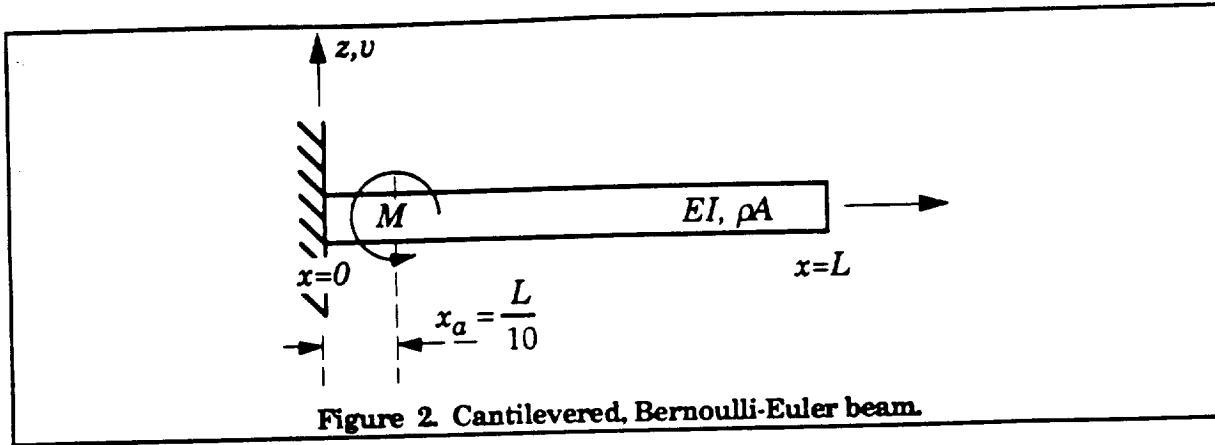
FEEDBACK KERNEL FORMULATION

This formulation process is shown in Figure 3. The upper left box represents the formulation of discrete displacement and rotation gains using classical finite element models. The objective is to evaluate the continuous curvature kernel represented by the bottom, right box. Two paths (1 and 2) can be followed to obtain the curvature kernel from the displacement and rotation gains. Following either path involves the same three steps but in different order. In either case, the first step is to evaluate the discrete displacement and rotation gains. For brevity, reference to displacement, rotation and curvature rate gains and kernels are omitted from the discussion although they are an integral part of any control design. However the evaluation of these rate gains and kernels are identical to the processes shown for the displacement, rotation and curvature gains and kernels.

Following path one, the second step involves calculating the continuous displacement kernel from the discrete displacement and rotation gains (Path 1a in Fig.3). This displacement kernel completely describes the feedback. The evaluation of a rotation kernel is redundant since it would simply be derived using the same gains that were used in deriving the displacement kernel. The third step (1b) involves transforming the displacement kernel into a curvature kernel which convolves with distributed curvature to generate the control action. This path is discussed in detail in the rest of this section.

Table 1. Parameters for cantilevered beam example.

Bending stiffness	EI	1.0 Nm^2
Mass per unit length	ρA	1.0 kg/m
Length	L	1.0 m
Actuator location	x_a	0.1 m
Control effort penalty	R	0.001

Figure 3. Matrix of feedback options.
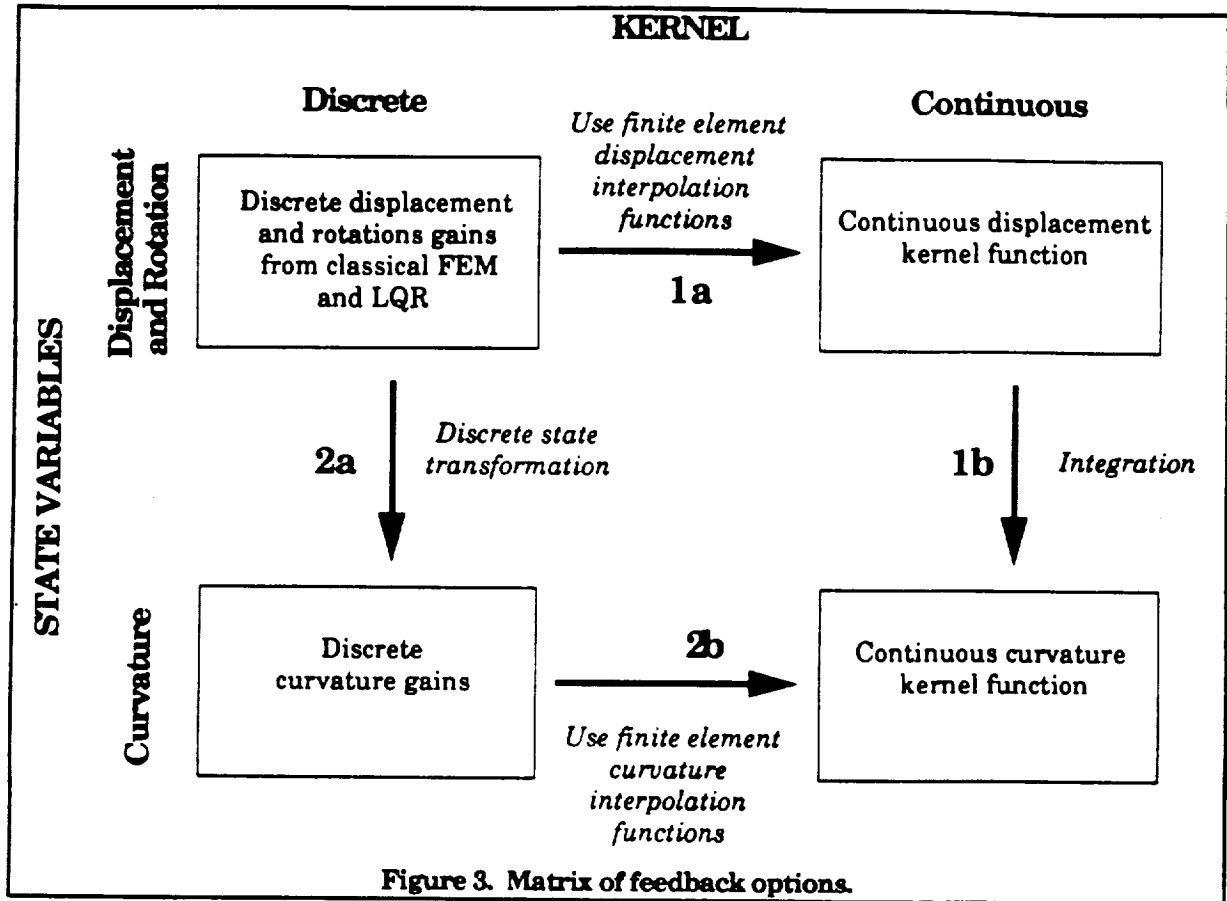
Following path two, the second step involves transforming the discrete displacement and rotation gains into discrete curvature gains (**2a**). The third step then involves using these gains to find the continuous curvature kernel (**2b**). This path is used, in the following discussion, as a check of the first path since both paths should yield approximately the same curvature kernel.

Evaluation of the Discrete Displacement and Rotation Gains

The first step in evaluating the discrete displacement and rotation gains is to develop a finite element model of the cantilevered beam. The mass and stiffness finite elements that are used in the following analysis are

$$
m_{ele} = \frac{\rho A l}{420}
\begin{bmatrix}
156 & 22l & 54 & -13l \\
221 & 4l^2 & 13l & -3l^2 \\
54 & 13l & 156 & -22l \\
-13l & -3l^2 & -22l & 4l^2
\end{bmatrix}
\quad
k_{ele} = \frac{EI}{l^3}
\begin{bmatrix}
12 & 6l & -12 & 6l \\
6l & 4l^2 & -6l & 2l^2 \\
-12 & -6l & 12 & -6l \\
6l & 2l^2 & -6l & 4l^2
\end{bmatrix}
\tag{13}
$$

with the corresponding finite element nodal degrees-of-freedom

$$v_{ele}^T = \begin{bmatrix} v_i & \dot{v}_i & v_{i+1} & \dot{v}_{i+1} \end{bmatrix}$$ (14)

where l is the element length and is equal to the total length of the beam (L) divided by the number of elements. The other parameters are listed in Table 1. It is assumed that the model is undamped. The entry in the state penalty matrix Q corresponding to this displacement is set equal to one.

Using a ten element model of the beam, the gains obtained from the LQR solver are shown in Figure 4. The gains in the upper left window are the displacement gains at discrete locations along the structure. The lower left window shows the rotation gains. Notice that no discernable spatial distribution can be seen in these gains. The windows in the upper and lower right display the displacement rate and rotation rate gains, respectively.
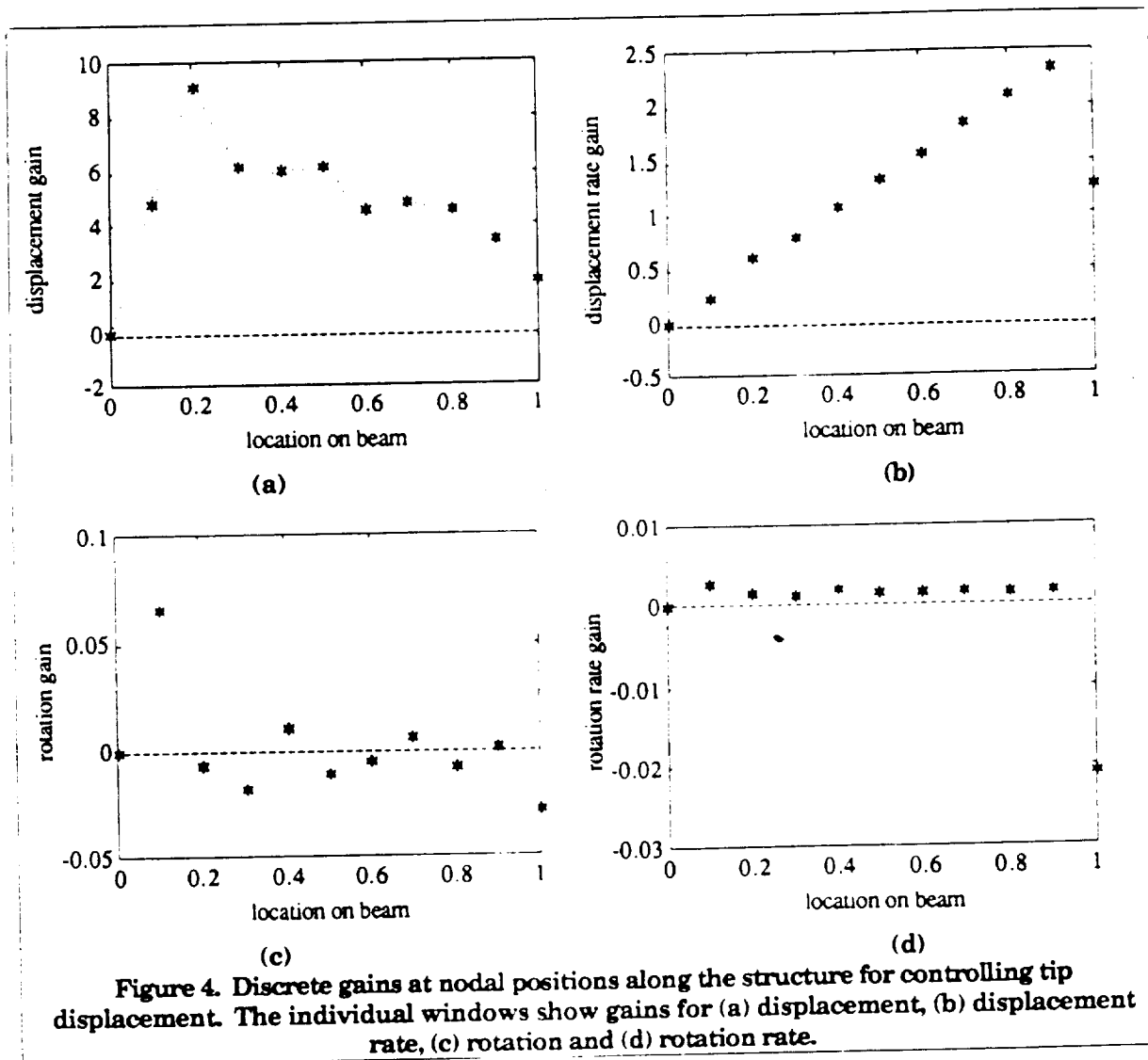
Figure 4. Discrete gains at nodal positions along the structure for controlling tip displacement. The individual windows show gains for (a) displacement, (b) displacement rate, (c) rotation and (d) rotation rate.

These displacement and displacement rate gain distributions indicate the shape that the respective continuous kernels will have, but not the magnitudes. This is only an approximate indication of the continuous shapes since the displacement kernel combines the information from both the discrete displacement and rotation gains. In other words, a single kernel contains all of the gain information displayed in a single column of Figure 4.

Evaluation of the Spatially Continuous Feedback Kernel

The next objective in the analysis is to find the spatially continuous feedback kernel from the spatially discrete gains evaluated in the previous section (Path 1a in Fig. 3). To this end, the beam finite element displacement and rotation gains will be used to derive the continuous displacement feedback kernel which convolves with the displacement state function. Since the reference example has a point actuator, the feedback convolution in Eq. 11 degenerates to the integral of a kernel times the state function. It is also convenient to use a kernel that is defined over the length of the beam, rather than having the kernel be defined, as in Eq. 11, in terms of the actuator location (x_a). Using this kernel transformation, the feedback is given by

$$
\begin{aligned}
u(t) = -\int_o^L \kappa(w)\boldsymbol{z}(w,t)dw &= -\int_0^L [\kappa_C \quad \kappa_{DR}](w)\left\{\begin{array}{c} \dfrac{\partial^2 v}{\partial w^2} \\ \dfrac{\partial v}{\partial t} \end{array}\right\}(w,t)dw \\
&= -\int_o^L \kappa_C(w)\frac{\partial^2 v}{\partial w^2}(w,t)dw - \int_o^L \kappa_{DR}(w)\frac{\partial v}{\partial t}(w,t)dw \\
&= -\int_o^L \kappa_D(w)v(w,t)dw - \int_o^L \kappa_{DR}(w)\frac{\partial v}{\partial t}(w,t)dw \\
&= u_D(t) + u_{DR}(t)
\end{aligned}
\tag{15}
$$

Note that the state functions shown in Eq. 8 include the curvature of the beam. Eq. 15 shows part of the feedback to be the integral of curvature times a curvature kernel. Alternatively, this can equivalently be expressed as the integral of the displacement state functions times a displacement kernel. This displacement kernel is derived in the next paragraph.

The integration over the entire length of the beam can be divided into the sum of integrals over segments of the structure corresponding to the finite element domains as shown in Fig. 5.
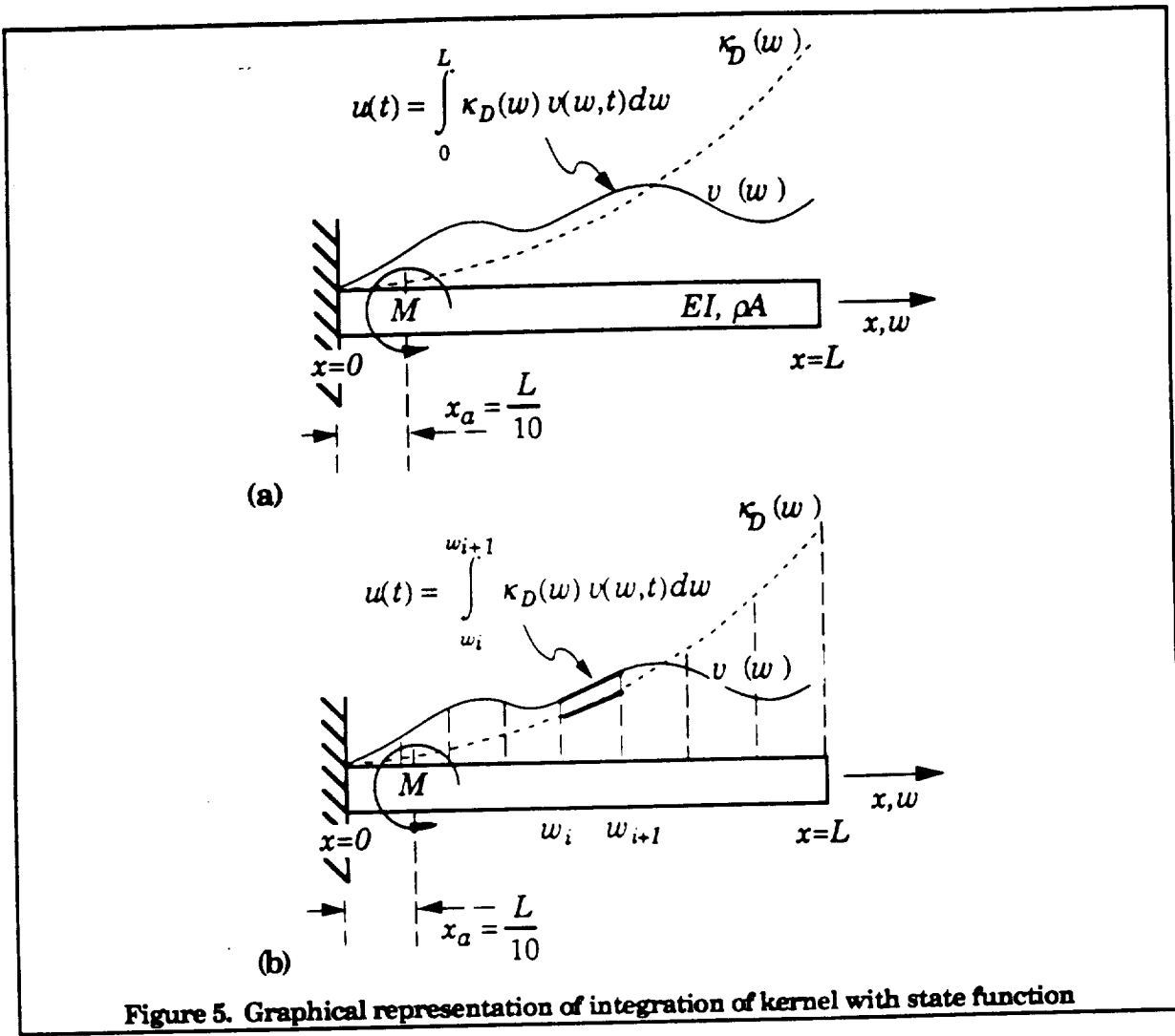
10

Figure 5. Graphical representation of integration of kernel with state function

The first half of Eq. 15 then becomes

$$u_D(t) = -\int_0^L \kappa_D(w)v(w,t)\,dw$$

$$=... - \int_{w_i}^{w_{i+1}} \kappa_D(w)v(w,t)\,dw - \int_{w_{i+1}}^{w_{i+2}} \kappa_D(w)v(w,t)\,dw - ...$$

$$=... u_{D_i} + u_{D_{i+1}} + ... \tag{16}$$

The element interpolation function description of the displacement anywhere within the element located between w_i and w_{i+1}

$$v(\xi,t) = \left(1 - 3\frac{\xi^2}{l^2} + 2\frac{\xi^3}{l^3}\right)v_i(t) + \left(\frac{\xi}{l} - 2\frac{\xi^2}{l^2} + \frac{\xi^3}{l^3}\right)l v_i'(t)$$

$$+ \left(3\frac{\xi^2}{l^2} - 2\frac{\xi^3}{l^3}\right)v_{i+1}(t) - \left(\frac{\xi^2}{l^2} - \frac{\xi^3}{l^3}\right)l v_{i+1}'(t) \qquad for \quad 0 \le \xi \le l \tag{17}$$

11

can be substituted into each of these element convolutions. Then, the control action associated with an element is a function of that element's nodal degrees-of-freedom

$$u_{D_i}(t) = - \int_{w_i}^{w_{i+1}} \kappa_D(w) \left\{ \left(1 - 3\frac{\xi^2}{l^2} + 2\frac{\xi^3}{l^3} \right) v_i(t) + \left(\frac{\xi}{l} - 2\frac{\xi^2}{l^2} + \frac{\xi^3}{l^3} \right) l \dot{v}_i(t) + \right.$$

$$\left. \left(3\frac{\xi^2}{l^2} - 2\frac{\xi^3}{l^2} \right) v_{i+1}(t) - \left(\frac{\xi^2}{l^2} - \frac{\xi^3}{l^2} \right) l \dot{v}_{i+1}(t) \right\} dw \quad where \quad \xi = w - w_i$$

(18)

If the form for κ_D were known, then the integral in Eq. 18 could be evaluated to find the the gains for the nodal degrees-of-freedom. Conversely, in this case these gains are known from the solution to the matrix Riccati equation and instead it is the form of the kernel κ_D that is being sought. To estimate this kernel, a form for the kernel, containing unknown parameters, can be selected so that the spatial integral in Eq. 18 can be evaluated. Then, these parameters can be found by equating the elements of this integration to the discrete gains. A cubic form for the kernel is chosen

$$\kappa_{D_i}(w) = a_i(w - w_i)^3 + b_i(w - w_i)^2 + c_i(w - w_i) + d_i \quad for \ w_i \leq w \leq w_{i+1} \quad (19)$$

Given the polynomial order (cubic) assumed for the four degree-of-freedom finite element, a cubic polynomial for the internal curvature distribution is the highest order polynomial for which the unknown coefficients can be uniquely found.

If the form in Eq. 19 is inserted into Eq. 18, and the integral is evaluated, the result will be the contribution that the continuous kernel across that element makes to the gains associated with that element's nodal degrees-of-freedom. In other words, at one of the element's nodes, Eq. 18 yields partial gains for the nodal degrees-of-freedom which, if summed with the gain contributions from the adjacent element, will give the total gains associated with that node's degrees-of-freedom. Thus, the gain contributions from the elements neighboring a shared node can be used to find the total displacement and rotation gains associated with that shared node

$$g_{v_i} = \int_0^l \left(a_i \xi^3 + b_i \xi^2 + c_i \xi + d_i \right) \left(3\frac{\xi^2}{l^2} - 2\frac{\xi^3}{l^2} \right) d\xi +$$

$$\int_0^l \left(a_{i+1} \xi^3 + b_{i+1} \xi^2 + c_{i+1} \xi + d_{i+1} \right) \left(1 - 3\frac{\xi^2}{l^2} + 2\frac{\xi^3}{l^3} \right) d\xi$$

(20a)

12

$$g_{v_i^{\cdot}} = \int_0^l \left(a_i \xi^3 + b_i \xi^2 + c_i \xi + d_i \right) \left(-\frac{\xi^2}{l^2} + \frac{\xi^3}{l^2} \right) l \, d\xi +$$

$$\int_0^l \left(a_{i+1} \xi^3 + b_{i+1} \xi^2 + c_{i+1} \xi + d_{i+1} \right) \left(\frac{\xi}{l} - 2\frac{\xi^2}{l^2} + \frac{\xi^3}{l^3} \right) l \, d\xi \qquad (20b)$$

where g_{v_i} and $g_{v_i^{\cdot}}$ are that node's displacement and rotation gains, respectively, as shown in Fig. 4.

These two relations give two conditions for finding for the elemental kernel coefficients a_i, b_i, c_i and d_i. Two more conditions are required in order to ensure a unique solution. These two additional conditions are found by requiring continuity of the kernel magnitude and slope at a shared node. These are found by using Eq. 19 to evaluate the magnitude and slope at the right end of the ith kernel and equating that to the magnitude and slope of the $(i+1)$th kernel at its left end yielding

$$a_i l^3 + 2b_i l^2 + c_i l + d_i - d_{i+1} = 0 \qquad (21)$$

$$3a_i l^2 + 2b_i l + c_i - c_{i+1} = 0 \qquad (22)$$

These four conditions can be expressed in matrix form as

$$\begin{bmatrix} \dfrac{3l^4}{14} & \dfrac{4l^3}{15} & \dfrac{7l^2}{20} & \dfrac{l}{2} & \dfrac{l^4}{28} & \dfrac{l^3}{15} & \dfrac{3l^2}{20} & \dfrac{l}{2} \\[2mm] -\dfrac{l^5}{42} & -\dfrac{l^4}{30} & -\dfrac{l^3}{20} & -\dfrac{l^2}{12} & \dfrac{l^5}{105} & \dfrac{l^4}{60} & \dfrac{l^3}{30} & \dfrac{l^2}{12} \\[2mm] l^3 & l^2 & l & 1 & 0 & 0 & 0 & -1 \\[2mm] 3l^2 & 2l & 1 & 0 & 0 & 0 & -1 & 0 \end{bmatrix} \begin{Bmatrix} a_i \\ b_i \\ c_i \\ d_i \\ a_{i+1} \\ b_{i+1} \\ c_{i+1} \\ d_{i+1} \end{Bmatrix} = \begin{Bmatrix} g_v \\ g_v^{\cdot} \\ 0 \\ 0 \end{Bmatrix} \qquad (23)$$

where the first two rows are found by evaluating the integrals in Eqs. 20a and 20b. A global matrix can be assembled, using Eq. 23 as the sub-matrices, to yield a linear equation relating the coefficients of the cubic-fitted kernel functions to the discrete gains

$$Tc = g \qquad (24)$$

The desired coefficients are then given by

$$c = T^{-1}g \tag{25}$$

The approximate shape of the spatially continuous displacement feedback kernel can be calculated by evaluating this piecewise cubic kernel along the length of the structure. This evaluation is made by using the coefficients in c which are appropriate for the given segment of the structure within which the kernel is being evaluated.

Using the discrete gains of the ten element finite element model (shown in Fig. 4) to evaluate the coefficients in Eq. 19 of the piecewise cubic displacement and displacement rate kernels, the functions in Figure 6 are found. These functions are the piecewise cubic kernels combined into a single curve.

Notice the erratic shape of the displacement kernel. This erratic shape may correspond to some weighted sum of mode shapes. Given that the tip displacement (performance metric) can be represented as a sum of displacement mode shapes, and that the applied moment (control input) can be represented by the sum of curvature mode shapes, the shapes in Figure 6 could correspond to some combination of the displacement and/or curvature mode shapes. In other words, these shapes may correspond to some type of mode shape 'feedthrough' from the control input to the performance metric.

(a)   (b)
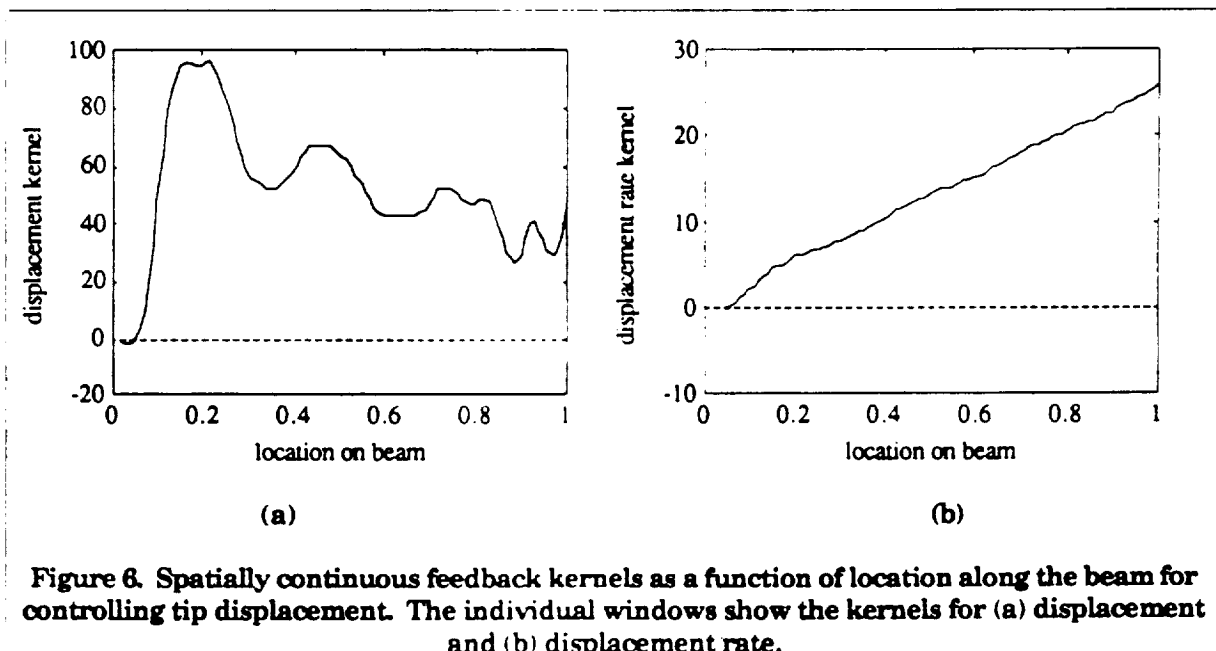
Figure 6. Spatially continuous feedback kernels as a function of location along the beam for controlling tip displacement. The individual windows show the kernels for (a) displacement and (b) displacement rate.

14

Equivalent Feedback Using Alternative State Functions

The feedback architecture using the kernel derived in the previous section has the form in Eq. 16. This involves the spatial integral of the kernel times the displacement state function. However, the continuously distributed displacement state function may not be a measurable quantity. Therefore, it may be convenient to express the same control in terms of another, more measurable state function.

Extensive work in the area of area averaging sensors[4,5,6,7,8] has shown that continuously distributed measurements of curvature-induced strain can be made using polyvinylidene flouride (PVDF). Therefore, the displacement feedback kernel of Eq. 16 must be transformed into equivalent feedback of the curvature state function.

Integration by parts can be used to transform the feedback form in Eq. 16 into equivalent feedback of the curvature state function plus point measurements of rotation and displacement, in order to retain rigid body control. This transformation is given by

$$
u_D(t) = \int_0^L \kappa_D(w)v(w,t)dw
$$

$$
= v(0,t)\int_0^L \kappa_D(w)dw + \frac{\partial v(L,t)}{\partial x}\int_0^L\int_w^L \kappa_D(\gamma)d\gamma dw -
$$

$$
\int_0^L\int_0^w\int_\gamma^L \kappa_D(\tau)d\tau d\gamma \frac{\partial^2 v(w)}{\partial w^2}dw
$$

$$(26)$$

While the point measurements of displacement and rotation must be made in order to retain rigid body measurement, the actual location on the structure where these measurements are made is arbitrary. The displacement or rotation of a point on the structure can be related to the displacement or rotation of any other point by integrating the intervening strain appropriately. For example,

$$
\frac{\partial v(L,t)}{\partial x} = \frac{\partial v(0,t)}{\partial x} + \int_0^L \frac{\partial^2 v(w,t)}{\partial w^2}dw
$$

$$(27)$$

Substituting this translation of the rotation measurement into Eq. 26 gives the equivalent feedback as

$$u_D(t) = v(0,t) \int_0^L \kappa_D(w)dw + \frac{\partial v(0,t)}{\partial x} \int_o^L \int_w^L \kappa_D(\gamma)d\gamma dw +$$

$$\int_o^L \int_w^L \int_\gamma^L \kappa_D(\tau)d\tau d\gamma \frac{\partial^2 v(w,t)}{\partial w^2}dw$$

$$(28)$$

Notice that in this equation, the first two terms, representing the feedback gains associated with point displacement and rotation measurements, can be evaluated directly from the displacement feedback kernel. The outer integral in the third term corresponds to the integration of the distributed curvature kernel with the curvature state function. The inner two integrals evaluate the curvature kernel from the displacement kernel. This curvature kernel is given by

$$\kappa_C(w) = \int_w^L \int_\gamma^L \kappa_D(\tau)d\tau d\gamma$$

$$(29)$$

The boundary conditions in the reference example were conveniently chosen to exclude rigid body motion thereby eliminating the need for any point displacement or rotation measurements. The motion of the structure is completely describable by the curvature state function because

$$v(0,t) = \frac{\partial v(0,t)}{\partial x} = 0$$

$$(30)$$

Substituting Eq. 30 into Eq. 28 yields

$$u_D(t) = \int_o^L \int_w^L \int_\gamma^L \kappa_D(\tau)d\tau d\gamma \frac{\partial^2 v(w,t)}{\partial w^2}dw$$

$$(31)$$

as the feedback law in terms of the displacement kernel. To calculate the shape of the continuous curvature kernel, Eq. 29 is employed. Equation 31 can also be used to evaluate the curvature rate kernel if the displacement rate kernel (κ_{DR}) is used in place of the displacement kernel (κ_D).

Figure 7 depicts the resulting curvature and curvature rate kernels for the ten node finite element model (Figure 4 and 6). Notice that, unlike the displacement kernel, the curvature kernel is smoother. This is predominantly due to the smoothing process inherent in the double integration of Eq. 31. Also notice that the magnitude of the kernels in Fig. 7 are largest where the cantilevered beam tends to exhibit the largest curvature: the root. In Fig. 6, the magnitude of the displacement kernel is not the largest where the beam tends to exhibit maximum displacement; namely the tip.
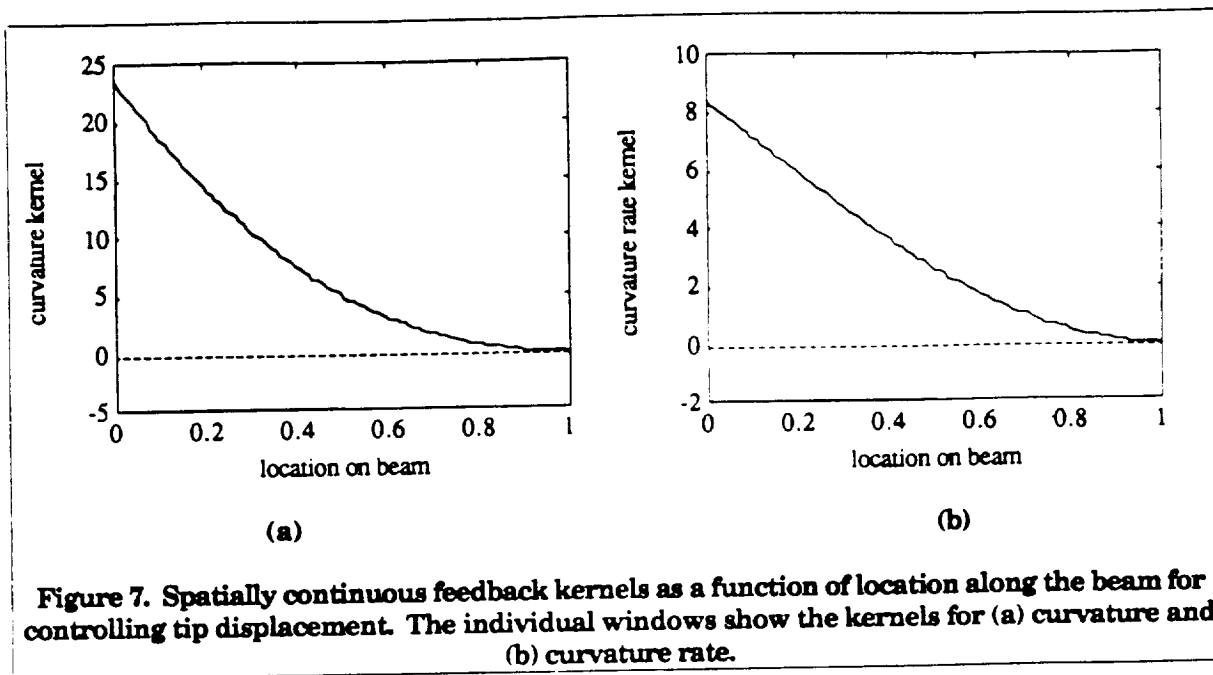
16

Figure 7. Spatially continuous feedback kernels as a function of location along the beam for controlling tip displacement. The individual windows show the kernels for (a) curvature and (b) curvature rate.

Although not shown, for this reference example, increasing control authority by decreasing the control effort penalty (R) does not change the kernel shapes. Instead, it changes the absolute and relative magnitudes of the kernels. A change in the shape of the kernel will be achieved by a change in the spatial nature of the problem such as moving the actuator or selecting a different performance metric. This observation is supported by an additional example presented later in the paper. Actual implementation of these sensors is the topic of a follow-on paper.

The results in Fig. 7 correspond to the objective represented by the lower, right box in Figure 3. The next step would be to implement these two kernel shapes using area averaging sensors. The details of this process will be discussed in the section on implementation issues. Prior to that, the next section discusses the alternate path in Fig. 3; namely path number **2**.

17

Equivalent Feedback Gains using Curvature States

An alternative procedure to evaluating the continuous curvature kernel is to first derive the discrete curvature gains from the discrete displacement and rotation gains, as shown by path **2a** in Fig. 3. This can be done in two ways. The first involves using the transformation matrix given by de Luis *et al*[2]

$$\begin{Bmatrix} v_i'' \\ v_{i+1}'' \end{Bmatrix} = \begin{bmatrix} -\dfrac{6}{l^2} & -\dfrac{4}{l} & \dfrac{6}{l^2} & -\dfrac{2}{l} \\ \dfrac{6}{l^2} & \dfrac{2}{l} & -\dfrac{6}{l^2} & \dfrac{4}{l} \end{bmatrix} \begin{Bmatrix} v_i \\ \dot{v}_i \\ v_{i+1} \\ \dot{v}_{i+1} \end{Bmatrix} \tag{32}$$

This elemental sub-matrix can be assembled into a global state transformation matrix. The number of degrees-of-freedom are not reduced by this transformation because now there exist two independent curvatures at each node. Remember, curvature is not constrained to be continuous in the beam finite element formulation because applied point moments can induce discontinuous curvature. Originally, displacement and rotation were the two nodal DOFs. Now, a node has two curvatures, one associated with the left and one with the right-hand element.

The 'o' symbols in Figure 8 indicate the net curvature gains at each node as derived using this transformation. The net curvature gain at a particular node is found by summing the individual curvature gains at that node. This procedure is justified at nodes where external moments are not applied because the two curvature gains correspond to the feedback of curvature measurements acquired an infinitesimal distance to either side of the node. Without an externally applied moment, it can be assumed that these curvature measurements are identical and therefore the net gain is the sum of the two gains.

The second approach to deriving discrete curvature gains is to integrate the displacement and rotation gain vectors to get the curvature vector. Unlike Eq. 29, this integration process involves both the displacement and rotation gains. This integral can be approximately evaluated element by element by summing the products of the gains with the element width. Other standard numerical integration techniques can also be used.

The '*' symbols in Fig. 8 represent the curvature and curvature rate gains found using this integration approach.
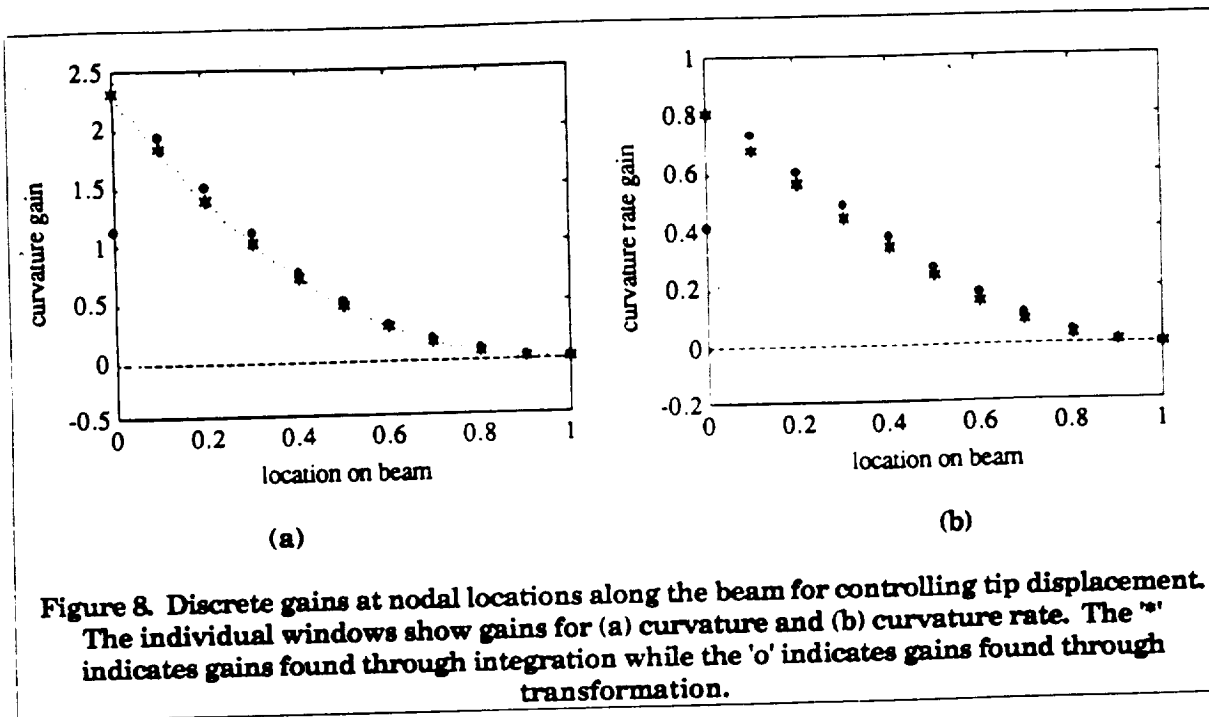
Figure 8. Discrete gains at nodal locations along the beam for controlling tip displacement. The individual windows show gains for (a) curvature and (b) curvature rate. The '*' indicates gains found through integration while the 'o' indicates gains found through transformation.

Notice the good agreement between the curvature and curvature rate gains found using the transformation and integration techniques. The agreement may seem to improve near the tip of the beam but when calculated it was found that the relative error is more less constant along the beam.

The final step in Figure 3 (2b) involves calculating the curvature and curvature rate kernels from the discrete curvature and curvature rate gains. Rather than using the technique in Eqs. 15 through 25, it can be observed that each of the discrete gains at a node roughly represents the area under the continuous kernel for the region between the midpoints of that node's neighboring elements Therefore, if the gain is divided by the length of an element, the result should be approximately equal to the magnitude of the kernel at the nodal location.

Figure 9, when compared with Fig. 7, shows that this is the case. Furthermore, Fig. 9 shows the overlay of the gains divided by respective element lengths for different fidelity models. This reveals that the magnitude of the kernel is captured quite well at nodal locations for rather coarse models for this simple reference example. This is an important result since in practice it would be generally impossible to find the exact feedback kernel from a continuous model. However, Fig. 9 illustrates that as the order of the model is increased the kernel shape is asymptotically approaching some shape. It is this shape that represents the infinite order solution and that must be implemented.
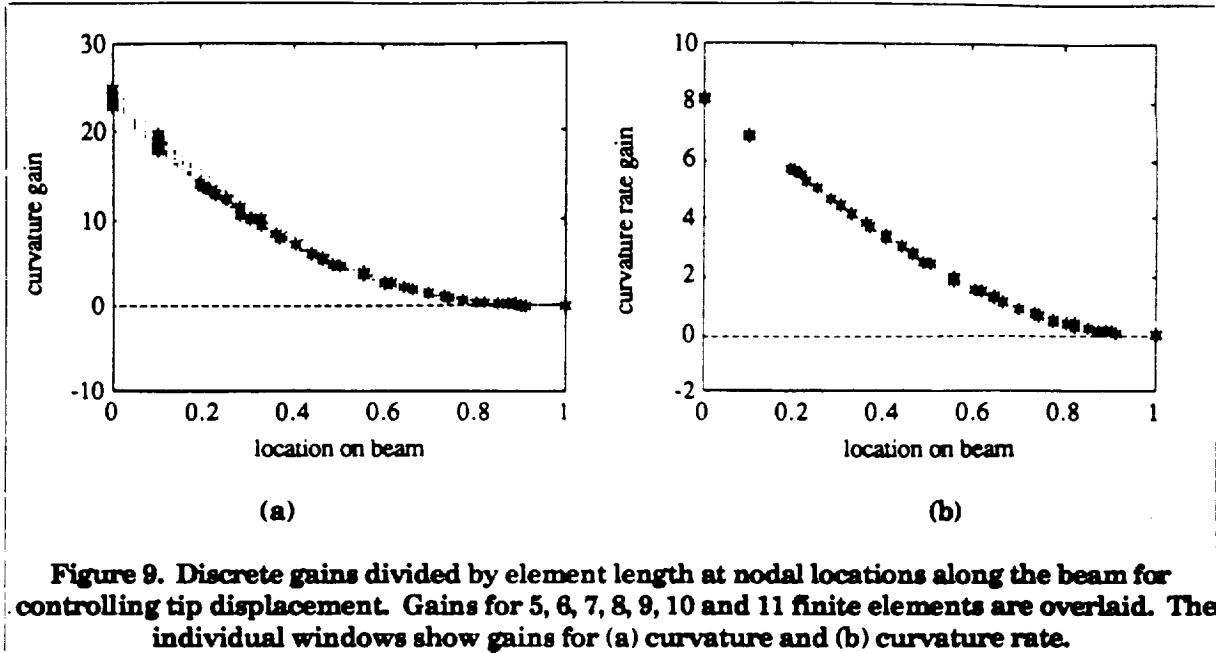
Figure 9. Discrete gains divided by element length at nodal locations along the beam for controlling tip displacement. Gains for 5, 6, 7, 8, 9, 10 and 11 finite elements are overlaid. The individual windows show gains for (a) curvature and (b) curvature rate.

Implementation Issues

The possibility of implementing infinite order structural controllers is made possible by the existence of area averaging sensors such as those described in References 4,5,7 and 8. Once the curvature kernel is obtained, it is a simple calculation to alter the kernel for equivalent feedback of curvature-induced surface strain. This simply requires knowledge of the distance of the surface mounted sensor from the centroidal axis in the structure. Once this kernel is found, the sensor can be built.

Polyvinylidene flouride (PVDF)[9] is suggested for this sensor for several reasons. First, PVDF is a strain sensitive material which can be continuously distributed along the surface of a structure and whose accumulated charge on a surface electrode equals the integral over the length of the PVDF of the electrode width times the surface strain in the structure. Second, PVDF has an elasticity which is relatively small when compared to the elasticity of conventional structural materials. This allows the sensor to be rather non-intrusive into the dynamics of the structure. Third, the shape of the electrode can be easily altered to equal that of the kernel while leaving the actual PVDF material uniformly distributed. This achieves the strain sensitivity appropriate for implementing the kernel while keeping the small dynamic influence that the PVDF does exert on the structure uniformly distributed. In addition, removal of electrode from near the edge of the PVDF greatly reduces the possibility of the sensor shorting its bottom and top surface electrodes. A fourth and final reason for using PVDF is its high strain sensitivity which provides an excellent signal to noise ratio for control purposes.

One drawback of implementing the feedback kernel through the shaping of the

electrode is that once the electrode is shaped and the material is mounted on the structure, the kernel is effectively fixed and cannot be altered. Feedback gains which reside in a computer can be readily altered if alteration is required. However, C. K. Lee in Reference 4 has developed a method which could be used to circumvent this inflexibility in the gains. He uses an area averaging sensor whose electrode is segmented into numerous squares and the voltages on these squares are summed as appropriate for a particular gain distribution. If the gain distribution needs to be altered, the manner in which these voltages are summed can be changed.

Throughout the discussion of full state feedback for infinite order systems, there was an implicit assumption that high frequency dynamics in the structure consisted solely of additional modes which would be properly modelled given the use of a sufficient number of finite elements. However, this is seldom, if ever, the case in actual structures. Often, torsion or out-of-plane bending modes exist irrespective of whether only in-plane bending was modelled. These dynamics may feed through to the output of the sensor. Therefore, the spatial wavenumber filtering concepts presented in Reference 8 could be used to roll off, without phase lag, the frequency response of the spatially continuous sensor.

Figure 10 illustrates the way in which a PVDF area averaging sensor was implemented in Reference 8. The electrode is shaped as a decreasing exponential in two directions. Note that the sensor may have to be segmented if the PVDF sheet is not as long as the kernel. Given that PVDF is a polarized material, a negative part of the kernel can be implemented by either flipping that segment of the PVDF or reversing leads (see Reference 8).

For the reference example discussed thus far, two PVDF electrodes could be shaped: one each as shown in Figs. 7a and 7b. Bonding these two sensors to either side of the cantilevered beam, one sensor for the curvature kernel and one for the curvature rate kernel, the two sensor voltages can be summed appropriately and used to drive the control moment.

The unique feature of this technique is that the processes of multiplying the gains times the curvature measurements and accumulating these products is performed by the sensor. This feature significantly reduces the control implementation effort associated with numerous point sensors.

Figure 10. Illustration of the implementation of an area averaging sensor using PVDF shaped in an exponential fashion.
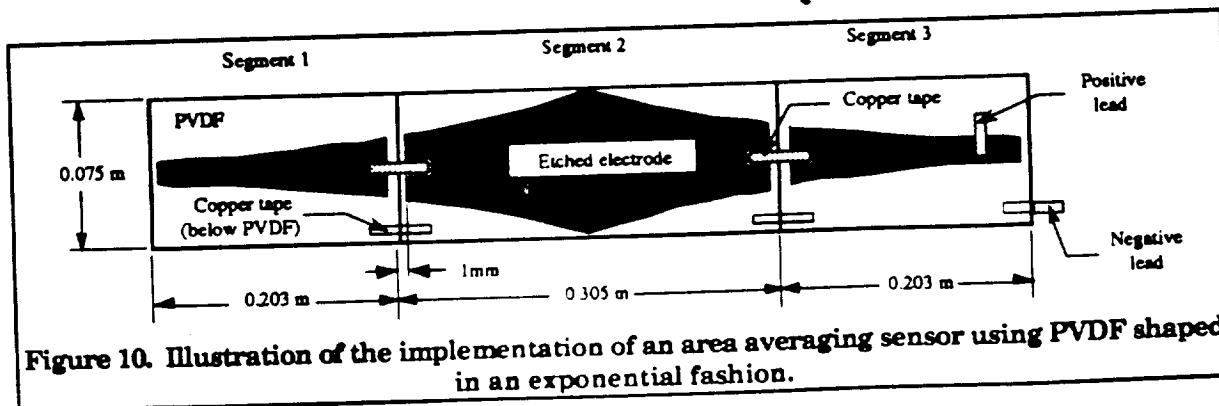
Issues associated with controllers based on classical beam finite elements

The previous section has shown how PVDF sensors can be used to implement infinite order controllers. It was also shown in Figure 9, that finite elements models can be used to predict the shape of the infinite order feedback kernel. The hope is that by progressively increasing the order (accuracy or fidelity) of the finite element model, the shape of the feedback kernel will approach some asymptotic shape. It is this shape that represents the infinite order feedback kernel and that must be implemented with PVDF.

Classical finite elements are the obvious elements to be used in such a model refinement process. This study has identified two implementation problems that are uniquely associated with these classical beam finite elements. The first is that the stiffness matrix obtained with these classical beam elements becomes ill-conditioned as the element size decreases. Decreasing the element size is typically associated with increasing model fidelity. This is illustrated by looking at the conditioning number of the stiffness matrix of a cantilevered beam obtained by using the following classical beam finite element:

$$ k_{ele} = \frac{EI}{l^3} \begin{bmatrix} 12 & 6l & -12 & 6l \\ 6l & 4l^2 & -6l & 2l^2 \\ -12 & -6l & 12 & -6l \\ 6l & 2l^2 & -6l & 4l^2 \end{bmatrix} \tag{33} $$

The conditioning number for a matrix is the ratio obtained by dividing the largest eigenvalue by the smallest eigenvalue of the matrix. The higher the conditioning number of a matrix, the more ill-conditioned the matrix is and the more likely that matrix will be susceptible to computer round-off errors. It can be shown[10] that the conditioning number is proportional to:

$$ Cond \propto \frac{1}{l^2} \tag{34} $$

Thus as more elements are used and the element length (l) decreases, the matrix becomes ill-conditioned and results from the LQR routine will become less reliable.

A second problem associated with classical finite element models is a problem of non-uniqueness. From finite difference theory it is known that rotation can be estimated from discretized displacements as:

$$ v_i^{\cdot} = \frac{v_{i+1} - v_{i-1}}{2l} + O\left(l^2\right) \tag{35} $$

In Eq. 35, $v_i^{\cdot}$ is the nodal rotation and v_i's is the nodal deflection. The truncation error, which is of order l^2, will decrease as the element size (l)
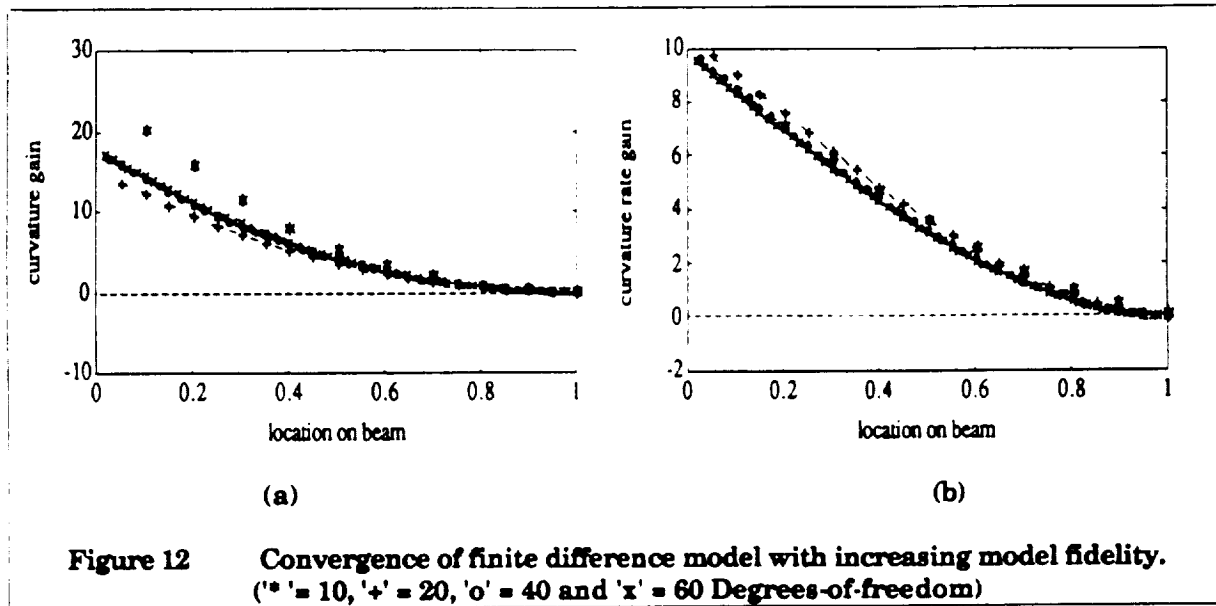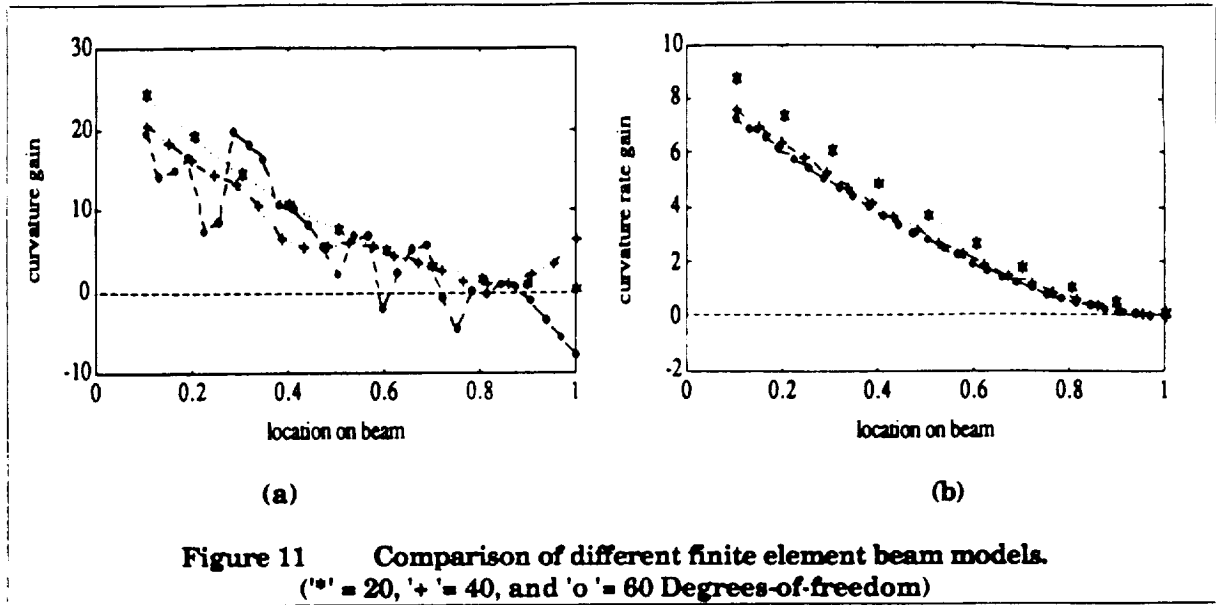
22

decreases, indicating that the finite element nodal rotations ($\dot{v}_i$) can be expressed as linear combinations of the nodal displacements (v_i) with increasing accuracy. The manifestation of this problem lies in the interpretation of the feedback gains calculated by the LQR algorithm. Given that the nodal rotations may become linearly dependent on the nodal displacements (or vice versa), the gains obtained by the LQR algorithm may yield an optimal solution but the displacement and rotation gains may not be unique.

These two problems are investigated by comparing the results of two discretized models used to solve the reference cantilevered beam example. The first model is the classical finite element beam model, while the second is a second order accurate finite difference model. In the finite difference mode, the stiffness term in the governing differential equation (Eq. 6) is approximated by:

$$EIv_i^{''''} = EI\left[\frac{v_{i+2} - 6v_{i-1} + 4v_i - 6v_{i-1} + v_{i-2}}{l^4}\right] + O\left(l^2\right) \tag{36}$$

The effects of ill-conditioning and non-uniqueness are investigated by comparing the results of models in which the fidelity of the model is increased by increasing the number of nodes. Both these models should exhibit the ill-conditioning problem since the finite difference model also has a conditioning number that will increase (deteriorate) as the element size decreases since the conditioning number is approximately $1/(l^2)$ [10]. The finite difference model, however, should not exhibit the non-uniqueness problem associated with the finite element model. These conclusions are supported by the results of the investigation. Although not shown, both the models exhibit ill-conditioning problems and the Riccati solver failed to yield a solution for a model with 40 nodes (or 80 degrees-of-freedom) for the finite element model and 80 degrees-of-freedom for the finite difference model. However, the finite element model may exhibit the non-uniqueness problem as the fidelity of the model is increased. In Fig. 11 the distribution of curvature gains becomes erratic as the number of nodes are increased above 10. The finite difference model on the other hand, as shown in Fig. 12 does not exhibit this behavior. Even with these erratic gains, the closed loop finite element models are stable with identical closed loop poles for the first five modes. This observation leads to the conclusion that this behavior may be due to the non-uniqueness problem associated with these elements.

Note that the slow convergence to the "infinite" shape of the finite difference model is due to the method in which the point moment is applied to the structure. An applied point moment is achieved by applying appropriate forces to nodes neighboring the node to which the moment must be applied.

Figure 11   Comparison of different finite element beam models.
('*' = 20, '+ '= 40, and 'o '= 60 Degrees-of-freedom)

Figure 12   Convergence of finite difference model with increasing model fidelity.
('* '= 10, '+' = 20, 'o' = 40 and 'x' = 60 Degrees-of-freedom)

AN ADDITIONAL NUMERICAL EXAMPLE

An additional numerical example involves the control of the relative transverse displacement between the tip and the middle of the beam. This state penalty has the form

$$q\left(v_{tip} - v_{middle}\right)^2 = q\left(v_{tip}^2 - 2v_{tip}v_{middle} + v_{middle}^2\right) \qquad (37)$$

For this example, the scalar q is unity.

Figure 13 shows the discrete gains. Again, the displacement and rotation gains are rather erratic. However, the curvature and curvature rate gains are smooth. Figure 14 shows the continuous feedback kernels. While the curvature rate kernel has a shape similar to that in the previous example, the curvature kernel now undergoes a change in sign. All the curves seem to have an inflection point near the midpoint of the beam $(x=0.5)$.

CONCLUSIONS

A technique has been presented for inferring the exact, spatially continuous LQR feedback solution to the control of structures from the discrete feedback gains derived using finite dimensional structural descriptions. These feedback kernels possess several unique attributes. First, it has been shown that feedback of the state functions can be transformed to equivalent feedback of other state functions. This aids in implementation because the feedback can be derived in terms of the state function that is most easily measured. Area averaging sensors provide one means for implementing these spatially continuous feedback kernels. Second, these continuous sensors can eliminate spatial aliasing. Spatial aliasing is one of the primary causes of spillover in structural control. Third, all of the feedback computation can be effectively performed by an area averaging sensor.

The research presented in this paper must be seen as the first step in an attempt to formulate and implement full state feedback for infinite order structural systems. Several issues must be resolved before this approach can be considered a viable alternative to reduced order controllers. For example: the accuracy with which the area averaging sensors must match the desired kernel must be investigated. Robustness of this control approach must be determined and the theory must be demonstrated in the laboratory. The researchers are presently working on these topics and plan to implement an infinite order controller on a cantilevered beam using the actuator and performance metric presented in the reference example.
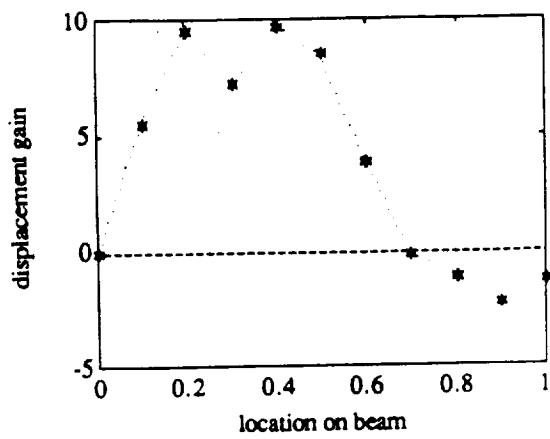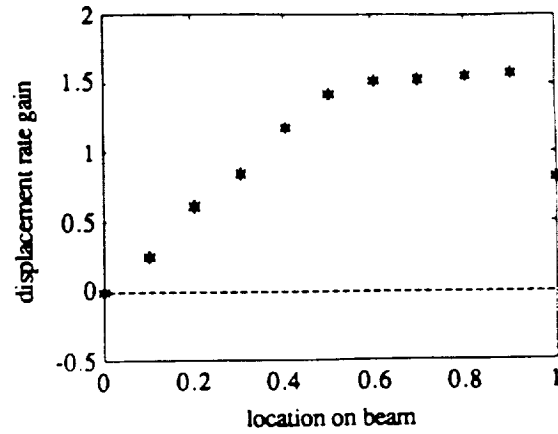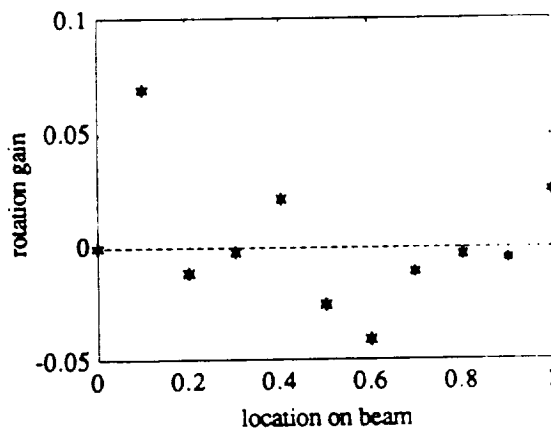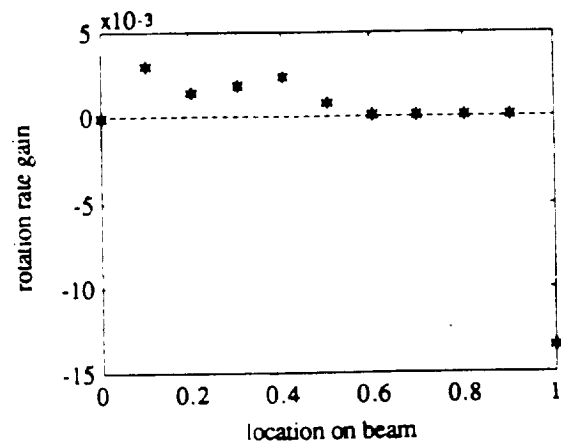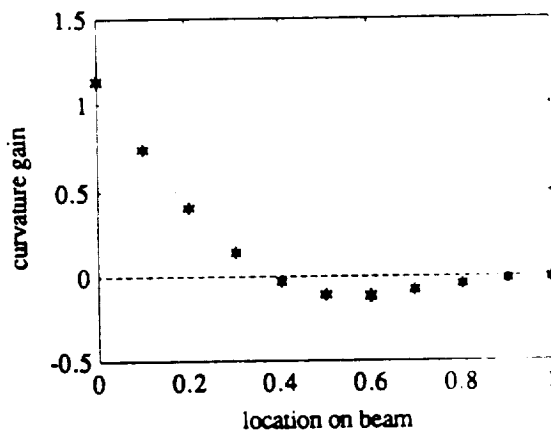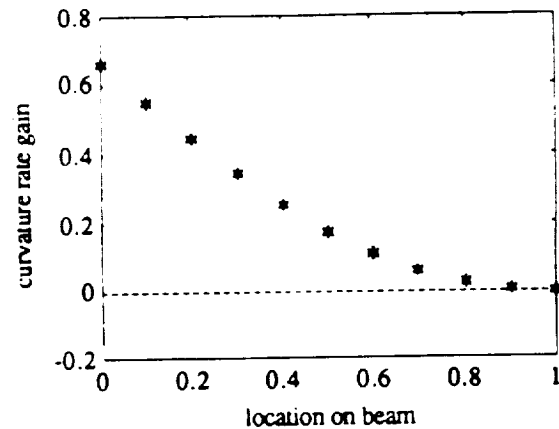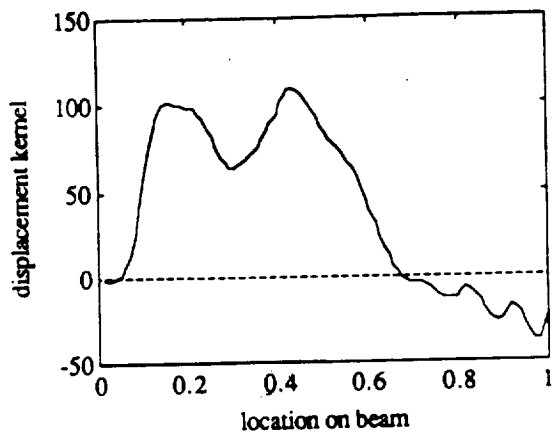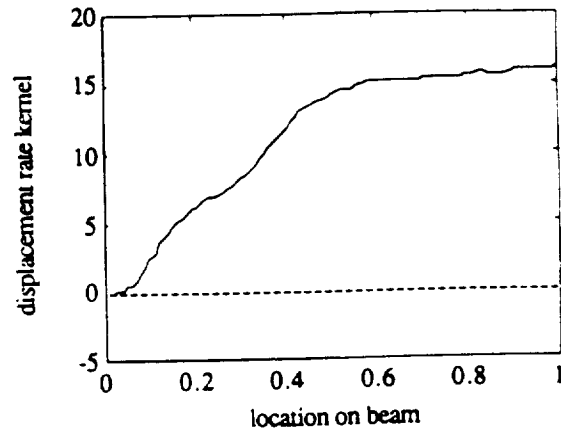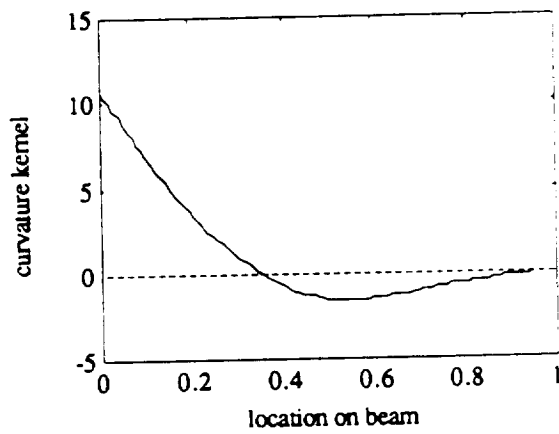
Figure 13. Discrete gains at nodal positions along the structure for controlling relative displacement between the tip and midpoint. The individual windows show gains for (a) displacement, (b) displacement rate, (c) rotation, (d) rotation rate, (e) curvature and (f) curvature rate.
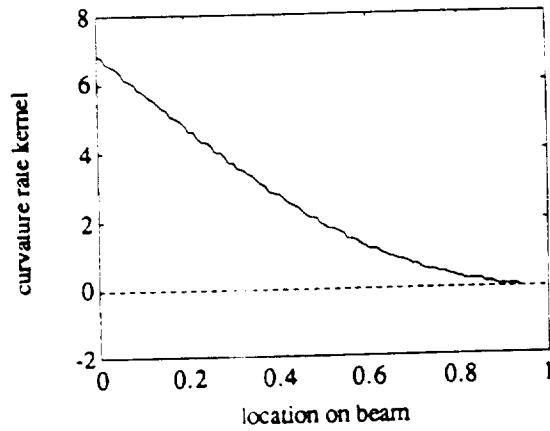
Figure 14. Spatially continuous feedback kernels as a function of location along the beam for controlling relative tip displacement. The individual windows show the kernels for (a) displacement, (b) displacement rate, (c) curvature and (d) curvature rate.

ACKNOWLEDGEMENTS

REFERENCES

1.   Kwakernaak, H and Sivan, R., *Linear Optimal Control Systems*, John Wiley and Sons, Inc., New York, 1972.

2.   de Luis, J., Crawley, E.F. and Hall, S.R., "Design and Implementation of Optimal Controllers for Intelligent Structures Using Infinite Order Structural Models," Space Systems Laboratory Report No. 3-89, M.I.T., Cambridge, MA, 1989.

3.   Lee, C. K., "Piezoelectric Laminates for Torsional and Bending Modal Control: Theory and Experiment," PhD Dissertation, Cornell University, Ithaca, NY, 1987.

4.   Lee, C. K., Chiang, W. W. and O'Sullivan, T.C., "Piezoelectric Modal Sensors and Actuators Achieving Critical Damping on a Cantilever Plate," *Proc. of the AIAA/ASME/ASCE/AHS/ASC 30th Structures, Structural Dynamics and Materials Conference*, Mobile, AL, April 3-5, 1989, pp. 2018-2026.

5.   Miller, S.E., Hubbard, J., "Theoretical and Experimental Analysis of Spatially Distributed Sensors on a Bernoulli-Euler Beam," Charles Stark Draper Laboratory Report C-5953, Cambridge, MA, 1987.

6.   Collins, S.A., Notestine, R.J., Padilla, C.E., Ramey, M., Schmitz, E. and von Flotow, A.H., "Design, Manufacture, and Application to Space Robotics of Distributed Piezoelectric Film Sensors," Proceedings of the 31st AIAA/ASME/ASCE/AHS/ASC Structures, Structural Dynamics and Materials Conference, Long Beach, CA, April 2-4, 1990, Paper No. AIAA-90-0949, pp. 1899-1906.

7.   Miller, D. W., Collins, S. A. and Peltzman, S. P., "Development of Spatially Convolving Sensors for Structural Control Applications," Paper # AIAA-90-1127, Proceedings of the 31st AIAA/ASME/ASCE/AHS Structures, Structural Dynamics, and Materials Conference, Long Beach, CA., April 1990, pp. 2283-2297.

8.   Bailey, T., Hubbard, J. E., "Distributed Piezoelectric-Polymer Active Vibration Control of a Cantilevered Beam," *Journal of Guidance, Control and Dynamics*, Volume 8, Number 5, Sept. 1985, pp. 605-611.

9.   *KYNAR Piezo Film Technical Manual*, Pennwalt Corp., Valley Forge, PA, 1987.

10.   Strang, G., *Linear Algebra and Its Applications*, Second Edition, Academic Press, New York, 1980.

on a structure in order to modify its dynamic behavior to meet its performance requirements. Unfortunately, active control introduces the possibility of exciting the structure in an unstable manner making it critical that either confidence in the prediction of on-orbit behavior be improved or the types of tests required for *qualification* be identified.

Before proceeding with a discussion of the experimental approach to *developing* qualification procedures, it is necessary to present the rationale that lead to MACE. After all, conducting experiments on-orbit, even those which are performed on the STS middeck, is technically risky, expensive, requires extensive planning, and produces less data than would be obtained in a comparable ground experiment. The program must clearly exploit the unique aspects of the on-orbit environment in order to justify its conduct.

The objective of this paper is to portray the rationale for conducting this type of flight experiment and to pose the scientific questions to be addressed through this research. Additionally, the test article will be described, along with the ground and on-orbit experiment support equipment. This paper concludes with a discussion of planned on-orbit activities.

OBJECTIVES AND RATIONALE

The goal of MACE is to develop a well verified set of CST tools that will allow designers to either be able to predict on-orbit behavior or allow sufficient versatility in the design to allow identification and tuning of the structure on-orbit. A number of different options exist for deriving this set of tools. The first and least expensive is to rely on analysis for the design and qualification of spacecraft which incorporate CST. Unfortunately, this approach is far less than satisfactory. The scientific literature is riddled with examples of both closed and open-loop experiments whose performance varied greatly from that predicted by state-of-the-art analytical methods. The reasons behind this are varied. Often the structural or sensor/actuator characteristic which contributes to this performance degradation is not the next detail that would have been included in the analytical model. Its existence is usually not predicted but instead is discovered through experimentation. This experience illustrates that analysis alone is not sufficient.

The question that next arises is what sort of testing needs to be performed, along with analysis, in order to *develop* an effective and efficient spacecraft *qualification* procedure. Four different options exist. Listed in ascending order from lowest to highest cost and complexity, they are: ground-based open-loop experiments, ground-based closed-loop experiments, on-orbit open-loop experiments and on-orbit closed-loop experiments.

Ground-based open-loop testing is the simplest type of experimental program that can be carried out to verify the validity of analytical models. It is an absolutely necessary step, since the quantities that are most required for closed-loop control design are exactly those which are hard to predict analytically For example, structural modal frequencies can be predicted using numerical methods with a relatively high degree of accuracy. Conversely, modal damping values are extremely hard to predict analytically on large complex structures where many energy dissipation mechanisms are present. Unfortunately, closed-loop controllers for

structures usually require accurate knowledge of the modal damping because damping determines stability margins and therefore performance. This problem is exacerbated in structures that are lightly damped, such as LSS.

It is easily concluded, therefore, that ground-based open-loop testing is essential to quantify the accuracy of analytical models. However, these tests by themselves are not sufficient to validate the appropriateness of an analytical model or the performance of a closed-loop system. Skelton[3] has demonstrated that no measures of accuracy of the open-loop model are sufficient to guarantee stability of a closed-loop system at arbitrarily high gain. This implies that the acquisition of the open-loop model can never be sufficient to predict closed-loop performance. Therefore, ground-based closed-loop testing is absolutely necessary for the successful application of CST to realistic structures.

Since CST structures will be used in the space environment, it is important to investigate whether those characteristics that are present on-orbit and cannot be adequately simulated on earth affect the open and closed-loop tests. In Table 1 various vehicle parameters are listed along with four significant differences that occur between on orbit and ground-based tests. The table indicates that these differences do affect the vehicle parameters.

Table 1 The various structural, kinematic and dynamic parameters that can differ between on-orbit and ground tests.

	Aero/ Acoustic	Suspension	Gravity	Thermal/ Radiation
Stiffness	no	yes	yes	yes
Damping	yes	yes	yes	yes
Mass	yes	yes	no	no
Forcing	yes	yes	no	no
Kinematics	no	yes	yes	no

The important issue is whether the differences in Table 1 cause *regular* or *singular* perturbations to the problem. A regular perturbation is one whose affect on the vehicle parameter disappears as the perturbation is allowed to approach zero. This is in contrast with a singular perturbation whose presence substantially modifies the vehicle parameter even as the perturbation approaches zero. If the perturbations are regular, then they can be modelled and the results from the ground-based tests can be more easily used to predict on-orbit behavior. However, they may still have a very substantial, although predictable effect on the structural parameter. For example, small changes in the plant can often lead to large changes in the modal damping or in the mode shapes, two quantities that have a direct effect on closed-loop stability and actuator and sensor performance. Therefore, if the plant is highly sensitive to regular perturbations due to influences listed in Table 1, it is probably necessary to conduct open-loop on-orbit testing. If the perturbations are singular, it is essential to conduct open-loop testing on-orbit in order to identify and adjust for these perturbations.

The only issue that now remains to be addressed is whether on-orbit closed-loop testing is still required. The answer to this question depends on whether any singular perturbations are identified during the on-orbit open-

loop experiments, or whether any regular perturbations cause significant unpredictable changes in the plant. If the answer to either of these questions is "yes", then on-orbit closed-loop testing is essential.

A preliminary analysis does not reveal any singular perturbations arising from one of the four sources shown in Table 1. Non-convective potential aeroacoustic equations do not give rise to singularities, nor do conservative fields such as gravity. So long as suspension devices are passive or collocated active, they do not introduce singularities. Since the thermal/radiation terms only affect otherwise symmetric stiffness and damping parameters, they also do not give rise to singular perturbations.

However, a situation in which a regular perturbation can have significant effect on the closed-loop performance of the structure can be easily imagined. The stiffness added by a suspension system, even if small, can change the modal structure. Additionally, for an articulated test article, a suspension system could introduce an unexpected kinematic constraint. Gravity can change preload on a joint, and hence damping. Gravity will also cause otherwise straight members to curve, causing significant changes in the modal structure, such as nonplanar coupling of modes. Therefore, while no singular perturbations have been identified, there are a number of regular perturbations which can cause significant changes in the plant that could result in control performance being degraded.

Therefore, the conclusion that is reached is that ground-based open and closed-loop testing is not sufficient for the verification of CST technology. At a minimum, on-orbit open-loop testing would need to be conducted to test for the presence of any singular perturbations, or any significant regular perturbations. If these perturbations are found to exist, then on-orbit closed-loop testing becomes essential as argued by Skelton. If they are not present, then the closed-loop tests might still be needed if a suitable ground-based performance metric or disturbance environment is unobtainable, or, more likely, if the additional cost of conducting the closed-loop experiments were incremental.

Having demonstrated the likely necessity of on-orbit closed-loop testing, a test article on which to perform the experiments must now be selected. A survey of proposed future spacecraft was undertaken and an evaluation was made on which type of spacecraft exhibit the most requirements for CST and which were most limited by earth-bound testing.[4,5] Some of the spacecraft types that were considered included two point alignment occulting instruments, multipoint alignment interferometric devices, shape control of reflective surfaces, flexible manipulators, and multipayload platforms. This latter type was selected because the large angle motions of the payloads stress state-of-the-art suspension devices and because of its applicability to missions of near term interest.

Proposed missions which will use this type of spacecraft include low and geosynchronous platforms in the Mission to Planet Earth, the evolutionary International Space Station, and the planetary orbiting platforms of the Exploration Initiative. As these platforms become larger and more complex, the propensity for individual on-board controllers to interact with each other and with the bus attitude control system will grow. This propensity is exacerbated by increasing payload mass fraction associated with larger instruments and robotic devices, decreasing structural bus stiffness associated with larger platforms, increasing authority of the controllers associated with tighter pointing and positioning requirements, and the increasing need to reject disturbances which originate at other payloads. This rationale makes clear the need to develop a well verified set of CST tools. This development must:

1. The development of a comprehensive analytical CST framework for the design and analysis of controlled multibody platforms. This analysis begins with an understanding of how flexibility influences the pointing and tracking performance of multibody platforms, and must be able to include the influences of suspension and gravity for use in correlating with ground test results, and to exclude the influence of suspension and gravity for use in predicting on-orbit results.

2. The validation of the analytical framework by comparison with a set of ground based experiments with a test article which incorporates the essential physical characteristics of a multibody platform. This test will, of necessity, include the influence of gravity and suspension, and will be typical of the preflight ground testing of an actual platform.

3. The validation of the analytical framework by comparison with a set of on-orbit zero gravity experiments which eliminate the influence of gravity and suspension.

The specific criteria which will determine experiment success of MACE are the identification of the regular (and, if they exist, singular) perturbations in the dynamics which occur as a result of the change from one to zero gravity, and the production of the data for the final validation of the analytical framework. The ultimate result of MACE will be a well verified modelling capability for the controlled structures design and qualification of future multibody platforms, and a detailed understanding of the parametric tendencies in vehicle dynamics, geometry and performance requirements, which cause the zero gravity closed-loop behavior to differ from the one gravity results. This capability can be exploited by future spacecraft designers to either obtain confidence in the on-orbit performance of their CST spacecraft before they are deployed, or to design enough versatility into the spacecraft in order to accommodate any unexpected deviation between ground and on-orbit behavior.

EXPERIMENTAL APPROACH

The fulfillment of the basic objective of the MODE 2 program requires two steps. First, the research must validate the analytical framework for the design and analysis of controlled multibody platforms by comparison with a set of *ground based* experiments on a test article which incorporates the essential physical characteristics of envisioned multibody platforms. Second, the research must also validate the analytical framework by comparison with a set of *zero gravity* experiments with a test article similar to that used in the ground tests. These objectives necessitate two aspects of the experimental approach: the capture of the essential physical characteristics of multibody platforms in the design of the MACE test article, and the performance of

meaningful tests which validate the analytical framework through a coherent on-orbit and ground test program.

Capturing the Essential Physics

To arrive at the essential physical characteristics of multibody platforms, one must consider the vehicle architecture of the missions which are envisioned by the international space community.[6] In such platforms, the payloads and articulating appendages each have pointing or positioning requirements, and corresponding attitude sensors, pointing gimbals and control systems. The spacecraft structural bus is flexible and has its own attitude control system. The simulation of this vehicle architecture, in its associated operational environment, necessitates a test article with the following attributes:

- a test article designed with the appropriate multiple scaling laws to allow it to fit in the middeck, yet preserve the essential performance requirements of a full scale test article,
- the incorporation of at least two gimballing payloads to enable the implementation of multiple interacting control systems with independent objectives,
- the incorporation of two rigid payloads, representative of compact but high mass fraction devices, and a flexible appendage, interchangeable with one payload, representative of an articulating appendage such as a robotic servicer,
- a sufficiently flexible structural bus such that flexible resonances lie within the controller bandwidth,
- a sufficiently flexible structural bus which, when suspended even from state-of-the-art suspension devices, exhibits a degree of suspension coupling, gravity stiffening and droop,
- a sufficiently low structural damping so that the test article is representative of structures incorporating typical aerospace materials,
- and a sufficiently complex geometry so that the test article undergoes full 3-D kinematic and coupled flexible motion further stressing state-of-the-art suspension systems.

In order to develop the appropriately refined CST tools, representative test objectives with appropriate disturbances and performance metrics must be used.[7] The tests that will be carried out as part of MACE include pointing and tracking of single and multiple payloads. For each experiment run, performance will be measured in the presence of random broadband disturbances, which originate on the structural bus, and narrowband disturbances due to the planar and non-planar slewing of a second payload.

The performance metrics of all the closed-loop tests will be derived from inertial angular rate data obtained from bi-axis gyroscope packages mounted on the payloads. Specifically, the performance metrics for the various tests are stability (i.e., RMS 2-axis angular position about pointing line of sight or tracking reference profile), jitter (i.e., RMS 2-axis angular rate about pointing line of sight or tracking reference profile), slew response time (i.e., time required to complete maneuver) and percent degradation of stability and jitter from single payload performance (i.e., quantification of multiple interacting control performance).

Different types of controllers, both linear and nonlinear, will be implemented on the MACE test article depending on the performance objective and payload amplitude. Three families of controllers will be used during the on-orbit test. One family will be identical to those used in the ground test. This family will explicitly identify the differences in one-gravity and zero-gravity performance. The second family will be those which analytically corrected beforehand for the absence of suspension and gravity effects. This family will explicitly verify the ability to model the known differences between ground and flight and identify the importance of unexpected perturbations. The third family will be based upon on-orbit identification of the test article. Between these three families, the objectives of MACE will be met.

Validation of the Analytical Framework

Given a test article which captures the essential physical characteristics of the generic class of multibody platforms, a test program which validates the analytical CST tools must be formulated. Such a program must incorporate both ground-based and zero-gravity testing.

Based upon SERC's previous experience in laboratory active structural control experiments, it was concluded that a challenging yet realistic goal for MACE would be to attempt to improve closed-loop pointing/tracking performance by 40 dB over its open-loop value (Fig. 2). Independent of the absolute level of performance, this level of performance improvement will demonstrate the effectiveness of the controlled structures technology.
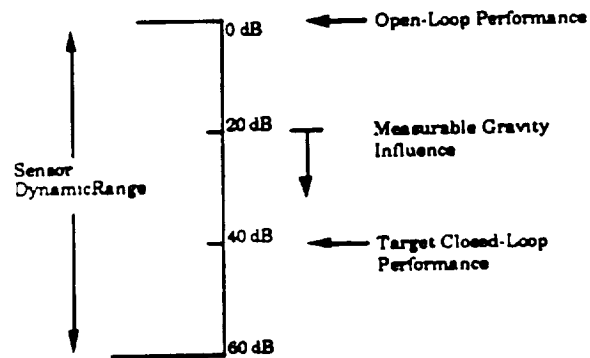

Figure 2   MACE Test Article Requirement

Both the ground testing and on-orbit testing will begin by measuring the open-loop performance. Then the authority of the controller will be increased, and closed-loop performance in the presence of scaled disturbances will be measured. By comparing closed-loop performance as a function of control authority between ground and on-orbit testing, regular (and if they exist, singular) perturbations in the dynamics which occur as a result of the change from one to zero gravity will be identified. To extract maximum benefit from the on-orbit data, it is desirable for these perturbations to begin to manifest themselves at the level of control authority which achieves half of the performance in the 1-g environment (i.e., at 20 dB). In this way, there is a series of tests (i.e., 0 to 20 dB) where ground and orbital results should be similar, and a series of tests (i.e., 20 to 40 dB) where significant deviation might be expected.

Singular perturbations could cause significant deviations throughout the 0 to 40 dB range.

This experimental approach is formulated to study the levels of control authority where the gravity perturbations become important (*i.e.*, the *transition regime*). Testing only at levels below this *transition regime* does not justify an on-orbit experiment. Testing only at levels above this *transition regime* may not yield meaningful data. Valuable information can only be uncovered by testing at levels which span the *transition regime* because these tests gradually reveal the fundamental ways in which the pertinent gravity dependent phenomena perturb the control problem.

Thus the MACE test article and associated tests are representative of an important class of future NASA, ESA, and NASDA missions, and they are designed to exhibit gravity dependent characteristics which become important to closed-loop performance as control authority is increased. By its design, the program exhibits mission applicability, technical relevancy and a fundamental exploitation of the environment unique to the STS system.

POINTING ON A FLEXIBLE STRUCTURAL BUS

A preliminary analysis of the linear pointing problem is presented to illustrate the research approach. In this section, performance degradation due to unmodelled flexibility will be investigated. There are two fundamental questions that need to be answered for the problem of pointing while mounted on a flexible structural bus. They are:

1) *How does unmodelled flexibility degrade payload pointing performance?* and

2) *How are controllers designed and implemented on a modelled flexible bus?*

The first identifies the problem and the second identifies the solution. The actual control analysis tasks that will be used as this research progresses are:

Task 1. Design a controller assuming the structural bus is rigid.

Task 2. Evaluate the performance of this controller on an evaluation model which incorporates flexibility in the structural bus.

Task 3. Use a flexible model to design the active controller using existing pointing and tracking hardware.

Task 4. Allow the flexible model controller to use additional sensors which measure flexible motion of the bus.

Task 5. Allow the flexible model controller to also use actuators to control this flexible motion.

The first two tasks address the first question. The control algorithm derived using the rigid design model in task 1 will be applied, in task 2, to a flexible evaluation model using two different sensor configurations referred to as *localized* and *centralized*, which are depicted in Fig. 3.

In the localized configuration, the inertial attitude of the payload is measured directly by an inertial platform (IP). In the centralized configuration, the inertial attitude

of the payload is inferred from the inertial attitude of the structural bus at the IP and a measure of the relative angle at the gimbal. Now, flexibility lies between the payload and the inertial measurement. If the structural bus were rigid the performance using the centralized and localized configurations would be equivalent. In the centralized configuration, however, flexibility in the structural bus can introduce an additional angle between the IP and the end of the structural bus where the gimbal is located. Left unmeasured, this flexibility induced angle can degrade pointing performance.
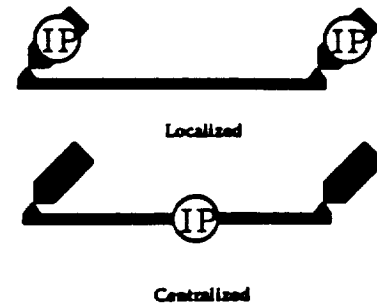

Centralized

Figure 3   Localized and centralized configurations for impinging design model control laws on the flexible evaluation model

In this paper, only typical section analyses[8] will be dealt with to investigate the manner in which structural bus flexibility degrades payload pointing performance (tasks 1 and 2). The typical section models employ lumped masses and inertias to capture the fundamental physics embedded in the linear pointing problem. Ultimately, these various control design and analysis tasks will be performed on models of increasing complexity.

There are two basic classes of rigid payloads: center of gravity (CG) mounted payloads and non-CG mounted payloads. As will be shown, CG mounted payloads exhibit certain desirable characteristics which make their control significantly easier.

The simplest model which captures the fundamentals of CG mounted payload pointing is the two inertia model shown in Fig. 4. The inertia J_1 represents a structural bus on which an attitude control torque τ_1 is applied. The inertia J_2 represents the pointed payload with the torque τ representing the gimbal torque between the payload and the structural bus. The two angle coordinates θ_1 and θ_2 are the inertial rotations of the structural bus and payload, respectively. This model is used as the rigid control design model.

In the Linear Quadratic Regulator (LQR) formulation the inertial angle of the payload can be penalized to improve payload pointing stability as

$$J = \tfrac{1}{2}\int_0^\infty \left(x^T Q x + u^T R u\right)dt \tag{1}$$

$$x = \begin{Bmatrix} \theta_1 \\ \theta_2 \\ \dot\theta_1 \\ \dot\theta_2 \end{Bmatrix},\ Q = \begin{bmatrix} 0 & 0 & 0 & 0 \\ 0 & v & 0 & 0 \\ 0 & 0 & 0 & 0 \\ 0 & 0 & 0 & 0 \end{bmatrix},\ u = \begin{Bmatrix} \tau_1 \\ \tau \end{Bmatrix} \text{ and } R = \begin{bmatrix} \alpha & 0 \\ 0 & \beta \end{bmatrix} \tag{2}$$

where J is the cost, x is the state vector, Q is the state penalty matrix, u is the control input vector, and R is the

control effort penalty matrix. The feedback solution to the steady-state Riccati equation gives

$$\left\{\begin{matrix} \tau_1 \\ \tau \end{matrix}\right\} = -\left[\begin{matrix} 0 & 0 & 0 & 0 \\ 0 & \sqrt{\frac{v}{\beta}} & 0 & \sqrt{2J_2}\sqrt[4]{\frac{v}{\beta}} \end{matrix}\right]\left\{\begin{matrix} \theta_1 \\ \theta_2 \\ \dot{\theta}_1 \\ \dot{\theta}_2 \end{matrix}\right\} = -Gx$$
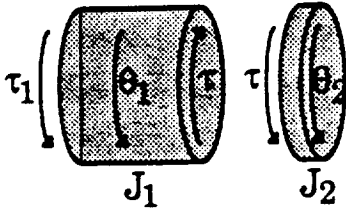
(3)

Figure 4   Rigid design model for CG mounted payload.

Notice that this control only feeds the inertial payload angle and angular rate to the gimbal torque. No attitude control or measurement of the structural bus attitude are required. The control stiffens and damps the payload motion with respect to a particular orientation in inertial space by using the structural bus as a reaction inertia. The closed-loop eigenvalues are

$$s = 0, 0, \frac{1}{\sqrt{2J_2}}\sqrt[4]{\frac{v}{\beta}}(-1\pm i)$$

(4)

As might be expected, the pointing mode is in a Butterworth pattern with damping equal to 70.71% of critical.

The closed-loop variance of the payload inertial angle about its nominal line-of-sight can be calculated assuming a steady-state additive white noise disturbance. This disturbance is assumed to be present either at the attitude control location or at the payload gimbal. Other work has looked at stability bounds associated with unmodelled flexibility.[9]

The variance is found by solving the closed-loop Lyapunov equation relating the driving noise covariance matrix V to the state covariance matrix X.

$$XA_{cl}^T + A_{cl}X = -V$$

(5)

where A_{cl} is the closed-loop state dynamics matrix of the plant. The variance of the payload inertial angle is

$$\frac{\Phi_{\tau_g \tau_g}}{2\sqrt{2J_2}\left(\frac{v}{\beta}\right)^{3/4}}$$

(6)

Notice that the variance is only a function of the additive gimbal torque noise ($\Phi_{\tau_g \tau_g}$). If there is no gimbal torque noise, the variance is zero. The attitude control noise does not disturb the payload because the motion of the payload is decoupled from the motion of the structural bus. The cost is proportional to the gimbal torque noise and decreases with increasing payload inertia and increasing control authority (v/β).

Having derived the controller using the design model, it is now possible to investigate how unmodelled flexibility degrades the pointing performance by impinging the control law (Eq. 3) upon a flexible evaluation model (Fig 5).
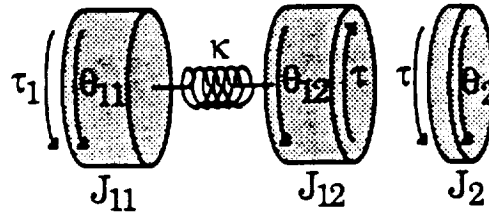

Figure 5   Flexible evaluation model for CG mounted payload

Assuming that θ_2 can be measured directly (the localized configuration), the closed-loop eigenvalues are given by

$$s = 0, 0, \frac{1}{\sqrt{2J_2}}\sqrt[4]{\frac{v}{\beta}}(-1\pm i), \pm i\sqrt{\frac{J_{11}+J_{12}}{J_{11}J_{12}}\kappa}$$

(7)

Notice that the rigid body mode is unaffected since the attitude control torque is not used. The poles associated with the pointing mode are equivalent to the poles for the system without flexibility (Eq. 4). The remaining poles are identical to the flexible mode poles of the open-loop system.

Control spillover exists because the gimbal torque disturbs the structure. However, there is no observation spillover because there is no measurement of any motion associated with the mismodelled structure. The measurement of the payload inertial motion is reconstructed exactly and therefore eliminates spillover. The closed-loop variance of the payload angle is identical to that in Eq. 6. Therefore, flexibility does not degrade the pointing performance when local inertial measurements are fed back to a CG mounted payload.

In the centralized configuration, the inertial angle of the payload equals the inertial angle of J_{12} (θ_{12}) plus the gimbal angle (θ_G). However, the inertial angle of the structural bus is assumed to be measured at the attitude control location on J_{11}. Therefore, the flexibility induced rotation $\theta_{12} \cdot \theta_{11}$ is not measured.

The closed-loop variance of the payload's inertial angle is shown in Fig. 6a (for gimbal noise) and Fig. 6b (for attitude control noise). The horizontal axis represents the ratio v/β as the cost of the control (β) is decreased. The solid line in Fig. 6a is the variance, from Eq. 6, for the rigid design model subject to gimbal noise. The dashed line represents the variance associated with the flexible evaluation model. Notice that feedback from inertial measurements at the attitude control location to the gimbal, across the flexibility, couples the flexible motion to the payload angle causing performance degradation which increases with increasing control authority (v/β).

In the case of attitude control noise (Fig. 6b), only the variance associated with the evaluation model is shown because the variance associated with the rigid design model (Eq. 6) is zero. This variance is now nonzero because the centralized configuration fails to account for the flexibility induced angle between the inertial platform and the location where the gimbal is attached
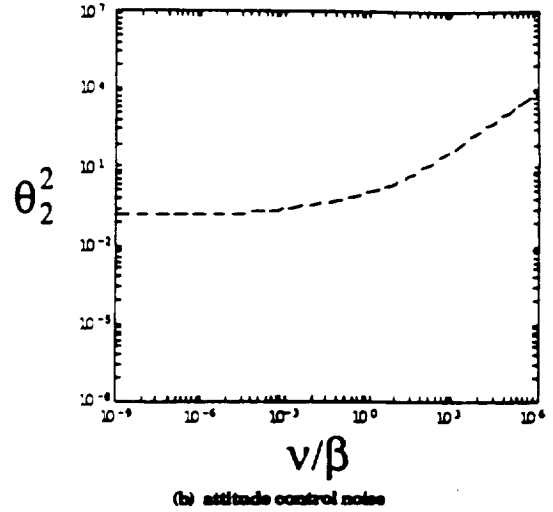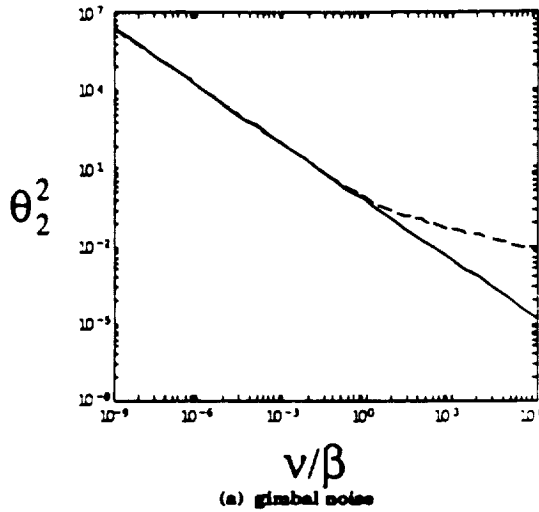
(a) gimbal noise   **(b) attitude control noise**

Figure 6 Variance of CG mounted payload under white noise applied at the gimbal and attitude control location for centralized configuration. The values of $J_1=1$, $J_2=0.5$ and $\nu=1$ were used.

$(\theta_{11}-\theta_{12})$. This flexibility-induced angle corrupts the estimate of the payload inertial angle. Since the payload attempts to track this estimate, this error causes a degradation in pointing performance.

Multibody platforms can also have non-CG mounted payloads attached to the structural bus. The non-CG mount couples rotation (θ_1) of the structural bus with rotation θ_2 of the payload. The rigid control design model is shown in Fig. 7.
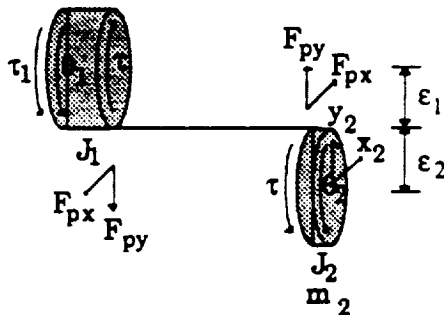
Figure 7 Rigid design model for non-CG mounted payload

Penalizing the inertial angle of the payload gives the feedback as

$$\left\{\begin{matrix} \tau_1 \\ \tau \end{matrix}\right\} = -\begin{bmatrix} 0 & \frac{1}{\alpha}b_{32}\sqrt{\frac{\nu}{\mu}} & 0 & b_{32}\sqrt{\frac{2}{\mu}}\sqrt[4]{\frac{\nu}{\mu}} \\ 0 & \frac{1}{\beta}b_{33}\sqrt{\frac{\nu}{\mu}} & 0 & \frac{1}{\beta}b_{33}\sqrt{\frac{2}{\mu}}\sqrt[4]{\frac{\nu}{\mu}} \end{bmatrix}\left\{\begin{matrix} \theta_1 \\ \theta_2 \\ \dot{\theta}_1 \\ \dot{\theta}_2 \end{matrix}\right\} = -Gx \tag{8}$$

where

$$\mu = \frac{1}{\alpha}b_{32}^2 + \frac{1}{\beta}b_{33}^2 \tag{9}$$

$$b_{32} = -\frac{m_1 m_2 \varepsilon_1 \varepsilon_2}{den}$$

$$b_{22} = \frac{(m_1+m_2)J_1 + m_1 m_2 (\varepsilon_1+\varepsilon_2)}{den} \tag{10}$$

$$den = (m_1+m_2)J_1 J_2 + (J_1\varepsilon_2^2 + J_2\varepsilon_1^2)m_1 m_2 \tag{11}$$

Notice that while both the attitude control and gimbal actuators are used, only the inertial states of the payload are measured. The closed-loop poles are given by

$$s = 0, \; 0, \; \frac{1}{\sqrt{2}}\sqrt[4]{\nu\mu}(-1\pm i) \tag{12}$$

Again, the Butterworth pattern exists. The control now requires feedback to the structural bus' attitude control torque since angular motion of the structural bus and payload are coupled in open-loop.

This control can be impinged upon a flexible evaluation model such as the one shown in Fig. 8.
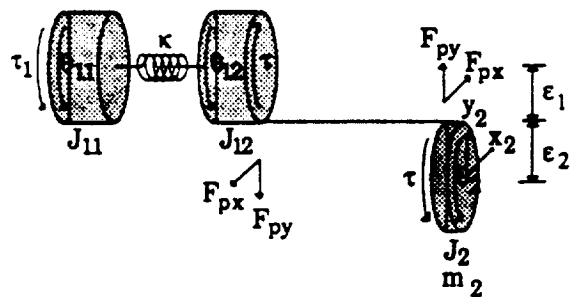

Figure 8 Flexible evaluation model for non-CG mounted payload.

Flexible motion of the structural bus, caused by gimbal and attitude control torque noise, perturbs the angle of the payload. This results in both control and observation spillover.

Impinging the feedback in Eq. 8 on the evaluation model in Fig. 8, using the localized configuration, gives the results shown in Figs. 9a and 9b. The overlaid solid and dashed lines in Fig. 9a show that the level to which gimbal noise disturbs the payload angle barely changes

between the design and evaluation models. The solid curve in Fig. 9b shows the variance of the payload angle associated with the design model (Fig. 7) in the presence of attitude control torque noise. Notice that since structural bus rotation couples with payload rotation, attitude control noise now disturbs the payload in the design model. The dashed line in Fig. 9b shows the variance associated with the evaluation model. Excitation of the flexible motion couples with payload rotation to cause performance degradation, even though a localized configuration is used. The evaluation model is more susceptible to performance degradation as a function of control authority when the noise is introduced at the attitude control location than when it is introduced at the gimbal. This is because the unmodelled flexibility lies between the disturbance and the payload thereby frequency shaping the disturbance on the payload in the former case, while the disturbance is impinged directly upon the payload in the latter.

Figures 9c and 9d show the variance caused by the two different noise sources for the non-CG mounted systems when a centralized configuration is used. In both figures, the solid curves represent the variance associated with the design model. The dashed curves are the variances of the evaluation model. Notice in Fig. 9c

that the variance associated with gimbal noise deviates from that for the design model at high levels of control authority. This was not the case for the localized configuration (Fig. 9a). For the case of attitude control noise (Fig. 9d), deviation again occurs between the variance of the design and evaluation models. Note, however, that for either noise source the variance eventually increases with increasing control authority and that the level of control authority which minimizes the variance depends on which noise source exists.

The above analysis has served to illustrate the degradation in performance that can occur when controllers designed using rigid models are applied to flexible spacecraft. The open-loop coupling of the unmodelled flexibility to the payload angle makes the non-CG systems more susceptible to performance degradation than the CG system. Centralized configurations exhibit more deviation from the expected rigid body performance than localized configurations because the feedback paths are closed across the flexibility thereby coupling the unmodelled flexibility to payload motion. However, centralized configurations are programmatically advantageous because the various payloads share an expensive common resource, the IP.
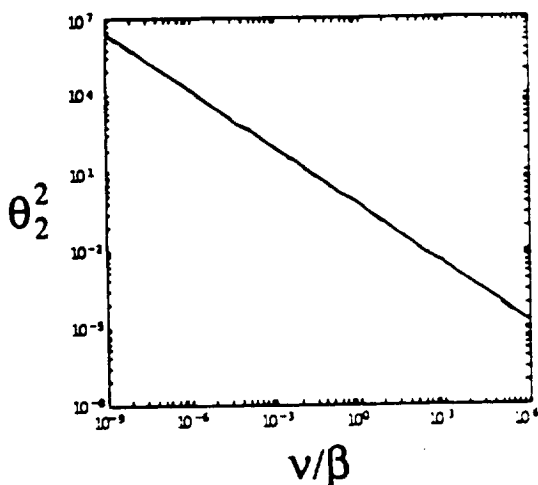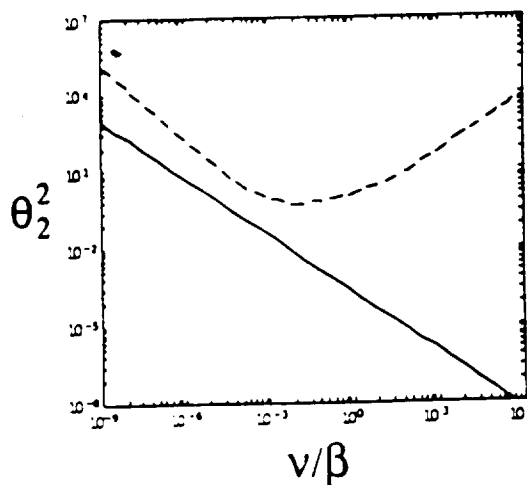

(a) localized config, gimbal noise
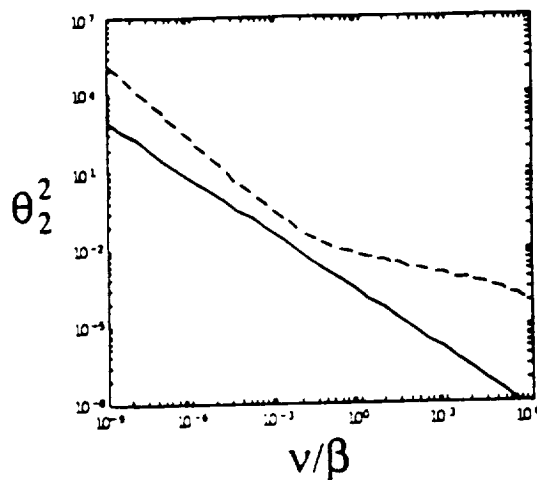
(b) localized config, attitude control noise
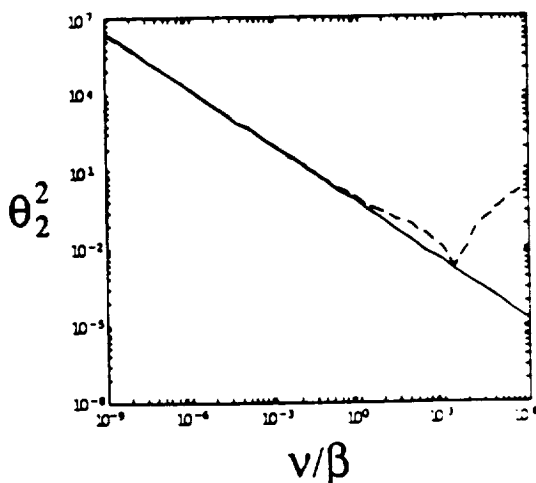
(c) centralized config, gimbal noise

(d) centralized config, attitude control noise

Figure 9 Variance of non-CG mounted payload under white noise applied at the gimbal and attitude control location for localized and centralized configurations. $J_1=1$, $J_2=5$, $\alpha=1$, $\epsilon_1=.2$, $\epsilon_2=1$, $\omega_2=1$

C-2

EFFECT OF GRAVITY ON THE POINTING AND TRACKING PROBLEMS

Multibody platforms were chosen as the reference mission configuration not only because they characterize many proposed missions but also because they are arguably the most susceptible to gravity influences. The essence of the on-orbit phase of the MACE program is to identify and characterize these influences. To this end, a set of sample problems was selected each of which captures a different type of gravity perturbation. The objective of this line of research is to analytically predict the manner and degree to which these influences perturb the closed-loop control problem.

Gravity will cause changes between dynamics measured on the ground and on-orbit. These perturbations can be grouped in two broad categories: those resulting directly from the presence of the gravity field, and those which are a result of the mechanical suspension system required for 1-g tests. These are illustrated in Fig. 10. The first category includes: modal coupling which occurs due to the static sag of a structural member, gravity stiffening (in tension) or destiffening (in compression) of structures along the gravity vector, and dynamic buckling which occurs when the structural members deform transversely to the gravity vector. The second category of problems includes: added stiffness and mass of the suspension system, added damping of the suspension system, and modal coupling of the suspension dynamics with the test article. All of these influences result in perturbations of the system frequencies, damping and mode shapes which can fundamentally alter the stability and performance of a controller, and must be taken into account in design.

GROUND-BASED ENGINEERING MODEL TESTBED

The initial configuration of the MACE test article is shown in Fig. 11. It consists of a segmented straight tubular bus with a two axis pointing/tracking payload at each end. An active, strain-inducing segment is located along the bus. The MACE test article will have a closely coupled set of flexible modes with a fundamental bending frequency below 2 Hz. This is done through the choice of material (Lexan) and geometry of the bus.

A segmented design of tubular members connected by universal joints was chosen as the bus structure for a number of reasons. First, it provides an evolutionary test article since it is straightforward to modify its geometry to represent more complex structures. It is also possible to add and change the locations of passive and active members. These include piezoelectric members and members with a high level of passive damping. Discrete devices such as torque wheels, accelerometers and proof mass actuators can be attached at the joints.

The overall length of the test article is approximately 1.5 m. The MACE engineering model (EM) node provides for attachment of the members through the MACE joint and provides a standard hole pattern for attachment of the payloads, inertial platforms and other instrumentation. Each member is .4 m in length and 25.4 mm in diameter. Four members are used in the MACE initial configuration.

Two types of payloads are currently envisioned:

- *Pointing/tracking.* These payloads are mounted to the bus through a two axis motorized gimbal mount. The payloads are rigid, and capable of 120° motion in two axes.

- *Flexible appendage.* This payload consists of a flexible, instrumented boom mounted on a two axis motorized gimbal. The gimbal is capable of 120° motion in two axes, and the fundamental frequency of the flexible boom is less than the fundamental frequency of the bus structure (<2 Hz).

The DC torque actuators in the gimbals will be used to align the payloads or to sweep them through a predetermined tracking profile. Rate gyroscopes located on the rigid pointing/tracking payloads and the flexible appendage will provide a measure of the inertial angular rate of the payloads for feedback and performance measure. The gimbal motors will have integrated encoders.

In addition to the sensors and actuators located on the payloads, the following sensors and actuators will also be used:

- *Torque Wheels.* A set of three torque wheels is situated at the center node of the structural bus. The purpose of these torque wheels is to provide both three axis attitude control and structural control.
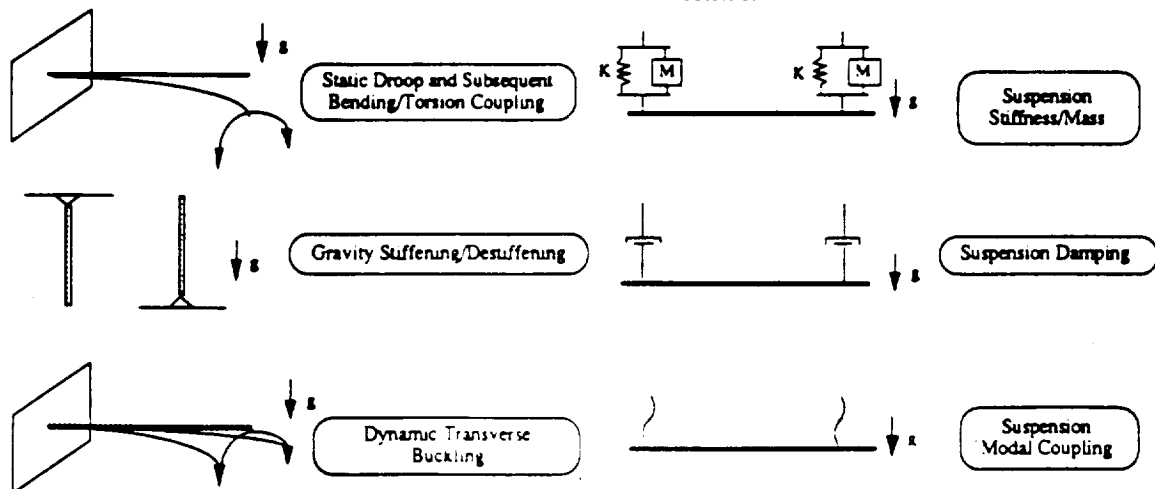

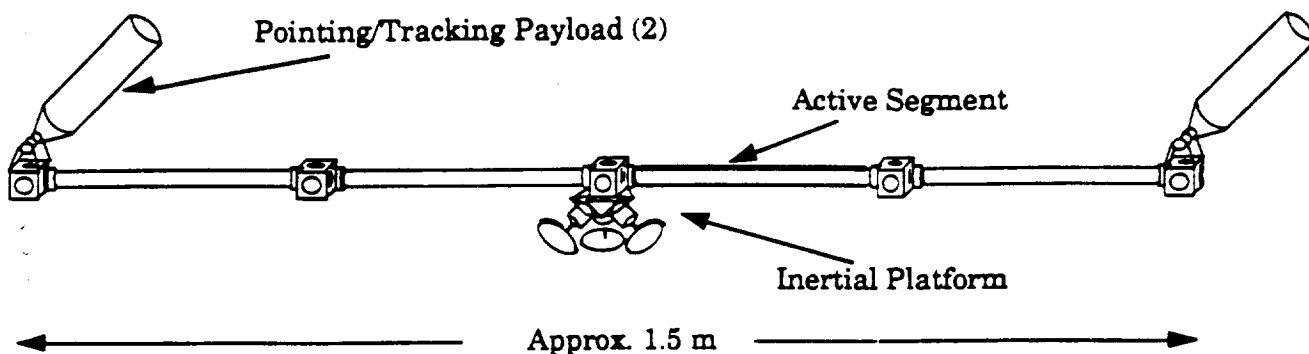Figure 10 Sample problems illustrating the effect of gravity on structures

Pointing/Tracking Payload (2)

Active Segment

Inertial Platform

Approx. 1.5 m

Figure 11 Initial configuration for multibody platform test article

- *Active Member.* The MACE active member consists of a square Lexan rod with piezoelectric ceramics mounted on the sides. It will be capable of bending about two axes. The member will be instrumented with surface bonded strain gauges.
- *Rate Gyroscopes.* A set of three rate gyroscopes will be collocated with the torque wheels forming an inertial attitude control platform.

Additional sensors such as strain gauges, accelerometers, *etc.* can be placed along the test article as required by the various control algorithms.

Given the recognized need to perform closed-loop ground-based tests, the question arises as to how does one best approximate the boundary conditions of space. Required is a system which will support the payload weight while having a minimal impact on the test article dynamics. A zero spring rate pneumatic/electric suspension device from CSA Engineering Inc. of Palo Alto, California will be used to support the test article in 1-g. The suspension system will have a 63.5 mm maximum vertical stroke, a maximum payload of 17.4 kg, and will use displacement and acceleration feedback.

FLIGHT TESTBED

The MACE flight testbed consists of (1) the Experiment Support Module (ESM), which contains all experiment electronics in one standard middeck locker, and (2) the MACE test article which is stowed in a second middeck locker (Fig. 12).[10] The primary difference between the ground-based EM and the flight testbed will be the manner in which the various active components of the test article will be connected to each other and to the ESM. Electrical connections along the bus will be accomplished by modifying the EM joint to provide simultaneous electrical and mechanical connections. This will be accomplished by inserting a multipin electrical connector inside the joint. Wiring will run inside the hollow Lexan members. Finally, the test article will be connected to the ESM through a single umbilical which will also attach to a test article node. This greatly simplifies on-orbit assembly time thereby maximizing testing time.

Experiment Support Module (ESM)

Much of the MODE 2 ESM will be identical to the MODE 1 ESM, utilizing many similar or identical components. These will include the ESM support frame, data storage device, analog circuit card cage, and the majority of the computer system. Modifications will include the addition of a real time high speed control computer, and downlink/uplink capability. All MACE data acquisition, storage, signal processing and signal generation will be performed by Payload Systems SensorNet Experiment Computer.

The purpose of the downlink/uplink is to allow on-orbit identification, downlink of identified parameters and uplink of new control algorithms in the event that unexpected behavior occurs. Downlink will be accomplished through data interleaving on the STS video channel. Uplink will be accomplished through the STS Text and Graphics System (TAGS).

Required Resources

MACE resource requirements are summarized in Table 2 below.

Table 2 MACE Resource Requirements Summary Table

ESM		
	Weight	54 lbs.
	Volume, operational	1 Middeck Locker
	Volume, stowed	1 Middeck Locker
	Power requirement	113 Watts @ +28 VDC
	Telemetry	Downlink/uplink
	Crew activities	Set-up, operations
	Data processing	Performed by ESM
MACE Test Article		
	Weight	54 lbs.
	Volume, operational	30" x 8" x 60"
	Volume, stowed	1 Middeck Locker
	Power requirement	15 Watts
	Crew activities	Set-up, operations

Flight Operations

MODE-2 calls for operation by the crew on two separate days. Procedures require configuration, activation and operation of MODE-2 by one crew member during a normal eight hour work period. If the test sequence proceeds flawlessly, the crew task for all the MACE tests will involve assembling the test article in a predetermined configuration, running open-loop identification tests over a specified frequency range, and beginning closed-loop operations. The probable testing scenario would be to excite the structure using a predetermined excitation profile with one of the on-board actuators, then, after steady-state has been achieved, to
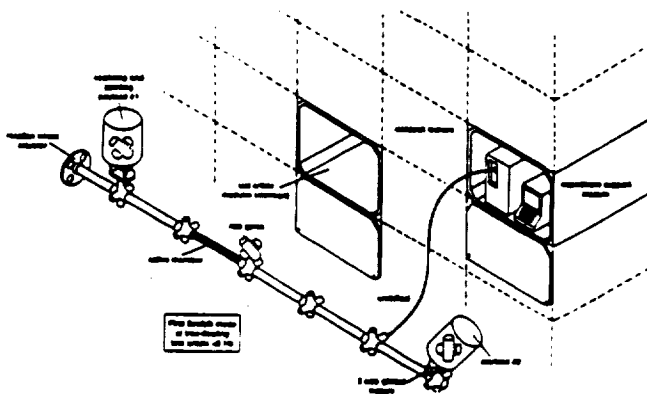
Figure 12. The MACE test article deployed on the STS Middeck

initiate the active control using low gain values. Assuming no instabilities are found, the performance metric and sensor outputs will be recorded and the experiment can be repeated with higher gain values, until all the predetermined gains have been implemented or an instability is reached. Testing would proceed to additional configurations or control algorithms as time permits. This procedure is illustrated in Fig. 13.
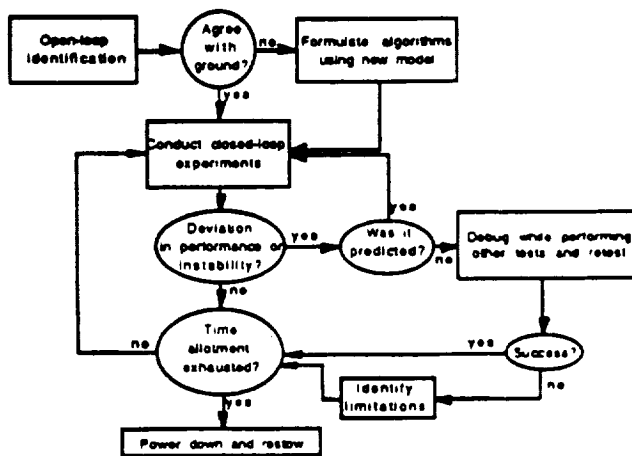

Figure 13 Testing procedure decision flowchart

After the first day, video and video encoded data will be transmitted to the ground to be analyzed by the PI team and new control algorithms, if necessary, will be uplinked to the crew prior to the second day's operation. While no real time communications, audio or video, are required, this infrequent access to the STS video and TAGS system will be necessary for up/down link activities.

CONCLUSIONS

There is a clear need to develop an effective and efficient analytical and test procedure for qualifying CST spacecraft. The goal is to determine the degree to which gravity perturbs the closed-loop performance of Large Space Structures which cannot be fully or accurately tested on the ground.

The MODE-2 program, using the MACE test article, is designed to develop this qualification procedure by formulating a set of CST design and qualification tools and validating these tools through extensive ground and on-orbit testing. By conducting these open and closed-loop tests using a relatively inexpensive test article, a cost effective preliminary search can be performed to identify the presence of gravitational perturbations to the control problem. The specific criteria which will determine experiment success are the identification of the regular (and, if they exist, singular) perturbations in the dynamics which occur as a result of the change from one to zero gravity, and the development of validated analytical and experimental CST tools needed to insure the operational success of a CST spacecraft.

REFERENCES

1   Crawley, E.F., Miller, D.W., van Schoor, M., de Luis, J., "Middeck 0-Gravity Dynamics Experiment (MODE): Project Plan," Massachusetts Institute of Technology Space Systems Laboratory Report # SSL 9-89, 1989.

2   Crawley, E.F., de Luis, J., Miller, D.W., "Middeck Active Control Experiment (MACE): Phase A Final Report," Massachusetts Institute of Technology Space Systems Laboratory Report # SSL 7-89, 1989.

3   Skelton, R.E., "A Tutorial on Model Error Concepts in Control Design, " to appear in *International Journal of Control.*

4   NASA Space Systems Technology Model, NASA TM 88176, Prepared for the Office of Aeronautics and Space Technology, June 1985

5   Space Station Engineering Design Issues: Report of a Workshop, Irvine, CA Nov. 1988, National Academy Press, Washington, DC, 1989

6   Proceedings of the Workshop on Multibody Simulation, JPL D-5190, Jet Propulsion Laboratory, April 1988.

7   Laskin, R.A., Sirlin, S.W., "Future Payload Isolation and Pointing System Technology," *Journal of Guidance, Control and Dynamics,* Vol. 9, No. 4, pp 469-477.

8   Miller, D.W., Jacques, R.N., de Luis, J., "Typical Section Problems for Structural Control Applications," Paper # AIAA-90-1225, presented at the Dynamics Specialist Conference, Long Beach, CA, April 1990.

9   Spanos, J.T., "Control-Structure Interaction in Precision Pointing Servo Loops," J. of Guidance, Control, and Dynamics, Vol. 12, No. 2, pp. 256-265, March-April 1989.

10 MACE Hardware Design Document, MACE-1-900, MIT Space Engineering Research Center, May, 1990.